

Precipitate development in steel

An in-depth study on formation and growth of a second solid phase

Slooter, R.J.

DOI

[10.4233/uuid:f51bfa1d-aca5-46d1-80a4-00a45f55fa3b](https://doi.org/10.4233/uuid:f51bfa1d-aca5-46d1-80a4-00a45f55fa3b)

Publication date

2025

Document Version

Final published version

Citation (APA)

Slooter, R. J. (2025). *Precipitate development in steel: An in-depth study on formation and growth of a second solid phase*. [Dissertation (TU Delft), Delft University of Technology].
<https://doi.org/10.4233/uuid:f51bfa1d-aca5-46d1-80a4-00a45f55fa3b>

Important note

To cite this publication, please use the final published version (if applicable).
Please check the document version above.

Copyright

Other than for strictly personal use, it is not permitted to download, forward or distribute the text or part of it, without the consent of the author(s) and/or copyright holder(s), unless the work is under an open content license such as Creative Commons.

Takedown policy

Please contact us and provide details if you believe this document breaches copyrights.
We will remove access to the work immediately and investigate your claim.

PRECIPITATE DEVELOPMENT IN STEEL

AN IN-DEPTH STUDY ON FORMATION AND GROWTH OF A
SECOND SOLID PHASE

PRECIPITATE DEVELOPMENT IN STEEL

AN IN-DEPTH STUDY ON FORMATION AND GROWTH OF A
SECOND SOLID PHASE

Proefschrift

ter verkrijging van de graad van doctor
aan de Technische Universiteit Delft,
op gezag van de Rector Magnificus prof. dr. ir. T.H.J.J. van der Hagen,
voorzitter van het College voor Promoties,
in het openbaar te verdedigen op dinsdag 22 april 2025 om 12:30 uur

door

Rutger Jarrick SLOOTER

Natuur- en wiskundig ingenieur,
Technische Universiteit Delft, Delft, Nederland,
geboren te Korendijk, Nederland.

Dit proefschrift is goedgekeurd door de

promotor: Dr. ir. M.H.F. Sluiter

copromotor: Dr. ir. C. Bos

Samenstelling promotiecommissie:

Rector Magnificus,	voorzitter
Dr. ir. M.H.F. Sluiter,	Technische Universiteit Delft
Dr. ir. C. Bos,	Technische Universiteit Delft & Tata Steel Europe, IJmuiden

Onafhankelijke leden:

Dr. F. Maresca,	Rijksuniversiteit Groningen
Prof. dr. ir. J. Sietsma,	Technische Universiteit Delft
Prof. dr. M. Dijkstra,	Universiteit Utrecht
Prof. dr. ir. B.J. Kooi,	Rijksuniversiteit Groningen

Reserve lid:

Prof. dr. ir. J.M.C. Mol,	Technische Universiteit Delft
---------------------------	-------------------------------

Overige leden:

† Dr. W.G.T. Kranendonk, Tata Steel Europe, IJmuiden

† Dr. W.G.T. Kranendonk heeft in belangrijke mate aan de totstandkoming van het proefschrift bijgedragen.



Keywords: Classical Nucleation and Growth, (Reference-Free) (Modified) Embedded Atom Method, Atomistic Simulation, Precipitation, Steel, Carbide.

Printed by: Gildeprint

Front & Back: Wallpaper-style artistic impression of ferritic steel embedded with metal-carbide platelets.

Style: TU Delft house style, with minor adaptations made by the author.

Copyright © 2025 by R.J. Slooter

ISBN 978-94-6496-356-4

An electronic version of this dissertation is available at

<http://repository.tudelft.nl/>.

*Ijzer scherpt men met ijzer;
alzo scherpt een man het aangezicht zijns naasten.*

Spreuken 27:17

CONTENTS

Summary	xi
Samenvatting	xiii
Preface	xv
1 Introduction	1
1.1 Introduction	2
1.2 KWN model and Classical Nucleation and Growth	2
1.2.1 Nucleation	2
1.2.2 Growth	6
1.2.3 Coarsening	6
1.3 Interatomic potentials for molecular dynamics	11
1.3.1 Early potentials	11
1.3.2 Embedded Atom Method, Finnis-Sinclair, and glue potentials	14
1.3.3 Modification and improvement	16
1.3.4 Reference-free MEAM	18
1.3.5 Machine learning or AI potentials	18
1.4 Nucleation of precipitates	20
1.4.1 Guinier-Preston zone	20
1.4.2 Spinodal decomposition	23
1.4.3 Nucleation of carbides	23
1.5 Summary	24
References	25
2 Approximation and characteristic times in precipitation modelling	33
2.1 Introduction	35
2.2 Derivation for isothermal precipitation	35
2.2.1 Evolution equations	35
2.2.2 Reference model	39
2.2.3 First approximation	40
2.2.4 Bootstrapping and approximating matrix concentration	42
2.2.5 Incubation time	46
2.2.6 Coarsening	46
2.2.7 Competition between nucleation and growth	48
2.3 Derivation for quasi-isothermal precipitation	49
2.4 Discussion on validity and limitations	50
2.5 Conclusions	52
References	52

3	A Reference-Free MEAM Potential for α-Fe and γ-Fe	57
3.1	Introduction	58
3.2	Fitting procedure	59
3.2.1	RF-MEAM formalism	59
3.2.2	Methodology.	60
3.2.3	Elastic constants for γ -Fe	61
3.2.4	Crystal structure and elastic constants	63
3.2.5	Point defects	64
3.2.6	Stacking faults and free surfaces	65
3.3	Validation of the potential and discussion	65
3.3.1	Structural properties	65
3.3.2	Point defects	66
3.3.3	Surfaces and stacking faults	66
3.3.4	Thermal expansion	69
3.3.5	Discussion	71
3.4	The potential	72
3.5	Conclusions.	74
	References	74
4	Atomistic simulation of carbide formation in ferrite	81
4.1	Introduction	82
4.2	Methodology	82
4.2.1	Static relaxations in Fe-M-C	82
4.2.2	DFT calculations.	84
4.2.3	Molecular dynamics for Fe-Nb-C	84
4.3	Results	85
4.3.1	Static relaxation	85
4.3.2	Molecular dynamics	91
4.3.3	Stability of clusters at finite temperatures	93
4.4	Formation mechanism	96
4.5	Conclusion	98
	References	98
5	Formation and growth of transition metal carbides in ferrite	103
5.1	Introduction	104
5.2	Methodology	105
5.2.1	Introduction	105
5.2.2	DFT-calculations.	105
5.2.3	LAMMPS simulations for the transformation mechanism	106
5.3	Formation of transition metal clusters	106
5.3.1	DFT calculations for the formation of transition metal clusters in ferrite	106
5.4	Transformation mechanism.	110
5.4.1	Transformation to NaCl-structure	110
5.4.2	Matrix misfit and strain	115
5.4.3	Results from LAMMPS simulations	118

5.5	Conclusion	119
	References	120
6	Conclusions & recommendations	123
6.1	Models for precipitation	124
6.2	RF-MEAM potential.	124
6.3	Carbide formation	125
A	Sensitivity analysis of the Kampmann-Wagner Numerical model	127
A.1	Mathematical analysis	128
A.1.1	Diffusion coefficient	129
A.1.2	Interface energy	129
A.1.3	Solubility product	129
A.2	Worked example: Niobium carbide	130
	References	130
	Acknowledgements	135
	Curriculum Vitae	137
	List of Publications	139

SUMMARY

MANY modern advanced steel grades make use of alloying elements which form so-called ‘nano-precipitates’. These nano-precipitates increase the strength, without affecting ductility and toughness much. The improved steels are for instance used in the automotive industry to increase car safety and decreasing weight, thus maintaining or improving fuel efficiency.

Nano-precipitates contribute to the strength by two mechanisms: directly by precipitation hardening and indirectly by pinning of grain boundaries, which keeps grain sizes small. Both mechanisms are determined by the volume fraction and the average size of the precipitates. The production of High Strength Low Alloy (HSLA) steels requires a delicate control of the heat-treatment to optimize the precipitate properties. The goal is to reach the optimal size and number density of the nano-precipitates, to optimize the contribution of precipitates to the required properties of strength and ductility.

A brief introduction into the background information of the topics that were studied is provided in Chapter 1. Here the Classical Nucleation and Growth Theory (CNGT) is explored which is the most applied theory for modelling precipitate development (*i.e.* nucleation, growth, and coarsening) during heat-treatment. Secondly a background to inter-atomic potentials is provided, where we reflect on the developments leading up to the Reference-Free Modified Embedded Atom Method (RF-MEAM). And thirdly a more detailed view on the nucleation of precipitates is examined, testing one of the main assumptions in the CNGT. To this end particularly the formation of so called ‘Guinier-Preston zones’ is touched upon. Experimental work on carbide and nitride nucleation in ferrite has shown the complex nature of the initial precipitation stages which require further study by atomistic methods.

A new analytical approximation to the equations describing Classical Nucleation and Growth Theories is presented in Chapter 2. This approximation predicts the mean precipitate radius and number density development under quasi-isothermal conditions. The approximation allows the prediction of a start and end time for the nucleation stage, as well as a time at which growth occurs and when coarsening starts. These times form an outline for the numerical solution to the CNGT model, providing key insights without running a full simulation. Such insights are useful to more efficiently simulate precipitate development.

Additionally several dimensionless parameters are formulated providing an intuitive insight in the precipitation trajectory.

THEN, in Chapter 3, a Reference-Free Modified Embedded Atom Method (RF-MEAM) potential for iron is constructed. The potential is aimed at predicting both bcc and fcc (α -Fe and γ -Fe) lattice properties, with a special interest in modelling in the 800-1300 K temperature range as this is the temperature range in which transformations and key processes in steel occur.

Of practical interest is the fact that RF-MEAM potentials can be plugged directly into

common molecular dynamics simulation software, e.g., LAMMPS¹.

The new potential combines good characteristics for point defect energies with free surface and stacking fault energies. Also the Nishiyama-Wassermann and Kurdjumov-Sachs orientation relation ratios and interface energies are reproduced, allowing for simulations of α -Fe and γ -Fe interphases.

IN Chapter 4, using a MEAM potential, molecular dynamics (MD) simulations for a Fe-M-C (M = Nb, Ti) ternary system are performed, these simulations reveal that there are growth pathways for M-C clusters with a monotone decrease in Gibbs energy, which suggests that the highest energy barrier for the formation of M-C clusters in ferrite is the diffusion barrier for the atoms which make up the cluster. The clusters found for both Nb and Ti have an Fe₃MC₃ composition. Furthermore it is found that these clusters are likely stable up to common process temperatures of 1100 K.

The formation of FeMC₃ clusters as found here shows a formation mechanism for nano-precipitates of carbides in ferrite consisting of multiple steps; where first a C cluster forms, then M atoms attach to the C cluster forming an FeMC cluster, and in the final step the cluster transforms to a NaCl-structured² carbide.

IN Chapter 5 the work of Chapter 4 is deepened. Similarities found between Nb-C and Ti-C cluster formation in ferrite suggest that other group IV and V transition metals (M = Ti, Zr, Hf, V, Nb, and Ta) could follow the same formation trajectory. Density Functional Theory (DFT) is used to analyse several M-M and M-C pairs and triplets, from the studied configurations clear trends in their binding energies are found that further imply similarity in their “carbide-formation-paths”.

The clusters found in Chapter 4 are found to behave in a way which is similar to that of Guinier-Preston zones in aluminium alloys, in that they form in a single atomic layer, and are energetically preferred to the formation of the final precipitate.

And finally the transition from the FeMC₃ cluster to a NaCl-structured precipitate is examined using MD-simulations, where it is found that the matrix strain energy is the key driving force behind the transformation.

FINALLY, in Chapter 6, the applicability of the presented research is examined. Furthermore several recommendations for follow-up studies are given.

¹Large-scale Atomic/Molecular Massively Parallel Simulator

²B1-structure in *Strukturbericht* notation: Ewald, P.P. and Hermann, C. editors, *Strukturbericht 1913-1928*, (1931).

SAMENVATTING

VEEL moderne geavanceerde staal types maken gebruik van legeringselementen die zogeheten ‘nano-precipitaten’ vormen. Deze nano-precipitaten verhogen de sterkte, waarbij het effect op de vervormbaarheid en hardheid klein is. Het verbeterde staal wordt bijvoorbeeld gebruikt in de automobielenindustrie om zo veiligere voertuigen te maken zonder de massa te vergroten, zó dat de brandstofefficiëntie wordt behouden of zelfs vergroot.

Nano-precipitaten dragen bij aan de sterkte door twee mechanismen: direct door precipitatie-verharding, en indirect door het ‘vast zetten’ van korrelgrenzen, waardoor de korrels klein blijven. Beide mechanismen worden bepaald door de volume fractie en gemiddelde grootte van de precipitaten. De productie van *High Strength Low Alloy (HSLA)* staal vereist een nauwkeurige afstemming van de warmtebehandeling om de eigenschappen van de precipitaten te optimaliseren. Het doel is om een optimale grootte en dichtheid van nano-precipitaten te bereiken, om zo een optimale bijdrage van de precipitaten aan de materiaalsterkte en vormbaarheid te verkrijgen.

EEN korte introductie van de achterliggende theorie van de bestudeerde onderwerpen wordt in Hoofdstuk 1 gegeven. Hier verkennen we de Klassieke Nucleatie en Groei Theorie (CNGT) welke het meest toegepast wordt voor het modelleren van precipitaatontwikkeling, (d.w.z., nucleatie, groei, en vergroving) tijdens warmtebehandeling. Het tweede gedeelte gaat in op de achtergrond van interatoompotentialen, waar we terugblikken op de ontwikkelingen die hebben geleid tot de ‘Referentie-Vrije Gemodificeerde Ingebedde Atoom Methode’³ (RF-MEAM). En in het derde gedeelte wordt een meer gedetailleerd beeld bekeken van de nucleatie van precipitaten, waarmee een van de belangrijke aannames van CNGT wordt beproefd. Hiertoe wordt in het bijzonder de vorming van zogeheten ‘Guinier-Preston zones’ behandeld. Ook wordt hier verwezen naar experimenteel werk aangaande carbide en nitride nucleatie in ferriet.

EEN nieuwe analytische benadering van de vergelijkingen welke de Klassieke Nucleatie en Groei Theorie (CNGT) beschrijft wordt in Hoofdstuk 2 gepresenteerd. Deze benadering voorspelt de gemiddelde straal en grootte waarschijnlijkheidsverdeling en het totale aantal precipitaten onder quasi-isotherme omstandigheden.

De benadering laat toe een begin- en eindtijd voor de nucleatie stap te voorspellen, evenzo een tijd waarop groei plaatsvindt en wanneer vergroving aanvangt. Deze tijden vormen tijdslijmieten voor de numerieke oplossing van het CNGT model, daarbij voorzien ze belangrijke inzichten zonder een volledige simulatie te laten draaien. Dit soort inzichten zijn bruikbaar om efficiënter precipitatie ontwikkeling te simuleren.

Verder worden in dit hoofdstuk verschillende dimensieloze grootheden geformuleerd welke een intuïtief inzicht verschaffen in het precipitatie traject.

³Er wordt vaak jammerlijk vergeten dat de Nederlandse taal heel mooi kan zijn.

VERVOLGENS wordt, in Hoofdstuk 3, een RF-MEAM potentiaal voor ijzer geconstrueerd. Deze potentiaal heeft als doel de roostereigenschappen van zowel krg en kvg⁴ (α -Fe en γ -Fe) te voorspellen, met een bijzondere aandacht voor modelleren in het temperatuurbereik van 800-1300 K dit is het temperatuurbereik waarin transformaties en andere belangrijke processen in staal plaatsvinden.

Van praktische belang is het feit dat RF-MEAM potentialen direct in gebruikelijke *moleculaire dynamica* simulatie software kunnen worden gebruikt, bijvoorbeeld LAMMPS⁵. De nieuwe potentiaal combineert goede karakteristieken voor roosterdefecten met vrijoppervlaktenergieën en stapelfoutenergieën. Tevens worden de Nishiyama-Wassermann en Koerdjoemov-Sachs oriëntatierelatieverhoudingen en grensvlakenergieën gereproduceerd, wat simulaties van α -Fe en γ -Fe interfasen toelaat.

IN Hoofdstuk 4 worden MD⁶ simulaties met een MEAM potentiaal voor een Fe-M-C (M = Nb of Ti) ternair systeem uitgevoerd. Deze simulaties tonen aan dat er groeipaden zijn voor M-C clusters met een monotone afname in Gibbs energie. Dit suggereert dat de hoogste energie barrière voor de vorming van M-C clusters in ferriet de activeringsenergie voor diffusie is van de atomen die in de cluster zitten. De clusters voor zowel Nb als Ti hebben een FeMC₃ samenstelling. Verder is berekend dat deze clusters waarschijnlijk stabiel zijn bij normale procestemperaturen van 1100 K.

De vorming van FeMC₃ clusters zoals hier gevonden toont een vormingsmechanisme voor nano-precipitaten van carbides in ferriet bestaande uit meerdere stappen; waarbij eerst een C cluster vormt, dan worden M atomen aan de C cluster gebonden om een cluster te vormen, en in de laatste stap transformeert de FeMC cluster naar een carbide met een keukenzoutstructuur.

IN Hoofdstuk 5 wordt het werk uit Hoofdstuk 4 verdiept. De overeenkomsten tussen Nb en Ti bij de vorming van Nb-C en Ti-C clusters in ferriet suggereert dat de groep IV en V transitie metalen (M = Ti, Zr, Hf, V, Nb en Ta) mogelijk dezelfde vormingspaden volgen. Hiervoor wordt DFT⁷ gebruikt om verscheidene M-M en M-C paren en triplets in ferriet te analyseren, vanuit de bestudeerde configuraties volgen duidelijke trends in hun bindingsenergieën welke verdere overeenkomsten in hun “carbide-vormingspaden” impliceren.

De in Hoofdstuk 4 gevonden clusters gedragen zich op vergelijkbare wijze als Guinier-Preston zones in aluminium legeringen, in dat ze vormen in een enkele atomaire laag, en in dat hun vorming energetisch voordeliger is dan de vorming van uiteindelijke precipitaten.

En ten laatste wordt de transitie van de FeMC₃ cluster naar een precipitaat met een keukenzoutstructuur onderzocht door middel van MD simulaties. Er is gevonden dat de matrix deformatie-energie de drijvende kracht is achter de transformatie.

TEN slotte wordt, in Hoofdstuk 6, de toepasbaarheid van de gepresenteerde onderzoeksresultaten bekeken. Tevens worden enkele aanbevelingen voor vervolgonderzoek gedaan.

⁴ *Kubisch ruimtelijk gecentreerd en kubisch vlakgecentreerd.*

⁵ Large-scale Atomic/Molecular Massively Parallel Simulator

⁶ Molecular Dynamics

⁷ Density Functional Theory

PREFACE

Lectori Salutem,

The desire to understand the universe never loses its appeal, and in this study several probes have been made into nature to find methods to systematically describe materials. Besides the development of precipitates in steel, the atomistic nature of precipitate-steel environments has been studied. As we are of finite nature, both in knowledge and in resources we have been prompted to reduce nature to sets of parameters and mathematical equations. And however close this may bring us to reproducing nature, it is limited by human assumptions and knowledge. As we remain finite, and all creation is finite in nature, approximations may be the best we can do. However, even in a virtual nature we can still develop a much better understanding of the world we live in. I wish the reader a good read, to be entertained and to be ever learning.

Rutger Jarrick Slooter
Delft, May 2024

1

INTRODUCTION

It takes considerable knowledge just to realize the extent of your own ignorance.

Thomas Sowell

Einer neuen Wahrheit ist nichts schädlicher als ein alter Irrtum.

Goethe

1.1. INTRODUCTION

PRECIPIATION of a second solid phase from solid solution is commonly used to enhance metal alloy properties. An example of this enhancement is grain size control in low alloyed steel [1], another example is precipitation hardening [2–8]. Many models exist to predict the precipitate development under given process treatment, e.g., [2, 9–12]. The goal of modelling precipitation is to establish the relation between processing parameters and the alloy composition, and the evolution of the precipitate sizes and precipitate volume fraction.

In this chapter an introduction to the Kampmann-Wagner Numerical (KWN) model is provided, a more detailed study is provided in Chapter 2. Here a particular interest is taken in the underlying ideas and physics, particularly classical nucleation and growth theory (CNGT).

Then the embedded atom method (EAM) and its descendants, e.g., modified embedded atom method (MEAM), and the reference-free modified embedded atom method (RF-MEAM), are introduced. (RF-)(M)EAM is used as a model to perform molecular dynamics (MD) simulations on various materials.

Finally the nucleation of carbides in ferrite is examined. Hereto the Guinier-Preston zone is of particular interest, as experiments show plate-like precipitates for newly nucleating precipitates.

1.2. KWN MODEL AND CLASSICAL NUCLEATION AND GROWTH

THE formation of a new phase has been studied for a long time. In the case of precipitation in alloyed metals a second solid phase forms within the bulk metal. The precipitate evolution can be divided into three stages:

- Nucleation
- Growth
- Coarsening

A schematic representation is given in Maugis and Gouné [13], reproduced in Figure 1.1. An overview is also presented by Perez et al. [14].

1.2.1. NUCLEATION

NUCLEATION is the first stage of precipitate development. The conventional theory to describe the formation of nuclei is the Classical Nucleation Theory (CNT). CNT is based on the change in the Gibbs energy ΔG linked to the formation of a precipitate in a supersaturated solid solution. Commonly spherical precipitates are assumed, this assumption will be upheld here¹ and in Chapter 2. The change in Gibbs energy, for a precipitate with radius R_{prec} , is then given as

$$\Delta G(R_{\text{prec}}) = \frac{4}{3}\pi R_{\text{prec}}^3 \Delta G_V + 4\pi R_{\text{prec}}^2 \gamma. \quad (1.1)$$

¹Precipitates are not necessarily spherical, e.g., in the work by Cheng [15] ellipsoid particles are considered. In Chapters 4 and 5 we study non-spherical carbide precipitates.

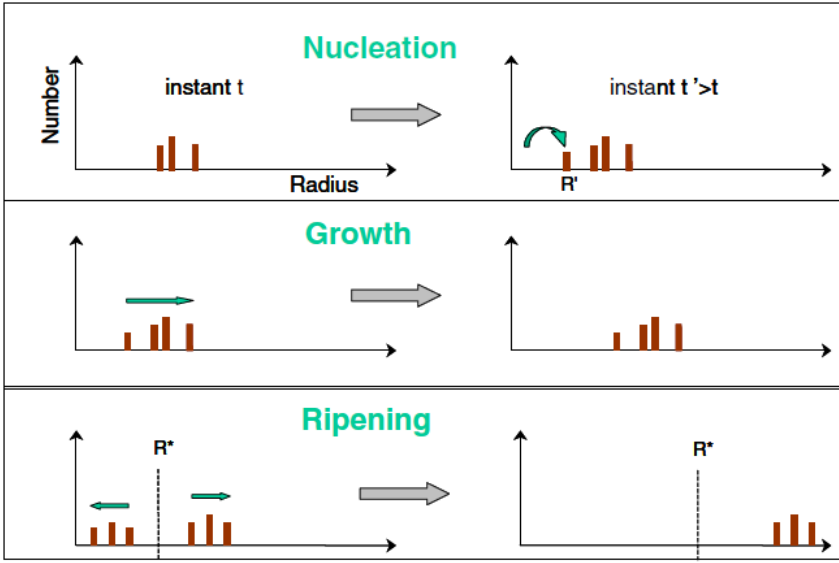


Figure 1.1: A schematic overview of the evolution of precipitates, where the number of precipitates of a specific radius evolves over time. After [13].

Here ΔG_V is the energy associated with the formation of a volume of precipitate, or chemical energy as it is associated with the solubility product of the precipitate forming elements. The other energy, γ , is the interface energy, i.e., the energy cost per unit interface area between the host material (matrix) and the precipitate. As precipitates can nucleate on different sites in the matrix a more generalised form of Eq. (1.1) is introduced.

$$\Delta G(R_{\text{prec}}) = V(R_{\text{prec}})\Delta G_V + A(R_{\text{prec}})\gamma + f(R_{\text{prec}}). \quad (1.2)$$

Where $V(R_{\text{prec}})$ is the precipitate volume, $A(R_{\text{prec}})$ the precipitate area, and $f(R_{\text{prec}})$ is a site dependent function, expressing the energy reduction for nucleation at that site. Precipitates can nucleate on different sites in the matrix, e.g., homogeneous, grain boundary, dislocations, or on other precipitates or inclusions. In these cases a different $f(R_{\text{prec}})$ is needed:

$$f(R_{\text{prec}}) = \begin{cases} 0, & \text{homogeneous} \\ -A_{\text{gb}}\gamma_{\text{gb}}, & \text{grain boundary} \\ -A_{\text{coprec}}\gamma_{\text{coprec}}, & \text{co-precipitate} \\ -\frac{\mu b^2 R_{\text{prec}} \ln(R_{\text{prec}}/b)}{2\pi(1-\nu)} - \frac{\mu b^2 R_{\text{prec}}}{5}, & \text{dislocation [16]} \end{cases} \quad (1.3)$$

Here A_{gb} is the grain boundary interface area, and γ_{gb} the associated grain boundary interface energy. For co-precipitates A_{coprec} is the co-precipitate interface area, and γ_{coprec} the associated co-precipitate interface energy. And for precipitates at dislocations μ is the shear modulus, ν is the Poisson ratio, and b is the length of the Burgers vector.

If the matrix is supersaturated with precipitate forming elements there will be an energy gain associated with the formation of a volume of precipitate ΔG_V . This gain is countered by a cost per unit area γ . The Gibbs energy is maximised for some value R^* , for this value the derivative of Eq. (1.2) with respect to R_{prec} is zero. R^* is the critical radius, and the associated ΔG^* is the activation energy. Only clusters larger than R^* can stably grow as precipitates. Clearly the critical radius depends on ΔG_V and γ , this is assessed in the sensitivity analysis in Appendix A at the end of this thesis. With the addition of precipitate growth we now have a Classical Nucleation and Growth Theory (CNGT).

Even as clusters smaller than the critical size dissolve they do exist. Unstable clusters may form in the matrix due to thermal fluctuations [17]. Their existence and distribution have been verified in Monte Carlo simulations [18, 19].

The activation energy found above is highly important in CNT. The nucleation rate is proportional to an exponent of the activation energy [20]

$$\frac{dN}{dt} \propto \exp\left(-\frac{\Delta G^*}{k_B T}\right). \quad (1.4)$$

With k_B the Boltzmann constant and T the temperature in Kelvin. This proportionality has later been expanded with a pre-factor by Becker and Döring [21], and Zeldovich [22] yielding:

$$\frac{dN}{dt} = \beta^* N_0 Z \exp\left(-\frac{\Delta G^*}{k_B T}\right). \quad (1.5)$$

Here β^* is the condensation rate of the precipitate forming elements to a precipitate of size R^* , N_0 is the number of available nucleation sites per unit volume, and Z is the Zeldovich factor. More background on the pre-factor can be found in the work of Farkas [23].

The pre-factor is derived from the idea that single particles, e.g., atoms, can attach themselves to nuclei or move away from a nucleus effectively yielding a Master equation-like formulation

$$\Gamma = \Gamma^+ - \Gamma^-. \quad (1.6)$$

Where Γ^+ is the rate at which particles attach to a cluster, and Γ^- the rate of detachment, therefore Γ is the net attachment rate. Becker and Döring [21] have found a steady-state solution to Eq. (1.6). The pre-factor has been expanded by Zeldovich [22], the Zeldovich factor Z includes the multiple re-crossing of the activation energy barrier in the nucleation rate, as it relates the flatness of the free energy to the nucleation rate. The Zeldovich factor accounts for the effect of thermal fluctuations on clusters at the critical size. Effectively this means that precipitates at the critical size have a probability to grow less than one, and will not automatically grow to stable precipitates. Detailed studies in this subject can be found in [24, 25]. The Zeldovich factor is given as

$$Z = \sqrt{\frac{-\frac{\partial^2 \Delta G(R_{\text{prec}})}{\partial N^2} \big|_{R_{\text{prec}}=R^*}}{2\pi k_B T}} = \sqrt{\frac{-1}{2\pi k_B T} \frac{(\Delta G)''(R^*)}{(R^*)^4} \frac{v_{\text{at}}^2}{16\pi^2}}. \quad (1.7)$$

Where $(\Delta G)''(R^*)$ is the second derivative of the Gibbs energy with respect to the number of precipitates at the critical radius, and ν_{at} is the atomic volume of the precipitate.

Additionally an incubation time τ for the formation of stable clusters from an over-saturated solution may be added, examples are found in Russell [26], Kampmann and Wagner [11], and Shneidman and Weinberg [27]. The incubation time allows for a transient nucleation regime, meaning that the steady-state nucleation rate is not instantly reached by the system due to the finite diffusivity of precipitate forming elements. Depending on the nature of the system the significance of the incubation time may be limited as found in this study [28].

The number of available nucleation sites will decrease as nuclei form, thus the N_0 pre-factor may be written as $N_{\text{total}} - N(t)$. The final form of the change in the number of particles per unit volume with time is then given as

$$\frac{dN}{dt} = (N_{\text{total}} - N(t)) \beta^* Z \exp\left(-\frac{\Delta G^*}{k_B T}\right) \exp\left(-\frac{\tau}{t}\right). \quad (1.8)$$

MASTER EQUATION

Attachment of atoms to a precipitate can, as mentioned above, be described by a master equation. This has been worked out by Korepanova *et al.* [29] for titanium and niobium carbide precipitates. In [29] two rates are defined: α_n a monomer emission from clusters of size- n (i.e. a precipitate consisting of n atoms), and β_n the rate of monomer absorption by size- n clusters.

$$\alpha_n = \beta_{n-1} C_{\text{eq}}^{\text{sol}} \exp\left[\frac{A(\gamma n^{2/3} - \gamma(n-1)^{2/3})}{k_B T}\right]. \quad (1.9)$$

$$\beta_n = 4\pi r_n D / V_{\text{at}}^m. \quad (1.10)$$

Here r_n is the radius of the size- n cluster, D is the thermal diffusion coefficient of solute atoms in the system, $C_{\text{eq}}^{\text{sol}}$ is the equilibrium concentration of solute atoms, and V_{at}^m is the atomic volume of the alloy matrix.

Then the uniform concentration of size- n clusters C_n is described by

$$\frac{dC_n}{dt} = \beta_{n-1} C_1 C_{n-1} - (\alpha_n + \beta_n C_1) C_n + \alpha_{n+1} C_{n+1}, \quad n \neq 1. \quad (1.11)$$

For clusters where $n = 1$

$$\frac{dC_1}{dt} = -2\beta_1 C_1 C_1 + \alpha_2 C_2 + \sum_{i=2}^{N_{\text{max}}} [\alpha_i - \beta_i C_1] C_i, \quad (1.12)$$

where N_{max} is the maximal cluster size.

Korepanova *et al.* have rewritten these equations in a Fokker-Planck partial differential equation [29]. For both titanium and niobium carbide it has been demonstrated that this master equation (or cluster expansion) method can describe the nucleation and growth of precipitates.

1.2.2. GROWTH

THE second stage is growth, as part of this study it has been seen that nucleation and growth might occur simultaneously [28], cf. Chapter 2. The growth of an individual precipitate with radius R_{prec} is approximated as proposed by Zener [30]:

$$\frac{dR_{\text{prec}}}{dt} = \frac{D_{\text{eff}}}{R_{\text{prec}}} \frac{C - C^e \exp(R_0/R_{\text{prec}})}{C^P - C^e \exp(R_0/R_{\text{prec}})}, \quad (1.13a)$$

where $R_0 = 2\gamma\nu_{\text{at}}(k_B T)^{-1}$ as defined in [2], which is the critical radius for homogeneous precipitation. The average radius of a distribution of precipitates, in a material where nucleation also takes place besides the already existing precipitates is:

$$\frac{d\bar{R}_{\text{prec}}}{dt} = \frac{D_{\text{eff}}}{\bar{R}_{\text{prec}}} \frac{C - C^e \exp(R_0/\bar{R}_{\text{prec}})}{C^P - C^e \exp(R_0/\bar{R}_{\text{prec}})} + \frac{1}{N} \frac{dN}{dt} (\alpha_n R^* - \bar{R}_{\text{prec}}), \quad (1.13b)$$

For averaging the radii of the growing precipitates the approximation $\overline{f(R)} = f(\bar{R})$ has been used. There are two terms in Eq. (1.13b), the first term gives the growth of already existing precipitates. The second term in Eq. (1.13b) is due to the new nuclei, where α_n is a numerical factor to only allow growth of nucleated precipitates that are (slightly) larger than the critical radius.

The growth rate in Zurob's model is made for precipitates at dislocations only. For growth of precipitates in the matrix and on grain boundaries equations similar to Eq. (1.13a) can be derived. The effective diffusion coefficient depends on the nucleation site, ref. [10] expands on the site dependent diffusion. This is worked out in Vonk's thesis [31].

$$D_{\text{eff}} = \begin{cases} D_{\text{pipe}} \pi R_{\text{core}}^2 \rho + D_{\text{bulk}} (1 - \pi R_{\text{core}}^2 \rho), & \text{dislocation} \\ D_{\text{gb}} \frac{3\delta_{\text{gb}}}{2R_{\text{grain}}} + D_{\text{bulk}} \left(1 - \frac{3\delta_{\text{gb}}}{2R_{\text{grain}}}\right), & \text{grain boundary} \\ D_{\text{bulk}}. & \text{homogeneous} \end{cases} \quad (1.14)$$

Where ρ is the dislocation density, R_{grain} is the radius of a grain, and δ_{gb} is the thickness of the grain boundary. Note these equations are all independent of the precipitate radius.

In Equation (1.14) R_{core} is the radius of the dislocation core. In ref. [9] it is taken to be equal to the length of the Burgers vector b .

1.2.3. COARSENING

WHEN the chemical energy and the surface energy (see Equation (1.1)), summed over all precipitates, become of the same order of magnitude a reduction of both terms starts by the growth of larger precipitates and the shrinking of smaller precipitates. This process is known as the coarsening of precipitates. To describe coarsening there are multiple approaches.

LIFSHITZ-SLYOZOV-WAGNER MODEL

After the initial nucleation phase the Lifshitz-Slyozov-Wagner (LSW) model [32, 33] provides a model for coarsening of the precipitates. A classical investigation of coarsening

can be traced to Ostwald [34]. Ostwald's idea is that there are two phases, of which one has a much smaller volume fraction, first the minority phase nucleates. The oversaturation of the matrix causes nucleation as mentioned earlier. The oversaturation is lowered by the formation of the minority phase, which lowers the Gibbs energy of the system. When the oversaturation becomes small enough the Gibbs energy will mainly be lowered by reducing the majority-minority, or matrix-precipitate, interface energy. To reduce the interface energy, the total interface area is reduced which causes large particles to grow and small particles to dissolve [35]. The LSW-theory seeks to quantify the coarsening described by Ostwald. Further details concerning Ostwald ripening and its descendants can for instance be found in Niethammer [36] and Baldan [35].

In the work by Ardell [37] the LSW model is modified to account for the volume fraction of precipitate, the original LSW-theory coincides with the limit case for the volume fraction $Q \rightarrow 0$. The modification comes from the assumption that the solute diffusion depends on a characteristic distance between the precipitate and the solute atom. Ardell's modification to the LSW model is known as MLSW. In ref. [38] the diffusion of solute atoms is examined more closely. It seeks to combine grain boundary diffusion and matrix diffusion, where the diffusion through the matrix is slower than along the grain boundary.

AVERAGE SIZE MODEL

The nucleation, growth and coarsening models need to be combined to cover the complete evolution of precipitation. One type of model that can be used to estimate the size of precipitates is the average size model. The model approximates the evolution of the average precipitate size of a distribution of precipitates.

For a precipitation model the idea is to integrate nucleation, growth and coarsening into one model. One paper in which the three steps in the precipitation process are unified is [2]. Here both homogeneous precipitation is considered and precipitation on dislocations. There are two main domains with different governing kinetics:

- A nucleation and growth regime.
- A growth and coarsening regime.

They also propose a simple criterion to separate these regimes:

$$-\frac{dN}{dt}|_{\text{growth+coars}} > \frac{dN}{dt}|_{\text{nucleation}}. \quad (1.15)$$

The presented model provides a method to describe the competitive kinetics of heterogeneous and homogeneous precipitation. Also it is coupled to a model for hardening, the hardening model allows taking into account the distribution of precipitation size.

In the average size models the equations for the number density of precipitates and mean radius are given in two regimes, that of nucleation and growth and of growth and coarsening. Note that in the distribution models this transition occurs automatically, in which the distribution shape changes as described later in this section.

The rate of nucleation and growth in the nucleation and growth regime are described in sections 1.2.1 and 1.2.2. However in the growth and coarsening regime, there is a different formulation for the change in the number of particles per unit volume with time, and a different growth rate:

$$\frac{dN}{dt}|_{\text{coarse}} = F_c \left(\frac{4}{27} \frac{C^e}{C^P - C^e} \frac{R_0 D_{\text{eff}}}{\bar{R}_{\text{prec}}^3} \right) \left(\frac{R_0 C}{\bar{R}_{\text{prec}} (C^P - C)} \left(\frac{3}{4\pi \bar{R}_{\text{prec}}^3} - N \right) - 3N \right), \quad (1.16)$$

$$\frac{d\bar{R}_{\text{prec}}}{dt} = (1 - F_c) \frac{d\bar{R}_{\text{prec}}}{dt}|_{\text{growth}} + F_c \frac{d\bar{R}_{\text{prec}}}{dt}|_{\text{coarse}}. \quad (1.17)$$

Where the growth and coarsening equations are given as [2]:

$$\frac{d\bar{R}_{\text{prec}}}{dt}|_{\text{growth}} = \frac{D_{\text{eff}}}{\bar{R}_{\text{prec}}} \frac{C - C^e \exp(R_0/\bar{R}_{\text{prec}})}{C^P - C^e \exp(R_0/\bar{R}_{\text{prec}})}, \quad (1.18)$$

$$\frac{d\bar{R}_{\text{prec}}}{dt}|_{\text{coarse}} = \frac{4}{27} \frac{C^e}{C - C^e} \frac{R_0 D_{\text{eff}}}{\bar{R}_{\text{prec}}^2}. \quad (1.19)$$

Here the parameter F_c is the coarsening factor, i.e. it indicates a coarsening fraction [2]². The fraction is necessary as for “average size” models the transition from nucleation and growth to coarsening needs to be explicitly included, whereas for “distribution models” this transition is implicitly present. The fraction is designed to create a more natural transition from the nucleation to the coarsening regime.

Deschamps formulates it as:

$$F_c = 1 - \text{erf} \left(4 \left(\frac{R_{\text{prec}}}{R_0} \ln \left[\frac{C}{C^e} \right] - 1 \right) \right). \quad (1.20)$$

But different formulations exist, for example [40]:

$$F_c = 1 - \text{erf} \left(4 \left(\frac{R_{\text{prec}}}{R_0} \right) - 1 \right). \quad (1.21)$$

KAMPMANN-WAGNER NUMERICAL MODEL

The average size model will only provide an approximation for the evolution of the average of the precipitate size distribution, this is a limited view as there are many differently sized precipitates. An approximation in this model is that the average of the growth rate is not the average of the r.h.s. term in Equation (1.13a), but that R_{prec} in the r.h.s. is replaced by the average \bar{R}_{prec} . The magnitude of the inaccuracy of this approximation is not well-known. Therefore an improved model is needed, hereto we will use the model introduced by Kampmann and Wagner [41]. The model has been further developed by various others, among them Robson [42].

The KWN model describes the evolution of the size distribution, and as will be shown

²Note that Equation (1.19) only describes the growth rate for homogeneous precipitates, to include precipitates on dislocations the Equation needs to be modified cf. [38, 39].

later, has been expanded to multiple and complex precipitates. In the formulation of Den Ouden [43] a function $\varphi(R_{\text{prec}}, t)$ denoting the number density distribution of precipitates with radius R_{prec} at time t is introduced. Den Ouden formulated his model for homogeneous precipitation. Vonk [31] expanded the KWN model of Den Ouden by adding precipitation on dislocations and grain boundaries, using the approximations for the nucleation and growth rate from Zurob's model [9]. The approach by Vonk [31] will be followed.

Using this more complex model will also increase the level of complexity in solving the equations. Note that the eqs. (1.8, 1.13a, 1.16 & 1.17) are all ordinary differential equations with only time as an independent variable. This allows the use of solvers like Runge-Kutta. However the KWN model using the distribution function $\varphi(R_{\text{prec}}, t)$ is more complicated. Here there are two independent variables, time and precipitate radius. The time evolution is given in a partial differential equation:

$$\frac{\partial \varphi}{\partial t} = -\frac{\partial[\nu \varphi]}{\partial R_{\text{prec}}} + S, \quad (1.22)$$

where $\nu = \nu(R_{\text{prec}}, t)$ is the growth rate of the precipitates with radius R_{prec} at time t . And $S = S(R_{\text{prec}}, t)$ is a source function, it represents the nucleation of particles of size R_{prec} at time t . In Den Ouden [12] it is defined as:

$$S(R_{\text{prec}}, t) = I(t)\delta(R_{\text{prec}} - R_n(t)). \quad (1.23)$$

The nucleation rate $I(t)$ comes directly from Zurob, eq. (1.8), and $R_n(t)$ is the critical radius at time t . Finally δ is the Dirac delta function.

In a similar way the growth rate $\nu(R_{\text{prec}}, t)$ is linked to the Zurob model, it is taken equal to eq. (1.18).

Some notes to the KWN model:

- With the KWN model there is no need to explicitly define the transition from a nucleation-growth to a growth-coarsening regime: as this transition takes place automatically in the distribution type model.
- The KWN model also assumes that the precipitates are spherical, we have already noted that this might be a poor approximation to the particles in the section on CNT (section 1.2.1).

MULTI-COMPONENT MATRIX KWN MODEL

Using the KWN model as defined above it can be extended to also cover precipitation in a multi-component matrix. That is the nucleation and growth rate can be adapted to include the diffusion of all alloying elements in the matrix, rather than only the precipitate forming elements (cf. Den Ouden [43]). This is a useful method to model a system in which multiple different types of precipitates may form. In the multi-component matrix KWN model the Zeldovich factor³ and atomic attachment rate β^* need to be altered.

³Indirectly due to its dependence on the chemical energy ΔG_ν , unlike the atomic attachment rate which depends directly on the diffusion coefficients of all alloying elements.

First the Zeldovich factor Z can be found in eq. (1.7). This can be worked out into (cf. Vonk [26, 31]):

$$Z = \frac{v_{at}}{2\pi\sqrt{k_B T}} \sqrt{-R_n \Delta G_v - \gamma + \frac{\mu b^2}{16\pi^2(1-\nu)R_n} \left(\frac{1}{R_n}\right)^2}. \quad (1.24)$$

Which is valid for dislocations. Again there is a dependence on nucleation site. For homogeneous sites we would get:

$$Z = \frac{v_{at}}{2\pi\sqrt{k_B T}} \sqrt{-R_n \Delta G_v - \gamma \left(\frac{1}{R_n}\right)^2}. \quad (1.25)$$

For precipitates at grain boundaries or co-precipitates the interface energy term is the only property that changes to $\gamma - \gamma_{gb}$ or $\gamma - \gamma_{coprec}$ respectively.

For the atomic attachment rate for precipitates at dislocations the following formulation is commonly presented for the KWN model

$$\beta^* = \frac{4\pi R_n^2 D_{X,pipe} x_X^M}{a^4}, \quad (1.26)$$

where $D_{X,pipe}$ is the pipe diffusion for the slowest diffusing element⁴ X [26], and x_X^M is the molar fraction of X . Den Ouden [43] has improved Eq. (1.26) to include all alloying elements present in the system.

For complex precipitates the chemical energy becomes a weighted function of the energies of the pure carbides and nitrides of which the precipitate consist:

$$\Delta G_v = -\frac{k_B T}{v_{at}} \ln \left(\frac{\text{matrix product}}{\text{solubility product}} \right). \quad (1.27)$$

Where the matrix product is the product of the weight percentages of the precipitate forming elements in the matrix, to the power of the stoichiometric ratio Eq. (1.28). The solubility product the product of equilibrium weight percentages Eq. (1.29).

$$\text{matrix product} = wt\% X^M (wt\% C^M)^x (wt\% N^M)^{1-x}, \quad (1.28)$$

and

$$\text{solubility product} = wt\% X^{Eq} (wt\% C^{Eq})^x (wt\% N^{Eq})^{1-x}. \quad (1.29)$$

Where X, C, N are the metal, carbon and nitrogen fractions respectively. Here the superscript M refers to the actual matrix weight percentage, and Eq to the equilibrium weight percentage.

At this point several models concerning the full precipitate development have been introduced. A drawback for the multi-component KWN model is that simulation times, and computational demand is high when simulating the development of precipitates. In

⁴The diffusion coefficient is temperature dependent, so the slowest diffusing element can change when temperature is varied.

Chapter 2 the multi-component KWN model will be looked into, where a quick approximation and characteristic times for the model are presented. This can reduce simulation times greatly, also increasing the efficiency of simulations. In Appendix A the sensitivity of the KWN model is briefly investigated, to provide another insight in the KWN model.

1.3. INTERATOMIC POTENTIALS FOR MOLECULAR DYNAMICS

MODELS based on Classical Nucleation and Growth Theory provide a macroscopic picture of the development of precipitates in alloys. These models have proved to be useful when predicting the material properties of precipitate populations in alloys. There are however, two main questions regarding the CNGT models: Firstly the parameter values as used in the models need to be determined. Either by experiment, or from atomistic models; And secondly, the macroscopic models use assumptions of which the validity and accuracy is unknown.

In order to address the atomistic picture and to test (some of) the assumptions in the model Molecular Dynamics (MD) simulations can be used. In MD simulations an alloy can be built atom-by-atom and simulated to provide parameter values, like for instance the interface energy between the matrix and the precipitate. Furthermore, formed clusters and precipitates can be analysed in more detail providing much more insight in the formation of precipitates, the latter is done in Chapters 4 and 5. MD simulations require an interatomic potential. Most importantly an interatomic potential capable of accurately predicting experimental material properties. In the last decades several methods to construct such a potential have been developed, here a historical overview is given to get an impression of the lead-up to the current state-of-art.

1.3.1. EARLY POTENTIALS

INTERATOMIC interactions have been studied for a long time. Two particular potentials are of historical significance, namely the Lennard-Jones potential [44–46] and the Morse-potential [47, 48]. Both were originally published in the 1920's.

The Lennard-Jones (LJ) potential is widely used and surprisingly effective, even though it has a relatively simplistic analytical form

$$V_{LJ}(R) = 4\epsilon \left[\left(\frac{\sigma}{R} \right)^{12} - \left(\frac{\sigma}{R} \right)^6 \right]. \quad (1.30)$$

Here R is the distance separating the interacting particles, σ is the distance where the potential energy is zero, and ϵ is the 'well-depth', i.e., the depth of the potential well, a generalised example is shown in Figure 1.2. The LJ potential has a minimum at $R_m = 2^{1/6}\sigma$ where the potential energy is $-\epsilon$. Important to see is that the LJ potential incorporates three important domains that are observed in two body interactions⁵;

- At short distances, particles repel each other. Which is found to be true in the hard-nucleus model for atoms as we currently accept it.
- At long distances, the particles do not really influence each other.

⁵This is not only true for atoms, but also in for example planetary orbits

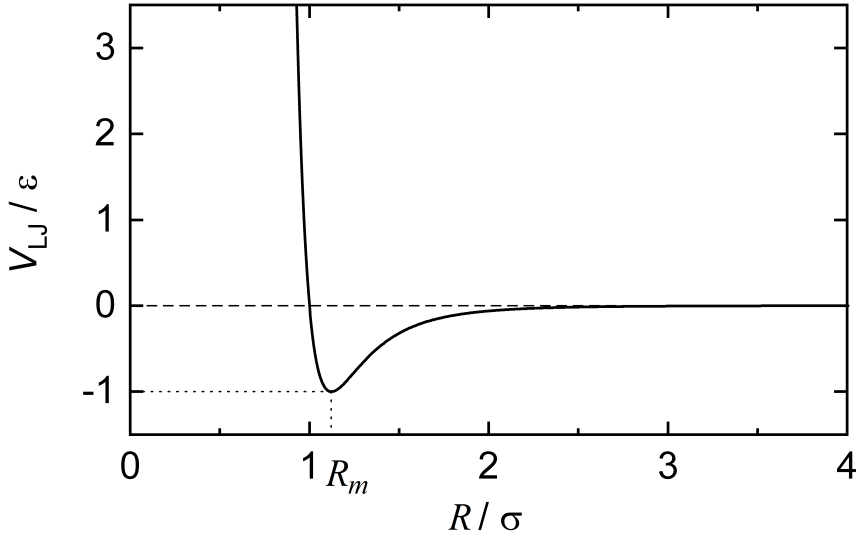


Figure 1.2: Example Lennard-Jones potential, where the energy is scaled with respect to ϵ , and the radius with respect to σ .

- At the intermediate range particles are attracted to be separated by a distance R_m .

The material described by the LJ potential is often referred to as ‘Lennard-Jonesium’ and shows very realistic behaviour in statistical mechanical simulations. Moreover, when ϵ and σ are set to real material properties the potential may be used to describe simple substances like noble gases.

The origins of the terms in Eq. (1.30) are traced to the Pauli repulsion for the repulsive $1/R^{12}$ term. The attraction $1/R^6$ term describes the dispersion force, the factor 6 is proven from quantum-chemical calculations which show a decay of $1/R^6$ for the dispersive contribution. Originating from (correlated) dipole-dipole interactions due to fluctuations in the charge densities in the atoms. The $1/R^{12}$ is mainly used as it is the square of the $1/R^6$ which makes it computationally convenient, and it approximates the Pauli repulsion reasonably well.

The LJ potential has been widely studied, and is still relevant today, therefore any handbook on (computational) statistical mechanics or solid state physics will cover it which we shall not repeat here, rather for theory and worked examples cf. [49, 50] statistical mechanics, [51] solid state physics, or [52] computational physics.

The Morse potential has been developed from the quantified harmonic oscillator, like for instance in an Einstein solid. Like de LJ potential there are just two parameters, therefore the Morse potential is computationally friendly. The potential is given as

$$V_M(R) = D_e (1 - e^{-a(R-R_e)})^2. \quad (1.31)$$

Again R is the interatomic distance, R_e is the core distance with the smallest potential energy, D_e is the spectroscopic dissociation energy, and a is a constant controlling the

width of the potential well. When $R \approx R_e$ the Morse potential resembles the harmonic oscillator with a spring constant k_e :

$$V_{\text{Harm.}}(R) = \frac{1}{2} k_e (R - R_e)^2. \quad (1.32)$$

When the exponential function is expanded in terms of $R - R_e$ the Morse potential transforms directly into a harmonic oscillator with $k_e = 2D_e a^2$:

$$V_{\text{M-Harm.}}(R) = D_e a^2 (R - R_e)^2. \quad (1.33)$$

Again there is a strong repulsion for small R and a diminishing of the potential well for $R \rightarrow \infty$, as the energy converges to D_e . And in between there is an attractive potential well like with the LJ potential. Again this potential is commonly described in literature, for instance in [50] or [52].

For these basic interaction potentials it is possible to describe some materials quite well. The use of an interatomic potential to describe a material, and particularly to study point-defects like vacancies or interstitials has received a lot of interest over time. A study on point defects in iron was conducted by Johnson [53], but earlier studies with a similar potential form were conducted on copper [54–56]. The development of such potentials goes back to Huntington [57] and Tewordt [58].

In the iron potential Johnson [53] considers each atom in the supercell⁶, a spherical crystallite, as an individual particle. An atom is placed at the centre of the crystallite and the surrounding atoms are considered symmetrically equivalent. Atoms outside of the crystallite are treated as if they were embedded in some elastic continuum. Johnson uses a displacement field \mathbf{u} , it is given by

$$\mathbf{u} = -C\nabla(1/r) = C(\mathbf{r}/r^3), \quad (1.34)$$

where C is the strength of the displacement field. Each atom i has a displacement given by

$$\mathbf{u}^i = C \left[\mathbf{r}_0^i / (r_0^i)^3 \right]. \quad (1.35)$$

The r_0 indicates that these displacements are evaluated at the perfect lattice position, cf. [55]. The energy of the crystallite is given as

$$E = \frac{1}{2} \sum_{i,j} \phi_{ij} + \sum_{i,k} \phi_{ik} + aC + bC^2. \quad (1.36)$$

Here ϕ_{ij} represents the interaction potential between atoms i and j , where the summation over i sums over all atoms in the spherical crystallite. The summation over j indicates atoms in the crystallite that interact with atom i , and the summation over k indicates the interaction with atoms outside the crystallite. The perfect lattice energy is labelled E_0 ,

$$E_0 = \frac{1}{2} \sum_{i,j} \phi_{ij}^0 + \sum_{i,k} \phi_{ik}^0. \quad (1.37)$$

⁶The space considered within a simulation containing all atoms.

The force on atom i due to atoms j and k is given by the derivative of the energy

$$F_i = -\frac{\partial E}{\partial \mathbf{r}_i} = \sum_j F_{ij} + \sum_k F_{ik}. \quad (1.38)$$

Parameters a and b from Eq. (1.36) are derived from perfect lattice conditions and elasticity theory. In the original paper [55] it is noted that both terms do not have a significant effect on the presented results, here we might add that this is not necessarily the case for other metals. The term aC is needed to include the work done countering the forces required to maintain the perfect lattice in equilibrium, and bC^2 includes the energy stored in the elastic field [53].

The iron potential by Johnson [53] was made in 1964, but it produces quite reasonable results. However with growing computational power potentials with more parameters, and therefore more detail, have become a more feasible option. This brings us to a more recent development, which is still used albeit in a modified form.

1.3.2. EMBEDDED ATOM METHOD, FINNIS-SINCLAIR, AND GLUE POTENTIALS

IN the 1980's Daw and Baskes have proposed the Embedded Atom Method (EAM) [59, 60]. Their work generalises the quasi-atom theory to uniformly treat all atoms. Each atom is embedded in a host lattice which consists of all other atoms, and an electron density is used resulting in a better treatment of impurities. More importantly, their method is not much more complicated than pair potentials, yet it is capable of describing more complicated systems. The total energy of a system is then given in Eq. (1.39).

$$E_{\text{tot}} = \sum_i F_i(\rho_i(r_i)) + \frac{1}{2} \sum_{i,j} \phi(r_{ij}). \quad (1.39)$$

Where $\phi(r_{ij})$ are the pair potential contributions for atoms i and j separated by a distance r_{ij} , and $F_i(\rho_i(r_i))$ is the embedding energy function for atom i at with $\rho_i(r_i)$ the local electron density.

The EAM formalism may be fitted to comply with material properties perfectly. This is a mathematical consequence as one may use more pair potential or local electron density terms to generate a system of equations with an equal number of unknowns and equations. The danger here is that this can easily lead to overfitting. Some examples of material properties used for parameter fitting are, the cohesive (sublimation) energy, vacancy formation energy, and elastic constants [60, 61]:

$$\begin{aligned} E_{\text{coh}} &= - \left[F(\bar{\rho}) + \frac{1}{2} \bar{\phi} \right], \\ E_{\text{vac}}^f &= -\frac{1}{2} \bar{\phi} + \sum_m [F(\bar{\rho} - \rho_m) - F(\bar{\rho})] + E_{\text{relax}}. \end{aligned} \quad (1.40)$$

Where $\bar{\rho} = \sum_m \rho(a^m)$, and $\bar{\phi} = \sum_m \phi(a^m)$. Here a^m are distances between neighbours. Using the EAM formalism many potentials have been created as they are effective and

easy to use.

A subtype of EAM potentials is the Finnis-Sinclair potential [62]. The scheme designed by Finnis and Sinclair is easy to use on various systems. In their original work they have used it to generate potentials for bcc metals vanadium, niobium, tantalum, chromium, molybdenum, tungsten and iron. Later Foiles *et al.* [63], and Ackland *et al.* [61, 64] have used it for fcc metals gold, silver, copper, palladium, platinum and nickel as well as some of the original bcc metals from Finnis and Sinclair.

The EAM formalism can also be applied to alloys, e.g., nickel-aluminium [65], or alloys of fcc metals in [63].

Another subtype of EAM potentials is the ‘glue’ model or ‘glue’ potential by Ercolessi *et al.* [66–68]. A comprehensive review article on EAM potentials was written by Daw, Foiles and Baskes [69].

As the EAM formalism is so powerful it has been used well into the 2000’s [70–74] to give some examples. Where the potentials for iron by Mendeleev and Ackland *et al.* [70, 71] are highly successful for describing point defects in irradiated iron.

With the growth of computational power these more modern EAM potentials have been fitted to more input data, for instance the potential of Mendeleev *et al.* [70] was in part fitted to the interatomic forces in liquid (molten) iron. In addition it may be observed that many EAM potentials of this era adhere to a common analytical form. As this analytical form is important to the further work in this dissertation it is worthwhile to pause a moment to fully appreciate it. For notational consistence the notation of Duff *et al.* [75] is adopted. The total energy (for a system of N atoms) of Eq. (1.39) is rewritten as:

$$E_{\text{tot}} = \sum_{i=1}^N E_{\alpha_i}^{\text{emb}}(\rho_i) + \frac{1}{2} \sum_{i \neq j}^N \sum_{j=1}^N \phi_{\alpha_i, \alpha_j}(r_{ij}). \quad (1.41)$$

Where α is the atom-type, $E_{\alpha_i}^{\text{emb}}(\rho_i)$ is the embedding energy function of the i^{th} atom of type alpha with ρ_i the (fictitious) local electron density at site i , and $\phi_{\alpha_i, \alpha_j}(r_{ij})$ the pair-potential function for atoms i and j separated by distance r_{ij} . The embedding energy function is given as:

$$E_{\alpha}^{\text{emb}}(\rho) = a_{\alpha} \rho^{\frac{1}{2}} + b_{\alpha} \rho^2 + c_{\alpha} \rho^3 + d_{\alpha} \rho^4. \quad (1.42)$$

Where $a_{\alpha}, b_{\alpha}, c_{\alpha}$ and d_{α} are fitting parameters⁷. A crude version of this form with only the a_{α} term can be observed in the work of Finnis and Sinclair [62]. The local electron density is given by:

$$\rho_i = \rho_i^{(0)} = \sum_{j \neq i}^N f_{\alpha_j}^{(0)}(r_{ij}). \quad (1.43)$$

Where the (0) is foreshadowing the more recent additions to the EAM formalism in the RF-MEAM formalism, which is discussed further in Section 1.3.4. The functions $f_{\alpha_j}^{(0)}(r)$ are partial electron density contributions which are given as sums over cubic splines:

$$f_{\alpha_j}^{(0)}(r) = \sum_{n=1}^m a_{\alpha_i}^{(n,0)} (r_{\alpha_i}^{(n,0)} - r)^3 H(r_{\alpha_i}^{(n,0)} - r). \quad (1.44)$$

⁷In the original article by Duff *et al.* d_{α} is not included, however it is included in the *MEAMfit* code

Where $H(\dots)$ is the Heaviside function, and m the number of splines used. This form is used in many EAM potentials, as its first and second derivative are continuous for all values of r [61]. The same holds for the pair-potentials,

$$\phi_{\alpha_i, \alpha_j}(r) = \sum_{n=1}^k b_{\alpha_i, \alpha_j}^{(n)} \left(s_{\alpha_i, \alpha_j}^{(n)} - r \right)^3 H \left(s_{\alpha_i, \alpha_j}^{(n)} - r \right). \quad (1.45)$$

Where k splines are used in the potential. The parameters that are optimised in a fit are $a_{\alpha_i}^{(n,0)}$, $r_{\alpha_i}^{(n,0)}$, $b_{\alpha_i, \alpha_j}^{(n)}$ and $s_{\alpha_i, \alpha_j}^{(n)}$.

Several variations to this analytical form exist. Firstly, in some cases a selection of the fit-parameters are fixed, e.g., $a_\alpha = -1$ in the iron potential in [70, 71]. Secondly, as it may be overwhelming to fit all parameters at once the cut-off radii, i.e., $r_{\alpha_i}^{(n,0)}$ and $s_{\alpha_i, \alpha_j}^{(n)}$ are fixed, e.g., for iron, iron-phosphorus, and iron-vanadium [70–72]. A more significant change is the use of quartic splines like in [72].

Even though quite a wide selection of (recent EAM) potentials use the cited form or can be algebraically rewritten in the cited form (*cf.* Timonova and Thijsse [76]), some potentials are actually quite different, like for instance the carbon potential of Hepburn and Ackland [74]. So some caution is warranted before generalising all EAM potentials.

Some remarks regarding the EAM potential need to be made. Despite its good performance for some systems, it performs quite poorly for systems in which directional bonding plays a role [77]. This includes semi-conductors and metals with a bcc or hcp structure with a non-ideal c/a ratio, which is the case for most elements in the early and middle transition metals group. The EAM formalism is not made to include angular contributions in the local electron density function, this is key to understanding its limited success or outright failure to describe systems with directional bonding.

1.3.3. MODIFICATION AND IMPROVEMENT

ANGULAR contributions to the local electron density were not included in the original EAM formalism, resulting in poor performance for systems in which directional bonding plays a role [77]. The solution is, rather obviously, to include angular terms, this was done for example in silicon and germanium systems [78, 79]. Further developments in this direction have given rise to the Modified Embedded Atom Method (MEAM). These MEAM potentials as introduced by Baskes only make use of the first nearest-neighbours (1NN) [80].

In the early 2000's Lee et al. have published more work on second nearest-neighbour (2NN) MEAM potentials [81, 82]. Following Lee we note that the 2NN distance in bcc structures is only about 15% larger than the 1NN distance. This indicates that one cannot simply neglect these higher order neighbours. This proves necessary as the 1NN MEAM potential for iron can reproduce the elastic constants and several point defects quite well, however free surface energies are far off as demonstrated by Lee and Baskes [81].

The 2NN MEAM potentials have seen a wide use in the 2000's and are still relevant for many materials. They have also been used for niobium and titanium carbides and nitrides in iron [83, 84]. In particular interface energies between the precipitate and pure iron in flat interfaces were studied.

The MEAM formalism uses a similar description for the total energy of a system as EAM.

$$E_{\text{tot}} = \sum_{i=1}^N F_i^{\text{emb}}(\bar{\rho}_i) + \frac{1}{2} \sum_{i \neq j}^N \sum_{j=1}^N \phi_{i,j}(r_{ij}). \quad (1.46)$$

Where $F_i^{\text{emb}}(\rho_i)$ is the embedding energy function at site i with $\bar{\rho}_i$ the background electron density at site i , and $\phi_{i,j}(r_{ij})$ the pair-potential function for atoms i and j separated by distance r_{ij} . The embedding energy function is given as:

$$F^{\text{emb}}(\bar{\rho}) = AE_C \left(\frac{\bar{\rho}}{\rho^0} \right) \ln \left(\frac{\bar{\rho}}{\rho^0} \right). \quad (1.47)$$

Where A is an adjustable parameter, E_C is the sublimation energy, and $\bar{\rho}^0$ is the background electron density for a reference structure (commonly the reference structure is the preferred structure at 0 K).

The background electron density $\bar{\rho}_i$ is given by:

$$\left(\rho_i^{(0)} \right)^2 = \left[\sum_{j \neq i}^N \rho_j^{a(0)}(r_{ij}) \right]^2, \quad (1.48a)$$

$$\left(\rho_i^{(1)} \right)^2 = \sum_{\alpha} \left[\sum_{j \neq i}^N \left(\frac{r_{ij}^{\alpha}}{r_{ij}} \right) \rho_j^{a(1)}(r_{ij}) \right]^2, \quad (1.48b)$$

$$\left(\rho_i^{(2)} \right)^2 = \sum_{\alpha, \beta} \left[\sum_{j \neq i}^N \left(\frac{r_{ij}^{\alpha} r_{ij}^{\beta}}{r_{ij}^2} \right) \rho_j^{a(2)}(r_{ij}) \right]^2 - \frac{1}{3} \left[\sum_{j \neq i}^N \rho_j^{a(2)}(r_{ij}) \right]^2, \quad (1.48c)$$

$$\left(\rho_i^{(3)} \right)^2 = \sum_{\alpha, \beta, \gamma} \left[\sum_{j \neq i}^N \left(\frac{r_{ij}^{\alpha} r_{ij}^{\beta} r_{ij}^{\gamma}}{r_{ij}^3} \right) \rho_j^{a(3)}(r_{ij}) \right]^2 - \frac{3}{5} \sum_{\alpha} \left[\sum_{j \neq i}^N \left(\frac{r_{ij}^{\alpha}}{r_{ij}} \right) \rho_j^{a(3)}(r_{ij}) \right]^2. \quad (1.48d)$$

For the density $\rho_j^{a(h)}$ represents the electronic density due to an atom j at a distance r_{ij} from site i . r_{ij}^{α} is the α -component of the distance vector between atoms i and j .

The total background electron density combined as⁸

$$\bar{\rho}_i = \rho_i^{(0)} G(\Gamma), \text{ with } G(\Gamma) = \frac{2}{1 + e^{-\Gamma}}. \quad (1.49)$$

Here

$$\Gamma = \sum_{h=1}^3 t_i^{(h)} \left[\frac{\rho_i^{(h)}}{\rho_i^{(0)}} \right]^2, \quad (1.50)$$

for which $t_i^{(h)}$ are adjustable (fit-)parameters. The electron density $\rho_j^{a(h)}$ is described by

$$\rho_j^{a(h)}(R) = e^{-\beta^{(h)}(R/r_e-1)}. \quad (1.51)$$

⁸The combination is not unique, the presented version is used by Lee *et al.* [81].

$\beta^{(h)}$ is a fit parameter and r_e is the nearest-neighbour distance in the equilibrium reference structure.

A noteworthy short-coming of MEAM potentials in general is the need to comply with the Rose zero-temperature universal equation of state for a given structure. The Rose equation of state [85] fixes the pair-potential, reducing freedom, but simultaneously introduces a (physically observed) “*logarithmic dependence of the bond length on the number of bonds*” [75]. As the Rose equation needs to be chosen for a given structure it guarantees a perfect equation for that structure, but will almost certainly fail for other structures. This ties the resulting potential to a chosen reference structure.

1.3.4. REFERENCE-FREE MEAM

TO regain variational freedom a new formalism has been introduced by Timonova and Thijsse [75, 76, 86]. In the new formalism the pair interactions are described by an explicit function and is no longer bound to the Rose equation of state. This means that the parameters of a potential may be fitted to any structure. This new formalism is therefore dubbed Reference-Free MEAM (RF-MEAM) as there is no dependence on a reference structure. The analytical formulation of Duff et al. [75] is used in this study, it is an addition to the formalism in Eqs. (1.41)-(1.44). The changes are made to Eq. (1.43), where the foreshadowing (0) is replaced with (l) where $l \in \{0, 1, 2, 3\}$. The other equations remain unchanged. For the partial electron density we write

$$\left(\rho_i^{(l)}\right)^2 = \sum_{j,k \neq i}^N f_{\alpha_j}^{(l)}(r_{ij}) f_{\alpha_k}^{(l)}(r_{ik}) P^{(l)}(\cos\theta_{jik}). \quad (1.52)$$

Where $P^{(l)}$ are Legendre polynomials, i.e., $P^{(0)}(x) = 1$, $P^{(1)}(x) = x$, $P^{(2)}(x) = (3x^2 - 1)/2$, and $P^{(3)}(x) = (5x^3 - 3x)/2$. The electron density at site i , ρ_i is given by

$$\rho_i = \frac{2\rho_i^{(0)}}{1 + e^{-T_i}}. \quad (1.53)$$

Where T_i is found from the partial electron densities

$$T_i = \sum_{l=1}^3 t_i^{(l)} \left(\frac{\rho_i^{(l)}}{\rho_i^{(0)}} \right)^2. \quad (1.54)$$

Here the t_i 's are additional parameters that can be optimised when fitting a potential. Setting all t_i 's equal to zero effectively returns an EAM potential.

In the current study the (RF-)MEAM potential will see a lot of use, in Chapter 3 a RF-MEAM potential for Fe is fitted, and in Chapters 4 and 5 several MEAM potentials are used to simulate nucleation of carbide clusters.

1.3.5. MACHINE LEARNING OR AI POTENTIALS

ARTIFICIAL intelligence (AI) or machine learning methods have also penetrated computational materials science. Potentials can also be constructed by various machine

learning methods, we cite two types of Machine Learning Potential (MLP): the Gaussian Approximation Potential (GAP) [87, 88], and the Neural Network Potential (NNP) [89, 90].

Dragoni *et al.* [88] have been able to find a potential capable of reproducing Density Functional Theory (DFT) results in bcc structured ferromagnetic iron. This potential is successful in reproducing defect formation energies, as well as the material properties, i.e., elastic moduli, lattice parameter, and bulk modulus⁹. The GAP methodology claims to fit to the fit-data using only linear algebra instead of “iterative nonlinear optimization of a highly multimodal function as in the case of neural networks”. So the GAP parameters should retain their physical meaning, and be re-traceable to their original starting point.

Neural Network Potentials, e.g. Feng *et al.* [90], using a variant of neural network learning methods, can also be used to fit a potential function. Clearly, as Feng *et al.* demonstrate, NNP’s can reproduce material properties with good accuracy.

The use of MLP’s to fit potential functions holds two big promises:

- The ability to reproduce DFT calculations, and produce results with DFT-like accuracy for much larger supercells than would be computationally viable in DFT.
- Fast adaptation to various systems, e.g., containing not only iron atoms, but also containing alloying elements.

In short, MLP’s could provide the most powerful tool in the interatomic potential toolbox yet. This is particularly interesting for complex compositions containing four or more elements, for which not many (RF)-(M)EAM potentials currently exist.

It is important to note that several drawbacks to using MLP’s also exist:

- Training a MLP requires a vast dataset, this cannot be satisfied with just experimental data.
- The lack of enough data points means that MLP’s are fit to DFT data, DFT calculations return different values than experiments⁹, so a choice must be made.
- Particularly for NNP’s it is difficult to comprehend any of the choices made by the training algorithm, as these choices are made by the algorithm itself. This results in a ‘black-box’ potential that produces the right result, but it is not understood why, or the potential functions lack physical meaning.
- Currently simulations using MLP’s are slow when simulating systems containing 10⁶ atoms or more. This point will, as time progresses, most likely be addressed by better optimisation and more powerful hardware.

In order to replace ‘classical’ potentials, for lack of a better term, these issues must be addressed in some form. Which is why (RF)-(M)EAM potentials remain useful as long as these drawbacks are not taken care of.

⁹The material properties and defect energies as found in DFT calculations, which may differ significantly from experimental values.

1.4. NUCLEATION OF PRECIPITATES

IN Section 1.2 the CNGT was introduced. Using the classical theory there are three stages in the precipitate development process, as mentioned; nucleation, growth, and coarsening. These stages are distinguished by the average precipitate size, the number density of precipitates, and the availability of precipitate forming elements that remain in solid-solution. The classical model provides a good macroscopic description of precipitate development. However, the atomistic behaviour is not captured.

Generally models based on CNGT implicitly assume that precipitates have the same shape and composition for all sizes. In most models a spherical shape is assumed. This works well for the model, however experimental observations show otherwise, e.g., [91–97]. For carbides, nitrides, and carbonitrides in ferrite, the initial shape of precipitates is plate-like or disk-like as displayed in Figure 1.3. The early cluster is in the form of a platelet lying mainly in a single [100] plane, whereas larger precipitates have a more spheroidal shape, close to the assumption in most CNGT models.

Evidently precipitation processes can follow more complex paths. These complex

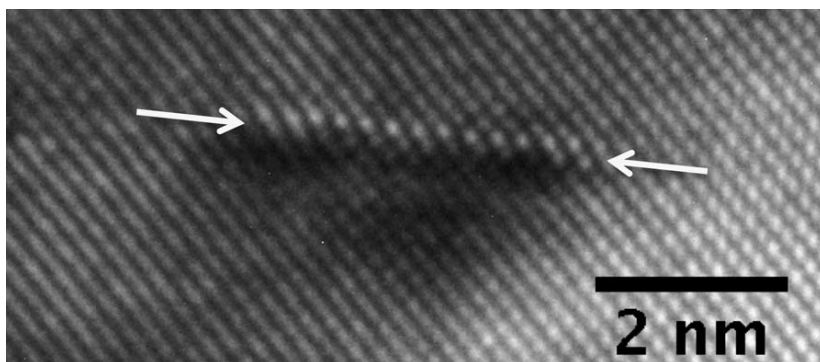


Figure 1.3: A high-resolution transmission electron microscopy image of a 'typical' Nb(C,N) nano-precipitate. The nano-precipitate has a flat shape consisting of one or two atomic layers. Reproduced from Breen *et al.* [92].

paths are not incorporated in CNGT, yet the CNGT models provide good general solutions. A more in-depth view is necessary for the microscopic picture, here we will follow the general outline used by Porter, Easterling, and Sherif [98]. For the nucleation of carbides, nitrides, and carbonitrides in ferrite the formation of a Guinier-Preston zone and the theory of spinodal decomposition are of particular interest¹⁰.

1.4.1. GUINIER-PRESTON ZONE

GUINIER and Preston [99–104] found, independent from each other¹¹, a change in the matrix structure of aluminium alloys before the formation of CuAl₂ precipitates.

In an Al-Cu alloy containing less than 2% Cu atoms all Cu atoms will be in solid solution at a temperature of about 525°C, as shown in the Al-Cu phase diagram in Figure 1.4. When the alloy is quenched to room temperature the solid solution is supersaturated with

¹⁰See Chapter 4.

¹¹An interesting article on G.D. Preston was written by Olivier Hardouin Duparc [105].

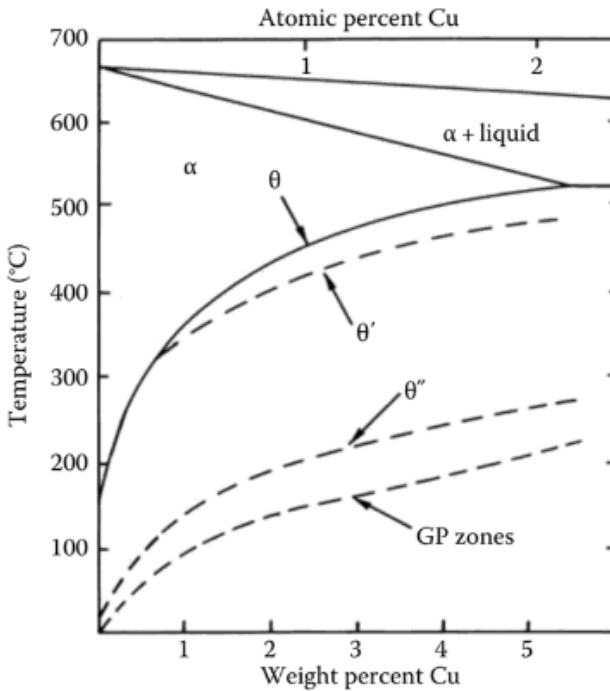


Figure 1.4: Phase diagram of the Al-Cu binary with the GP zone and the solvus lines for the θ , θ' , and θ'' precipitates. After [98, 106].

Cu atoms. In the supersaturated solid solution there is an energy gain associated with forming the CuAl_2 equilibrium phase (θ phase). The θ phase will not be formed at all after quenching, but when the alloy is left (aged) at room temperature (or slightly higher depending on the Cu content) a Cu-rich zone appears. This Cu-rich zone is known as the Guinier-Preston (GP) zone. When the aging process continues eventually θ'' will form, which is a meta-stable precursor to the θ phase.

The GP zones are fully coherent with the Al matrix, and therefore possesses a low interface energy. Furthermore they induce a low strain energy due to their disk-shape. Despite the fact that the energy gain for forming GP zones is lower than for forming the θ phase, the activation energy barrier for nucleation of the GP zones is lower. At room temperature the thermal energy is limited which is why only low activation energy can be overcome, and this determines which process occurs. In this case only the GP zones form.

Similar GP zones have been found in Al-Zn and Al-Ag alloys. The Zn and Ag-rich zones are also fully coherent with the Al matrix, and cause a low strain energy.

A special role is played by vacancies. The equilibrium vacancy concentration goes

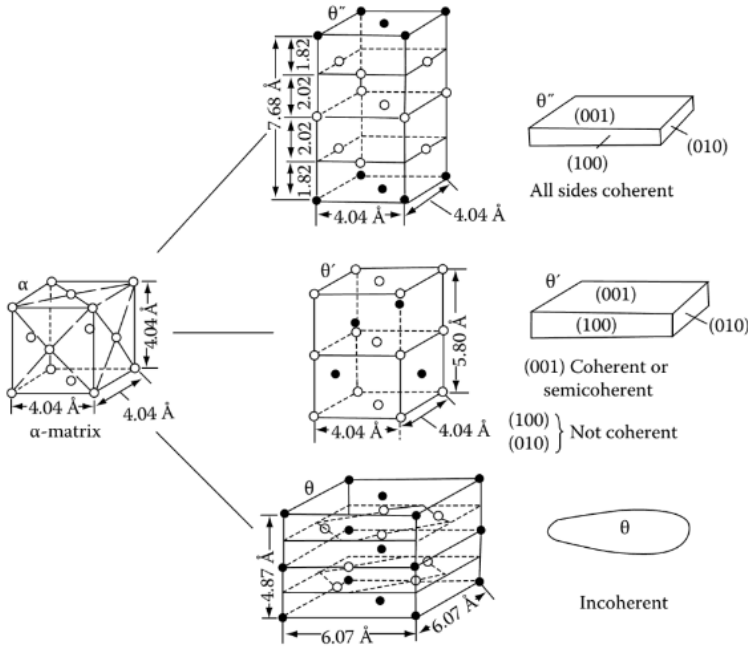


Figure 1.5: Comparison of the fcc Al lattice with the various precipitate phases: θ'' , θ' , and θ . After [98].

up with temperature [98],

$$X_{\text{vacancy}}^{\text{eq}} = \exp\left(-\frac{\Delta G_{\text{vacancy}}}{RT}\right). \quad (1.55)$$

Where $X_{\text{vacancy}}^{\text{eq}}$ is the mole fraction of vacancies, $\Delta G_{\text{vacancy}}$ is the free energy associated with the formation of one mole of vacancies, R the gas constant, and T the absolute temperature.

The high temperature equilibrium vacancy concentration is also high, and this high equilibrium vacancy concentration is retained at low temperatures when the material is quenched. The retained vacancy concentration is much higher than the low temperature equilibrium vacancy concentration. Over time vacancies evolve towards their much lower equilibrium concentration, by forming vacancy clusters which collapse into dislocation loops or by allowing dislocation climb [107, 108]¹². Vacancies also increase the diffusivity of atoms within the matrix, which speeds up nucleation and growth of precipitates. This is key in explaining the rapid formation of GP zones. Moreover, Girifalco and Herman [109], and Petrik *et al.* [110] found that the GP zones act like ‘vacancy pumps’. Girifalco and Herman’s model assumes that the binding energy between vacancies and Cu atoms is high enough that vacancies predominantly exist as vacancy-Cu complexes. The binding energy between a vacancy and a Cu atom in a GP zone is very small. The

¹²The θ' formation in the Al-Cu alloy occurs during annealing at ≈ 400 K, and involves absorption of large numbers of vacancies.

interaction between a vacancy and a GP zone is small, and between a GP zone and a vacancy-Cu complex is small. The diffusion for vacancy-Cu complexes is much larger than for free Cu atoms.

The vacancy pump cycle then works as follows: The GP zone attracts vacancy-Cu complexes. The vacancy-Cu complexes are disbanded when they reach the GP zone. Then the local accumulation of vacancies near the GP zone creates a driving force pushing the vacancies back into the matrix, where they form new vacancy-Cu complexes.

1.4.2. SPINODAL DECOMPOSITION

SOME transformations do not have an energy barrier for nucleation. One particular example is spinodal decomposition. For alloys where spinodal decomposition plays a role, a spontaneous separation of two phases occurs, the smallest composition fluctuation in the alloy will set off this separation. An in-depth theoretical description is provided in [98] which we will not reproduce here.

The dynamics of such a decomposition process can be modelled using the Cahn-Hilliard equation,

$$\frac{\partial c}{\partial t} = M \left[\left(\frac{\partial^2 f}{\partial c^2} \right)_{c=c_0} \nabla^2 c - 2\kappa \nabla^4 c \right]. \quad (1.56)$$

Where c is the fraction of a phase, $c \in [0, 1]$ gives domains of the two phases. M is the mobility, κ is the gradient-energy coefficient, and f is the Helmholtz free energy per unit volume [111].

The spinodal decomposition and GP zone formation are different in nature, in that in spinodal decomposition there is no barrier for nucleation whereas for the GP zones there is a lowered barrier for nucleation [98]. However, both show that nucleation of a new phase does not have to follow the assumptions set by the CNGT. The formation of the carbide, nitride, or carbonitride platelets in ferrite, as found in experiments [91–97], seems to be a violation of the assumption made in the CNGT that these precipitates immediately form with the NaCl-structure forming without an intermediate phase. In fact Danoix *et al.* [95] claim that niobium nitrides form GP zones or similar structures in steel, which is not a part of CNGT.

1.4.3. NUCLEATION OF CARBIDES

UNDERSTANDING the formation of carbides, nitrides and carbonitrides would ideally require direct experimental observations of steps in the nucleation process of the precipitates. The formation of commonly used carbides, i.e., NbC, TiC, and VC, occurs at temperatures higher than 1000 K. Transmission electron microscopy (TEM), as used in [91–97] cannot be used at these temperatures. The smallest observed particles in Breen *et al.* [92] contain roughly 100 atoms, so many atoms have already formed such a particle, similarly for Wang *et al.* [94] the smallest particles have a diameter of roughly 1.5 nm. The formation of smaller particles or clusters is not observed experimentally. Interatomic models and simulations as described in Section 1.3 can be useful to reproduce various atomic structures resembling precipitates at high temperatures and at much smaller scales, to study the properties and stability of such atomic structures.

Three main questions arise:

- How do proto-clusters form from dissolved single Nb, Ti, C, and N atoms?
- What does the atomic structure of newly formed proto-clusters look like?
- How do the clusters develop a NaCl-structure?

Sawada *et al.* [112, 113] have performed first principles calculations studying the interface of Nb and Ti-carbides with ferrite. They found that the interface between the precipitate and the ferrite matrix maintains coherency up to a certain interface size, which is dependent on the thickness of the precipitate. Hereto a NaCl-structure carbide was used, which was then relaxed in a ferrite matrix. It is found that NaCl structured carbide platelets can have a coherent interface with a diameter of 1.5 nm for NbC and 2.3 nm for TiC. These sizes agree with the experimental observations by Wang *et al.* [94] for TiC, and Danoix *et al.* [95] for Nb(C_xN_y) precipitates.

From experiments and calculations it follows that the nucleation of carbides in ferrite¹³ hinges on the coherency of the initial nucleus' interface with the matrix and the induced strain energy within the system. Which is a good reason to assume that a GP zone, or something similar to a GP zone forms before the carbides form as they cause less strain as shown in Chapter 5.

1.5. SUMMARY

IN this chapter a brief overview of the underlying models and ideas for the evolution of precipitates in iron has been presented.

Firstly the models concerning classical precipitate nucleation and growth have been discussed. Clearly, there are several paths to follow when modelling the development of precipitates. The general pattern is that some driving force needs to be found, this may be a Gibbs energy as in Eq. (1.1) or an attachment/detachment rate (which is a direct result of a driving force) as in Eqs. (1.9) and (1.10). The models presented here are all intended to describe the macroscopic nucleation behaviour where several generalisations are made, particularly concerning the shape or structure of the developing precipitates.

In the second part interatomic models were introduced, with a particular focus on analytical models. These models are widely used in computational materials science, and can predict material properties with great accuracy.

In the last part the nucleation of precipitates, and carbides in ferrite, has been discussed in more detail. Additionally GP zone formation and spinodal decomposition have been introduced as formation mechanisms alternative to classical nucleation and growth. It is important to see the contrast between experimental results for carbide precipitation in ferrite on the atomic level or microscale and the numerical models which describe the total precipitate population at the macroscale. TEM observations from several groups have shown in the last decades that the assumptions, made in CNGT, especially on the composition of the (initial) nucleus, are not valid.

¹³Or more generally, for most common precipitate types as suggested in for example [98, 108].

REFERENCES

- [1] T. Gladman. *The physical metallurgy of microalloyed steels*. CRC Press, second edition, 2001.
- [2] A. Deschamps and Y. Bréchet. Influence of predeformation and ageing of an Al-Zn-Mg alloy - II. modeling of precipitation kinetics and yield stress. *Acta materialia*, 47(1):293–305, 1999.
- [3] A. J. Ardell. Precipitation hardening. *Metallurgical transactions A*, 16A:2131–2165, December 1985.
- [4] A. Deschamps, F. Livet, and Y. Bréchet. Influence of predeformation on ageing in an Al-Zn-Mg alloy - I. microstructure evolution and mechanical properties. *Acta materialia*, 47(1):281–292, December 1999.
- [5] G. E. Dieter Jr. *Mechanical metallurgy*. McGraw-Hill book company, second edition, 1988.
- [6] S. Nandy, K. K. Ray, and D. Das. Process model to predict yield strength of AA6063 alloy. *Materials science and engineering: A*, 644:413–424, 2015.
- [7] S. Esmaeili, D. J. Lloyd, and W. J. Poole. A yield strength model for the Al-Mg-Si-Cu alloy AA6111. *Acta materialia*, 51:2243–2257, 2003.
- [8] S. Esmaeili and D. J. Lloyd. Modeling of precipitation hardening in pre-aged AlMgSi(Cu) alloys. *Acta materialia*, 53:5257–5271, 2005.
- [9] H. S. Zurob, C. R. Hutchinson, Y. Brechet, and G. Purdy. Modeling recrystallization of microalloyed austenite: effect of coupling recovery, precipitation and recrystallization. *Acta materialia*, 50:3075–3092, 2002.
- [10] B. Dutta, E. J. Palmiere, and C. M. Sellars. Modelling the kinetics of strain induced precipitation in Nb microalloyed steels. *Acta materialia*, 49:785–794, 2001.
- [11] R. Kampmann and R. Wagner. Kinetics of precipitation in metastable binary alloys - Theory and application to Cu-1.9 at% Ti and Ni 14 at% Al. In P. Haasen, V. Gerold, R. Wagner, and M. F. Ashby, editors, *Decomposition of alloys: the early stages: proceedings of the 2nd Acta-Scripta Metallurgica conference*, number 2 in 2. Acta metallurgica, Pergamon press, 1984.
- [12] D. den Ouden, L. Zhao, C. Vuik, J. Sietsma, and F. J. Vermolen. Modelling precipitate nucleation and growth with multiple precipitate species under isothermal conditions: Formulation and analysis. *Computational materials science*, 79:933–943, 2013.
- [13] P. Maugis and M. Gouné. Kinetics of vanadium carbonitride precipitation in steel: a computer model. *Acta materialia*, 53:3359–3367, 2005.

- [14] M. Perez, M. Dumont, and D. Acevedo-Reyes. Implementation of classical nucleation and growth theories for precipitation. *Acta materialia*, 56:2119–2132, March 2008.
- [15] L. M. L. Cheng. *Study of the kinetics of precipitation, dissolution and coarsening of aluminum nitride in low carbon steels*. phdthesis, University of British Columbia, April 1999.
- [16] R. Gómez-Ramírez and G. M. Pound. Nucleation of a second solid phase along dislocations. *Metallurgical transactions*, 4(6):1563–1570, June 1973.
- [17] E. Clouet. Modeling of nucleation processes. *ASM handbook*, 22A:203–219, 2009.
- [18] E. Clouet, M. Nastar, and C. Sigli. Nucleation of Al₃Zr and Al₃Sc in aluminum alloys: from kinetic Monte Carlo simulations to classical theory. *Physical review B*, 69:064109, 2004.
- [19] F. Soisson and G. Martin. Monte Carlo simulations of the decomposition of metastable solid solutions: Transient and steady-state nucleation kinetics. *Physical review B*, 62(1):203–214, July 2000.
- [20] M. Volmer and A. Weber. Keimbildung in übersättigten Gebilden. *Zeitschrift für Physikalische Chemie*, 119:277–301, 1926.
- [21] R. Becker and W. Döring. Kinetische Behandlung der Keimbildung in übersättigten Dämpfen. *Annalen der Physik*, 416(8):719, 1935.
- [22] Ya. B. Zeldovich. On the theory of new phase formation: cavitation. *Acta physicochim USSR*, 18:1–22, 1943.
- [23] L. Farkas. Keimbildungsgeschwindigkeit in übersättigten Dämpfen. *Zeitschrift für Physikalische Chemie*, 125(1):236–242, 1927.
- [24] A. C. Pan and D. Chandler. Dynamics of nucleation in the Ising model. *The journal of physical chemistry B*, 108(51):19681–19686, 2004.
- [25] H. Vehkamäki, A. Määttänen, A. Lauri, I. Napari, and M. Kulmala. Technical note: The heterogeneous Zeldovich factor. *Atmospheric chemistry and physics*, 7:309–313, 2007.
- [26] K. C. Russell. Nucleation in solids: The induction and steady state effects. *Advances in Colloid and Interface Science*, 13(3-4):205–318, September 1980.
- [27] V. A. Shneidman and M. C. Weinberg. Induction time in transient nucleation theory. *The journal of chemical physics*, 97(5):3621, 1992.
- [28] R. J. Slooter, M. H. F. Sluiter, W. G. T. Kranendonk, and C. Bos. Approximation and characteristic times in precipitation modelling. *ISIJ international*, 61(5), 2021.

- [29] N. Korepanova, L. Gu, M. Dima, and H. Xu. Cluster dynamics modeling of niobium and titanium carbide precipitates in α -Fe and γ -Fe. *Chinese Physics B*, 31:026103, 2022.
- [30] C. Zener. Theory of growth of spherical precipitates from solid solution. *Journal of applied physics*, 20:950–953, October 1949.
- [31] S. M. Vonk. Precipitates on dislocations: Mathematical modelling of nucleating and growing precipitates on dislocations. mathesis, TU Delft, September 2016.
- [32] I. M. Lifshitz and V. V. Slyozov. The kinetics of precipitation from supersaturated solid solutions. *Journal of physical chemistry solids*, 19(1-2):35–50, 1961.
- [33] C. Wagner. Theorie der Alterung von Niederschlägen durch Umlösen. *Zeitschrift für elektrochemie*, 65:581–594, 1961.
- [34] W. Ostwald. Studien über die Bildung und Umwandlung fester Körper. 1. Abhandlung: Übersättigung und Überkaltung. *Zeitschrift für Physikalische Chemie*, 22U(1):289–330, February 1897.
- [35] A. Baldan. Review progress in Ostwald ripening theories and their application to nickel-base superalloys. Part I: Ostwald ripening theories. *Journal of materials science*, 37:2171–2202, 2002.
- [36] B. Niethammer. *Analysis and stochastics of growth processes and interface models*, chapter 10. Effective theories for Ostwald ripening, pages 223–242. Oxford University press, 2008.
- [37] A. J. Ardell. The effect of volume fraction on particle coarsening: theoretical considerations. *Acta Metallurgica*, 20(1):61–71, January 1972.
- [38] J. J. Hoyt. On the coarsening of precipitation located on grain boundaries and dislocations. *Acta metallurgica et materialia*, 39(9):2091–2098, September 1991.
- [39] H. Kreye. Influence of dislocations on the growth of particles. *Zeitschrift für Metallkunde*, 61:108, 1970.
- [40] W. Kranendonk. Modelling strain induced precipitation: The Zurob model. Internal report, Corus, June 2005.
- [41] R. Kampmann and R. Wagner. *Materials science and technology - A comprehensive treatment*, volume 5, chapter 5. Homogeneous second phase precipitation, page 213. Wiley - VCH, Weinheim, Germany, 1991.
- [42] J. D. Robson. Modelling the overlap of nucleation, growth and coarsening during precipitation. *Acta materialia*, 52(15):4669–4676, 2004.
- [43] D. den Ouden. *Mathematical modelling of nucleating and growing precipitates*. phdthesis, TU Delft, 2015.

- [44] J. E. Jones. On the determination of molecular fields - I. From the equation of state of a gas. In *Proceedings of the Royal Society of London. Series A, containing papers of a mathematical and physical character*, volume 106, pages 463–477, 1924.
- [45] J. E. Jones. On the determination of molecular fields - II. From the variation of the viscosity of a gas with temperature. In *Proceedings of the Royal Society of London. Series A, containing papers of a mathematical and physical character.*, volume 106, pages 441–462, 1924.
- [46] J. E. Lennard-Jones. Cohesion. In *Proceedings of the Physical Society*, volume 43, page 461. IOP Publishing Ltd, 1931.
- [47] P. M. Morse and E. C. G. Stueckelberg. Diatomic molecules according to the wave mechanics I: Electronic levels of the hydrogen molecular ion. *Physical review*, 33:932–947, 1929.
- [48] P. M. Morse. Diatomic molecules according to the wave mechanics II: Vibrational levels. *Physical review*, 34:57–64, 1929.
- [49] L. Peliti. *Statistical mechanics in a nutshell*. Princeton university press, 2011.
- [50] T. L. Hill. *An introduction to statistical thermodynamics*. Dover publications, Inc., second edition, 1986.
- [51] N. W. Ashcroft and N. D. Mermin. *Solid state physics*. Brooks/Cole, 1976.
- [52] J. M. Thijssen. *Computational physics*. Cambridge university press, second edition, 2007.
- [53] R. A. Johnson. Interstitials and vacancies in α -iron. *Physical review*, 134(5A):A1329–A1336, 1964.
- [54] J. B. Gibson, A. N. Goland, M. Milgram, and G. H. Vineyard. Dynamics of radiation damage. *Physical review*, 120(4):1229–1253, 1960.
- [55] R. A. Johnson and E. Brown. Point defects in copper. *Physical review*, 127(2):446–454, 1962.
- [56] A. Seeger, E. Mann, and R. v. Jan. Zwischengitteratome in kubisch-flächenzentrierten kristallen, insbesondere in kupper. *Journal of physical chemistry in solids*, 23:639–658, 1962. [German].
- [57] H. B. Huntington. Mobility of interstitial atoms in a face-centered metal. *Physical review*, 91(5):1092–1098, 1953.
- [58] L. Tewordt. Distortion of the lattice around an interstitial, a crowdion, and a vacancy in copper. *Physical review*, 109(1):61–68, 1958.
- [59] M. S. Daw and M. I. Baskes. Semiempirical, quantum mechanical calculation of hydrogen embrittlement in metals. *Physical review letters*, 50(17):1285–1288, April 1983.

- [60] M. S. Daw and M. I. Baskes. Embedded-atom method: Derivation and application to impurities, surfaces, and other defects in metals. *Physical review B*, 29(12):6443–6453, June 1984.
- [61] G. J. Ackland, G. Tichy, V. Vitek, and M. W. Finnis. Simple N -body potentials for the noble metals and nickel. *Philosophical magazine A*, 56(6):735–756, 1987.
- [62] M. W. Finnis and J. E. Sinclair. A simple empirical N -body potential for transition metals. *Philosophical magazine A*, 50(1):45–55, 1984.
- [63] S. M. Foiles, M. I. Baskes, and M. S. Daw. Embedded-atom-method functions for the fcc metals Cu, Ag, Au, Ni, Pd, Pt, and their alloys. *Physical review B*, 33(12):7983–7991, June 1986.
- [64] G. J. Ackland and R. Thetford. An improved N -body semi-empirical model for body-centered cubic transition metals. *Philosophical magazine A*, 56(1):15–30, 1987.
- [65] S. M. Foiles and M. S. Daw. Application of the embedded atom method to Ni_3Al . *Journal of materials research*, 2(1):5–15, 1987.
- [66] F. Ercolessi, E. Tosatti, and M. Parrinello. Au (100) surface reconstruction. *Physical review letters*, 57(6):719–722, 1986.
- [67] F. Ercolessi, E. Tosatti, and M. Parrinello. Au(100) reconstruction in the glue model. *Surface science*, 177(2):314–328, 1986.
- [68] F. Ercolessi, M. Parrinello, and E. Tosatti. Simulation of gold in the glue model. *Philosophical magazine A*, 58(1):213–226, 1988.
- [69] M. S. Daw, S. M. Foiles, and M. I. Baskes. The embedded-atom method: a review of theory and applications. *Materials science reports*, 9(7-8):251–310, 1993.
- [70] M. I. Mendeleev, S. Han, D. J. Srolovitz, G. J. Ackland, D. Y. Sun, and M. Asta. Development of new interatomic potentials appropriate for crystalline and liquid iron. *Philosophical magazine*, 83(35):3977–3994, 2003.
- [71] G. J. Ackland, M. I. Mendeleev, D. J. Srolovitz, S. Han, and A. V. Barashev. Development of an interatomic potential for phosphorus impurities in α -iron. *Journal of physics: Condensed matter*, 16:S2629–S2642, 2004.
- [72] M. I. Mendeleev, S. Han, W.-J. Son, G. J. Ackland, and D. J. Srolovitz. Simulation of the interaction between Fe impurities and point defects in V. *Physical review B*, 76:214105, 2007.
- [73] C. S. Becquart, J. M. Raulot, G. Bencteux, C. Domain, M. Perez, S. Garruchet, and H. Nguyen. Atomistic modeling of an Fe system with a small concentration of C. *Computational materials science*, 40:119–129, 2007.
- [74] D. J. Hepburn and G. J. Ackland. Metallic-covalent interatomic potential for carbon in iron. *Physical review B*, 78:165115, 2008.

- [75] A. I. Duff, M. W. Finnis, P. Maugis, B. J. Thijsse, and M. H. F. Sluiter. MEAMfit: A reference-free embedded atom method (RF-MEAM) energy and force-fitting code. *Computer physics communications*, 196:439–445, 2015.
- [76] M. Timonova and B. J. Thijsse. Optimizing the MEAM potential for silicon. *Modelling and simulation in materials science and engineering*, 19:015003, 2011.
- [77] A. E. Carlsson. Beyond pair potentials in elemental transition metals and semiconductors. *Solid state physics*, 43:1–91, 1990.
- [78] M. I. Baskes. Application of the embedded-atom method to covalent materials: a semiempirical potential for silicon. *Physical review letters*, 59(23):2666–2669, December 1987.
- [79] M. I. Baskes, J. S. Nelson, and A. F. Wright. Semiempirical modified embedded-atom potentials for silicon and germanium. *Physical review B*, 40(9):6085–6100, September 1989.
- [80] M. I. Baskes. Modified embedded-atom potentials for cubic materials and impurities. *Physical review B*, 46(5):2727–2742, August 1992.
- [81] B.-J. Lee and M. I. Baskes. Second nearest-neighbor modified embedded-atom-method potential. *Physical review B*, 62(13):8564–8567, October 2000.
- [82] B.-J. Lee, M. I. Baskes, H. Kim, and Y. K. Cho. Second nearest-neighbour modified embedded atom method potentials for bcc transition metals. *Physical review B*, 64:184102, 2001.
- [83] H.-K. Kim, W.-S. Jung, and B.-J. Lee. Modified embedded-atom method interatomic potential for the Fe-Ti-C and Fe-Ti-N ternary systems. *Acta materialia*, 57:3140–3147, 2009.
- [84] H.-K. Kim, W.-S. Jung, and B.-J. Lee. Modified embedded-atom method interatomic potentials for the Nb-C, Nb-N, Fe-Nb-C, and Fe-Nb-N systems. *Journal for material research*, 25(7):1288–1297, 2010.
- [85] J. H. Rose, J. R. Smith, F. Guinea, and J. Ferrante. Universal features of the equation of state of metals. *Physical review B*, 29(6):2963, 1984.
- [86] I. Lazic and B. J. Thijsse. An improved molecular dynamics potential for the Al-O system. *Computational materials science*, 53:483–492, 2012.
- [87] A. P. Bartók, M. C. Payne, R. Kondor, and G. Csányi. Gaussian Approximation Potentials: The accuracy of quantum mechanics, without the electrons. *Physical Review Letters*, 104:136403, 2010.
- [88] D. Dragoni, T. D. Daff, G. Csányi, and N. Marzari. Achieving DFT accuracy with a machine-learning interatomic potential: Thermomechanics and defects in bcc ferromagnetic iron. *Physical Review Materials*, 2:013808, 2018.

- [89] H. Mori and T. Ozaki. Neural network atomic potential to investigate the dislocation dynamics in bcc iron. *Physical Review Materials*, 4:040601(R), 2020.
- [90] F.-S. Feng, J.-P. Du, S. Shinzato, H. Mori, P. Yu, K. Matsubara, N. Ishikawa, and S. Ogata. General-purpose neural network interatomic potential for the α -iron and hydrogen binary system: Toward atomic-scale understanding of hydrogen embrittlement. *Physical Review Materials*, 5:113606, 2021.
- [91] E. Courtois, T. Epicier, and C. Scott. Characterisation of niobium carbide and carbonitride evolution within ferrite: contribution of transmission electron microscopy and advanced associated techniques. *Materials Science Forum*, 500-501:669–676, 2005.
- [92] A. J. Breen, K. Y. Xie, M. P. Moody, B. Gault, H.-W. Yen, C. C. Wong, J. M. Cairney, and S. P. Ringer. Resolving the morphology of niobium carbonitride nano-precipitates in steel using atom probe tomography. *Microscopy and microanalysis*, 20:1100–1110, 2014.
- [93] J. Takahashi, K. Kawakami, and Y. Kobayashi. Origin of hydrogen trapping site in vanadium carbide precipitation strengthening steel. *Acta materialia*, 153:193–204, 2018.
- [94] J. Wang, M. Weyland, I. Bikmukhametov, M. K. Miller, P. D. Hodgson, and I. Timokhina. Transformation from cluster to nano-precipitate in microalloyed ferritic steel. *Scripta materialia*, 160:53–57, 2019.
- [95] F. Danoix, T. Epicier, F. Vurpillot, and D. Blavette. Atomic-scale imaging and analysis of single layer GP zones in a model steel. *Journal of material science*, 47:1567–1571, 2012.
- [96] T. Furuhashi, Y. Zhang, M. Sato, G. Miyamoto, M. Enoki, H. Ohtani, T. Uesugi, and H. Numakura. Sublattice alloy design of high-strength steels: Application of clustering and nanoscale precipitation of interstitial and substitutional solutes. *Scripta Materialia*, 223:115063, 2023.
- [97] S. Taniguchi, G. Shigesato, and M. Sugiyama. Atomic resolution scanning transmission electron microscopy of TiC precipitates in low carbon ferritic steels. *ISIJ International*, 62(5):984–991, 2022.
- [98] D. A. Porter, K. E. Easterling, and M. Y. Sherif. *Phase transformations in metals and alloys*. CRC Press, Taylor and Francis group, third edition, 2009.
- [99] G. D. Preston. The diffraction of X-rays by an age-hardening alloy of aluminium and copper. The structure of an intermediate phase. *The London, Edinburgh, and Dublin Philosophical Magazine and Journal of Science*, 26:855–871, 1938.
- [100] G. D. Preston. The diffraction of X-rays by age-hardening aluminium copper alloys. *Proceedings of the Royal Society*, 167:526–538, 1938.

- [101] G. D. Preston. Structure of age-hardened aluminium-copper alloys. *Nature*, 142:570, 1938.
- [102] A. Guinier. Un nouveau type de diagrammes de rayons X. *Comptes Rendus Hebdomadaires Des Séances De l'Académie Sciences*, 206:1641–1643, 1938.
- [103] A. Guinier. Structure of age-hardened aluminium-copper alloys. *Nature*, 142:569–570, 1938.
- [104] J. Calvet, P. Jacquet, and A. Guinier. Sur le durcissement par vieillissement d'un alliage aluminium-cuivre. *Comptes Rendus Hebdomadaires Séances l'Académie Sciences*, 206:1972–1974, 1938.
- [105] O. B. M. Hardouin Duparc. The Preston of the Guinier-Preston zones. *Metallurgical and Materials Transactions B*, 41A:1873–1882, 2010.
- [106] K. C. Russell and H. I. Aaronson, editors. *Precipitation processes in solids*. The Metallurgical Society of AMIE, 1978.
- [107] W. Cai and W. D. Nix. *Imperfections in crystalline solids*. Cambridge University Press, 2016.
- [108] D. Hull and J. D. Bacon. *Introduction to dislocations*. Butterworth-Heinemann, fifth edition, 2011.
- [109] L. A. Girifalco and H. Herman. A model for the growth of Guinier-Preston zones—the vacancy pump. *Acta Metallurgica*, 13(6):583–590, June 1965.
- [110] M. V. Petrik, Y. N. Gornostyrev, and P. A. Korzhavyi. Point defect interactions with Guinier-Preston zones in Al-Cu based alloys: Vacancy mediated GPZ to θ' -phase transformation. *Scripta Materialia*, 165:123–127, 2019.
- [111] K. B. Rundman and J. E. Hilliard. Early stages of spinodal decomposition in an aluminum-zinc alloy. *Acta Metallurgica*, 15:1025–1033, 1967.
- [112] H. Sawada, S. Taniguchi, K. Kawakami, and T. Ozaki. First-principles study of interface structure and energy of Fe/NbC. *Modelling and simulation in materials science and engineering*, 21(4):045012, 2013.
- [113] H. Sawada, S. Taniguchi, K. Kawakami, and T. Ozaki. Transition of the interface between iron and carbide precipitate from coherent to semi-coherent. *Metals*, 7:277–289, 2017.

2

APPROXIMATION AND CHARACTERISTIC TIMES IN PRECIPITATION MODELLING

*Nichts ist leichter, als so zu schreiben, dass kein Mensch es versteht;
wie hingegen nichts schwerer, als bedeutende Gedanken so auszudrücken, dass jeder sie
verstehen muss.*

Arthur Schopenhauer

You can't know too much, but you can say too much.

Calvin Coolidge

A new approximation to the equations describing Classical Nucleation and Growth Theories, is proposed providing quick, and intuitive insight. It gives a prediction of the mean precipitate radius and number density development under quasi-isothermal conditions. Current “mean-radius”, and “multi-class” approaches to modelling classical nucleation and growth theory for precipitation, require considerable computation times. An approximate analytical is proposed. Its results are compared to numerical simulations for quasi-isothermal precipitation. From the approximation a start and end time for the nucleation stage is predicted, as well as a time at which growth occurs and when the coarsening stage starts. Ultimately, these times, outline the numerical solution to the precipitation trajectory, providing key insight before performing numerical simulations. This insight can be

Parts of this chapter have been published in *ISIJ international* **61**(5), pp. 1698-1707, (2021) [1].

used to more efficiently simulate precipitate development, as time scales at which the various stages in precipitate development occur can be predicted for various precipitate types. When these time scales are known, a numerical simulation can be used for a specific goal. For instance to only simulate nucleation and growth, thus saving computational time. Moreover, for a first indication of the precipitate development for a composition under a particular heat treatment a numerical simulation is no longer necessary. This is also useful for process control as consequences of changes in treatment can be assessed on-line. Using these approximate analytical results an estimate can be made for the matrix concentration of precipitate forming elements. Additionally some dimensionless parameters are established to provide intuitive details to the precipitation trajectory.

2.1. INTRODUCTION

PRECIPITATION of a second solid phase from solid solution is commonly used to enhance metal alloy properties. An example of this enhancement is grain size control in low alloy steel [2], another example is precipitation hardening [3–9]. Many models exist to describe the precipitate development under given processing treatment, e.g. [3, 10–13]. The goal of modelling precipitation is to establish the relation between composition, processing parameters and the evolution of the precipitate sizes and precipitate volume fraction.

Different types of models exist to simulate the precipitate size and number density evolution during heat treatment. One commonly used type is based on Classical Nucleation and Growth Theory (CNGT) models [14]. CNGT precipitation models can be divided into two approaches; (i) mean-radius approach; and (ii) multi-class approach. In some cases both approaches return the same result, but in more complex systems and/or process conditions the results can differ and the more sophisticated multi-class models are required [14]. Unfortunately multi-class models require much more computational resources than mean-radius models, which matters particularly for more complex systems.

With growing computational power current research is focussed on expanding the accuracy and applicability of CNGT models, e.g., [13, 15–17], however this does not provide any detailed intuitive insight in the precipitation trajectory. This chapter seeks to provide a fast analytical approximation to quasi-isothermal precipitation for one precipitate type at one site, and from this approximation derive parameters which provide a more intuitive insight into the development of the precipitates. Though only one type of precipitate can be assessed at one nucleation site, results for multiple types and sites can be compared quickly. Allowing prediction of which precipitate will form first and where.

The approximation method is illustrated in Section 2.2.3 using an idealised system, defined by isothermal conditions, one type of precipitate, one type of nucleation site, and all available nucleation sites will to be occupied after the nucleation stage. Using this approximation several parameters are defined, which characterise the precipitate evolution, thus providing a more intuitive insight into the simulated precipitate development. As a second step, the restriction that all nucleation sites will be occupied is relaxed in Section 2.2.7, and a new approximation is derived for the case that the maximum precipitate number density is lower than the maximum available nucleation sites per unit of volume. Finally the isothermal condition is relaxed in Section 2.3 and replaced by a quasi-isothermal approximation for non-isothermal conditions. Examples for this most generalised approximation are presented. Section 2.4 gives a discussion of the validity and limitations of the methods, which are presented here.

2.2. DERIVATION FOR ISOTHERMAL PRECIPITATION

2.2.1. EVOLUTION EQUATIONS

BEFORE the approximation is made several equations are needed, here we will look into the equations used to describe a multi-class approach to get a better understanding of the classical nucleation and growth model. The approximation is made using the equations used in the multi-class approach.

NUMBER DENSITY DISTRIBUTION

VARIOUS equations are used to describe the evolution of the precipitate radii and number density. The first equation we look into is the rate of change for the precipitate number density distribution, which is derived here. We shall label the number density distribution $\varphi(R, t)$, where t is the time, and R the radius of the precipitates.

We want to prove that this function can suffice the form presented in Hulburt and Katz [18]¹:

$$\frac{\partial \varphi}{\partial t} = -\frac{\partial [\partial R / \partial t] \varphi}{\partial R} + \frac{\partial N}{\partial t} \delta(R - R^*), \quad (2.1)$$

where N is the precipitate number density, R^* is the critical radius, and $\delta(\dots)$ is the Dirac-delta function. Which may be generalised to:

$$\frac{\partial f}{\partial t} = -\frac{\partial}{\partial R} (f(R, t) \cdot v(R)) + J(R), \quad (2.2)$$

where $f(R, t)$ represents the density distribution, $v(R)$ is the growth rate of the existing precipitates, and $J(R)$ is a source term to account for nucleation². Note that the density of precipitates with radius R is not a conserved quantity as new precipitates may form due to nucleation.

Equation (2.2) is derived as follows. First we consider a situation with finite size 'bins' for density, with a bin width of ΔR . The change in density for one bin with time is then:

$$\Delta R \cdot (f(R, t + \Delta t) - f(R, t)). \quad (2.3)$$

The difference in density with time is the net flux to the bin, in combination with a possible source or drain inside the bin. Which may be written as:

$$\Delta t \cdot (f(R - \Delta R, t) \cdot v(R - \Delta R) - f(R, t) \cdot v(R) + J(R) \cdot \Delta R). \quad (2.4)$$

Now if $\partial v(R) / \partial R = 0$ there is nothing to prove, as the desired result can be written immediately. However if $v(R)$ is not constant a Taylor series can be written for $v(R - \Delta R)$ at ΔR instead:

$$\Delta t \cdot \left(f(R - \Delta R, t) \cdot v(R) - f(R, t) \cdot v(R) - f(R - \Delta R, t) \cdot \frac{\partial v(R)}{\partial R} \Delta R + J(R) \cdot \Delta R + \mathcal{O}(\Delta R^2) \right). \quad (2.5)$$

Which can be rewritten as:

$$\Delta t \cdot \left(\Delta R \left(\frac{f(R - \Delta R, t) - f(R, t)}{\Delta R} \right) \cdot v(R) - f(R - \Delta R, t) \cdot \frac{\partial v(R)}{\partial R} \Delta R + J(R) \cdot \Delta R + \mathcal{O}(\Delta R^2) \right). \quad (2.6)$$

¹Hulburt and Katz also demonstrate that solutions can be approximated by the gamma-distribution.

²Generally this term can also account for the dissolution of precipitates, but then the form of Eq. (2.1) is no longer applicable.

So when comparing Eqs. (2.3) and (2.4) we have:

$$\begin{aligned} \Delta R \cdot (f(R, t + \Delta t) - f(R, t)) &= \Delta t \cdot \left(\Delta R \left(\frac{f(R - \Delta R, t) - f(R, t)}{\Delta R} \right) \cdot v(R) \right. \\ &\quad \left. - f(R - \Delta R, t) \cdot \frac{\partial v(R)}{\partial R} \Delta R + J(R) \cdot \Delta R + \mathcal{O}(\Delta R^2) \right). \\ &\Leftrightarrow \\ \frac{(f(R, t + \Delta t) - f(R, t))}{\Delta t} &= \left(\frac{f(R - \Delta R, t) - f(R, t)}{\Delta R} \right) \cdot v(R) \\ &\quad - f(R - \Delta R, t) \cdot \frac{\partial v(R)}{\partial R} + J(R) + \mathcal{O}(\Delta R). \end{aligned} \quad (2.7)$$

Now with the definition of the derivative we take the limits $\Delta t, \Delta R \rightarrow 0$. Which gives:

$$\frac{\partial f(R, t)}{\partial t} = \frac{\partial f(R, t)}{\partial R} \cdot v(R) - f(R, t) \cdot \frac{\partial v(R)}{\partial R} + J(R) = \frac{\partial}{\partial R} (f(R, t) \cdot v(R)) + J(R). \quad (2.8)$$

Which is the expression that we wanted to find.

The exact form for $J(R)$ is not known. Hulburt and Katz [18] assume $J(R)$ to be the Dirac-delta function. Which implies that precipitates form with precisely the critical radius. More realism could be included by introducing a spread around this critical radius where the width depends on temperature to accommodate for thermal fluctuations.

Several numerical models exist, e.g., [13, 15–17], to find a solution to Eq. (2.1) and describe the precipitate development. We seek to find an analytical solution to Eq. (2.1). This proves to be an arduous task due to the non-linear nature of the right-hand-side of the equations.

The moments of this function are themselves descriptors for the precipitate development, the 0-th moment is the number density:

$$N(t) = \int_0^{\infty} \varphi(R, t) dR. \quad (2.9)$$

The 1-st moment is linked to the average radius

$$\bar{R}(t) = \frac{\int_0^{\infty} R(t) \varphi(R, t) dR}{N(t)}. \quad (2.10)$$

The 2-nd moment is then linked to the average surface area of the precipitate

$$\bar{R}^2(t) = 4\pi \frac{\int_0^{\infty} R^2(t) \varphi(R, t) dR}{N(t)}. \quad (2.11)$$

The 3-rd moment gives the total volume, $V_P(t)$, of the precipitates

$$V_P(t) = \frac{4\pi}{3} \int_0^{\infty} R^3(t) \varphi(R, t) dR. \quad (2.12)$$

NUCLEATION RATE AND NUMBER DENSITY

In Eq. (2.1) change in the number density distribution has a source term for nucleation³. In the classical nucleation and growth theory the nucleation rate is given as [19–21]:

$$\frac{\partial N}{\partial t} = (N_{\text{total}} - N(t)) Z \beta^* \exp\left(-\frac{\Delta G^*}{k_B T}\right), \quad (2.13)$$

where Z is the Zeldovich factor [20], β^* the condensation rate [21], and ΔG^* the activation energy. N_{total} is the maximum number of available nucleation sites, k_B is the Boltzmann constant, and T is the absolute temperature. The activation energy, ΔG^* , is site dependent, e.g., for nucleation on dislocations a different activation energy is used than for nucleation in bulk.

In Eq. (2.13) the incubation time [3, 22], τ_{inc} , for nucleation is left out, so a steady-state nucleation rate is used. This is done as $\tau_{\text{inc}} = 1/(2Z^2\beta^*)$, which is considerably smaller than the time-scales that were found in the study performed here on NbC and AlN. Including the incubation time would give:

$$\frac{\partial N}{\partial t} = (N_{\text{total}} - N(t)) Z \beta^* \exp\left(-\frac{\Delta G^*}{k_B T}\right) \exp\left(-\frac{\tau_{\text{inc}}}{t}\right), \quad (2.14)$$

the incubation time lowers the initial nucleation rate to accommodate for slowing factors like for instance low diffusivity of precipitate forming elements. More details will be provided in section 2.2.5.

PRECIPITATE RADIUS

For the growth rate of precipitates the mean value approximation is used here, in which the Gibbs-Thomson effect is included to account for the interfacial energy between the precipitate and the matrix, this enters through $C_m^{\bar{R}}$ [3]. The growth rate for the average radius, \bar{R} , is given by [3, 23]:

$$\frac{d\bar{R}}{dt} = \frac{D_{\text{eff}}}{\bar{R}} \frac{C_m - C_m^{\bar{R}}}{C_m^P - C_m^{\bar{R}}} + \frac{1}{N} \frac{\partial N}{\partial t} (\alpha R^* - \bar{R}), \quad (2.15)$$

where D_{eff} is the effective diffusivity for the given nucleation site. An example for the effective diffusivity concerning precipitation on dislocations is given by Dutta and Sellars [11]. Furthermore for the growth rate there are three important concentrations for each element m in the system [13]; C_m^P the concentration of m inside the precipitate, $C_m^{\bar{R}}$ at the precipitate-matrix interface at the matrix side, and C_m the matrix concentration of element m . The growth rate given in Eq. (2.15) is used for “mean-radius” models, where the first term accounts for the growth of existing particles, and the second term for newly nucleated precipitates. α ensures precipitates that are slightly larger than the critical radius can grow, Deschamps et al. [3] use $\alpha = 1.05$. In the approximations presented here it is assumed that this correction is negligible as the highest growth rate generally occurs after the nucleation stage has ended. The growth rate that is used here will therefore be

³More background to this short description and derivation can be found in Chapter 1.

taken as⁴:

$$\frac{d\bar{R}}{dt} = \frac{D_{\text{eff}}}{\bar{R}} \frac{C_m - C_m^{\bar{R}}}{C_m^P - C_m^{\bar{R}}}. \quad (2.16)$$

Cases where the nucleation correction cannot be dismissed are studied more closely in section 2.2.7, where it is shown that this assumption is still usable.

For the interface concentration $C_m^{\bar{R}}$ the description from Deschamps [3] is used:

$$C_m^{\bar{R}} = C_m^{eq} \exp\left(\frac{R_0}{\bar{R}}\right), \quad R_0 \equiv R^* \ln\left(\frac{C_m}{C_m^{eq}}\right) \equiv \frac{2\gamma v_{\text{mol}}}{R_{\text{gas}} T} \Rightarrow C_m^{\bar{R}} = C_m^{eq} \left(\left[\frac{C_m}{C_m^{eq}}\right]^{\frac{R^*}{\bar{R}}}\right), \quad (2.17)$$

where R_0 is defined to include the Gibbs-Thomson effect, v_{mol} is the molar volume, R_{gas} is the universal gas constant in $\text{J K}^{-1} \text{mol}^{-1}$, γ is the precipitate-matrix interface energy, and C_m^{eq} is the matrix equilibrium concentration. Solving Eq. (2.16) becomes noticeably harder when the Gibbs-Thomson effect is included, which is radius dependent. However, for common precipitates under regular heat treatment conditions, the Gibbs-Thomson effect typically yields $C_m^{\bar{R}} \leq 3C_m^{eq}$ for nanometre-size precipitates using common parameter values. The effect is reduced as precipitates grow larger. The surface concentration is therefore replaced with the equilibrium concentration, then Eq. (2.16) can be rewritten to:

$$\frac{d\bar{R}}{dt} = \frac{D_{\text{eff}}}{\bar{R}} \frac{C_m - C_m^{eq}}{C_m^P - C_m^{eq}}. \quad (2.18)$$

This is the growth rate that will be used in the approximations that are made in the following sections. Note that, for both Eqs. (2.13) and (2.18), the right-hand-side is generally time-dependent.

2.2.2. REFERENCE MODEL

THE proposed approximation is compared to a multi-class KWN model as specified by Den Ouden [13], which has been encoded in Matlab, and for which the governing equations have been given in Section 2.2.1. The Den Ouden model is an improved version of the model proposed by Robson [22]. In this work it shall be used to simulate the development of a single type of precipitate, but the model allows for multiple types of precipitates to develop simultaneously. The original KWN model only considered homogeneous precipitation, and therefore in order to model precipitate formation on dislocations an adaptation of the model proposed by Zurob [10] was included in the Den Ouden model. Additionally, precipitation on grain boundaries was included.

In this chapter precipitate development in steel is considered. A single chemical composition is used in all examples: Fe 98.4695%, Mn 1.34%, Si 0.06%, Nb 0.03%, Al 0.01%, C 0.076% N 0.0061%, P 0.0058%, and S 0.0026% by weight.

The precipitate that will be studied is niobium carbide (NbC). The suggested approximations in this work are applied to the equations as described above, therefore they are equally valid for other precipitates. In the examples only nucleation at dislocations is

⁴This form is identical to the expression for individual particles in the distribution form of Eq. (2.1): $D_{\text{eff}}/R(C_m - C_m^{\bar{R}})/(C_m^P - C_m^{\bar{R}})$, cf. Den Ouden [13].

considered, however different sites can be approximated for by altering the relevant parameters in Eqs. (2.13) and (2.15). The activation energy for nucleation at dislocations is found from $\Delta G(R) = V\Delta G_V + A\gamma - \mu b^2 R \left(\frac{\ln R/b}{2\pi(1-\nu)} - \frac{1}{5} \right)$, following Zurob et al. [10, 24, 25]. The parameters used for NbC are listed in Table 2.1. The correction factor F is used in

2

Table 2.1: Model parameters used in the reference simulations. Here T is given in Kelvin, and R_{gas} is the universal gas constant in $\text{J K}^{-1} \text{mol}^{-1}$. For the solubility product the concentrations used are in wt%.

Parameter	label	value	unit
Interface energy	γ	$1.0058 - 0.4493 \cdot 10^{-3} \cdot T$	J/m^2
Molar volume	v_{mol}	13.39×10^{-6} , [10]	m^3
Bulk diffusivity [Nb]	D_{bulk}	$0.83 \cdot 10^{-4} \exp(-266500/(Rg \cdot T))$, [10]	m^2/s
Pipe diffusivity [Nb]	D_{pipe}	$4.1 \cdot 10^{-4} \exp(-172500/(Rg \cdot T))$, [10]	m^2/s
Solubility product	K_{sol}	$10^{3.42-7900/T}$, [26]	d
Dislocation density	ρ	3.27×10^{14}	$1/\text{m}^2$
Burgers vector	b	2.53144×10^{-10}	m
Correction factor	F	1.32×10^{-3} , [10]	
Poisson ratio	ν	0.293, [10]	
Shear modulus	μ	$81 - \frac{73.71(T-300)}{1810}$	GPa

the reference model and is defined by Zurob [10], where F is used to fit the model to experimental data. The value that is used here was fitted in-house for the reference model, and is comparable to the value presented by Zurob et al. F typically has an order of magnitude $F 10^{-3}$ to 10^{-2} , as it can be viewed as the average spacing between nucleation sites along a dislocation line as a multiple of the Burgers vector. The practical use of F is to determine the number of nucleation sites, $N_{\text{total}} = F\rho/b$.

2.2.3. FIRST APPROXIMATION

THE approximation is illustrated by starting from a simplified system:

1. The system is isothermal during the entire process.
2. Only precipitates of one composition are considered.
3. Only one type of nucleation site is considered, i.e., only homogeneous, or on dislocations, or on grain boundaries.
4. At the start of the process no nuclei have formed, i.e., only the initial stage of precipitation is considered in this first approximation.
5. At the end of the nucleation stage all available nucleation sites are occupied, i.e., the maximum number density is attained.
6. The matrix exists as a single phase, so no interphase precipitation occurs.
7. The incubation time is small with respect to the characteristic nucleation time defined below, i.e., $\tau_{\text{inc}} \ll \tau_{\eta}$.

Both Eq. (2.13) and Eq. (2.18) are non-linear differential equations. To approximate a solution for both equations they first rewritten for notational convenience:

$$\frac{\partial N}{\partial t} = (N_{\text{total}} - N(t)) Z \beta^* \exp\left(-\frac{\Delta G^*}{k_B T}\right) \equiv \frac{N_{\text{total}} - N(t)}{\tau_\eta(t)}, \quad (2.19)$$

and

$$\frac{d\bar{R}}{dt} = \frac{D_{\text{eff}}}{\bar{R}} \frac{C_m - C_m^{eq}}{C_m^P - C_m^{eq}} \equiv \frac{\Sigma(t)}{\bar{R}}. \quad (2.20)$$

Where the (explicitly) time-dependent parameters $\tau_\eta(t) = \exp(\Delta G^* / k_B T) / Z \beta^*$ and $\Sigma(t) = D_{\text{eff}}(C_m - C_m^{eq}) / (C_m^P - C_m^{eq})$ are defined.

Under the listed restrictions it is assumed that both $\tau_\eta(t)$ and $\Sigma(t)$ can be considered time-independent. This may be done as external variables like temperature are constant, and only a single precipitate is considered at a specific site. The approximation will essentially assumes that the matrix concentrations will not change too much. Now both equations reduce to ordinary differential equations.

When $\tau_\eta(t) = \tau_\eta(0) \equiv \tau_\eta$ and $\Sigma(t) = \Sigma(0) \equiv \Sigma$, i.e., are time-independent, Eq. (2.19) resolves to:

$$N(t) = N_{\text{pre}} + \left(1 - \exp\left(-\frac{t}{\tau_\eta}\right)\right) (N_{\text{total}} - N_{\text{pre}}), \quad (2.21)$$

where N_{pre} is the pre-existing number density, which, under the given restrictions, is equal to 0. For eq. (2.20)

$$\bar{R}(t) = \sqrt{2\Sigma t + (\bar{R}(0))^2}. \quad (2.22)$$

Here $\bar{R}(0) = R^*$, R^* is the critical radius which is constant under the used restrictions.

Some examples are presented in Figure 2.1. The approximation for precipitate number density agrees with the simulated number density from the KWN model; in the case where all the available sites are occupied. The number of available sites for dislocation precipitates is found from $F\rho/b$ [10]. The values of these three parameters are given in Table 2.1. The agreement between the approximation and simulation result can be seen in Figures 2.1b and 2.1d, in these examples $\tau_\eta = 4.6, 1.9, 3.5 \cdot 10^2$ s in the order of ascending temperature. Therefore it is worthwhile to determine when the nucleation stage starts and when it ends following Eq. (2.21). The true start and end of nucleation are at the limits $t = 0$ and $t = \infty$ respectively, so a threshold value is chosen for the start when 5% of the sites are occupied, and for the end of nucleation when 95% of the sites are occupied. These times will be labelled $t_{5\%}$ and $t_{95\%}$ respectively, and are found to be:

$$t_{5\%} = \ln(20/19)\tau_\eta \approx 0.05\tau_\eta, \quad t_{95\%} = \ln(20)\tau_\eta \approx 2.996\tau_\eta. \quad (2.23)$$

These ‘nucleation’ times provide an intuitive insight into the time interval during which nucleation plays its role in the precipitate development. Note that the quotient of $t_{95\%}$ and $t_{5\%}$ is a dimensionless constant $t_{95\%} / t_{5\%} = 58.4$, because of the idealised nature of the approximation. Furthermore, when $t_{95\%}$ is large compared to the time-scales associated with growth, the matrix concentration is likely to change significantly before all nuclei have formed. Then the initial assumption that τ_η is time-independent is likely to be invalid, this condition is discussed in Section 2.2.4.

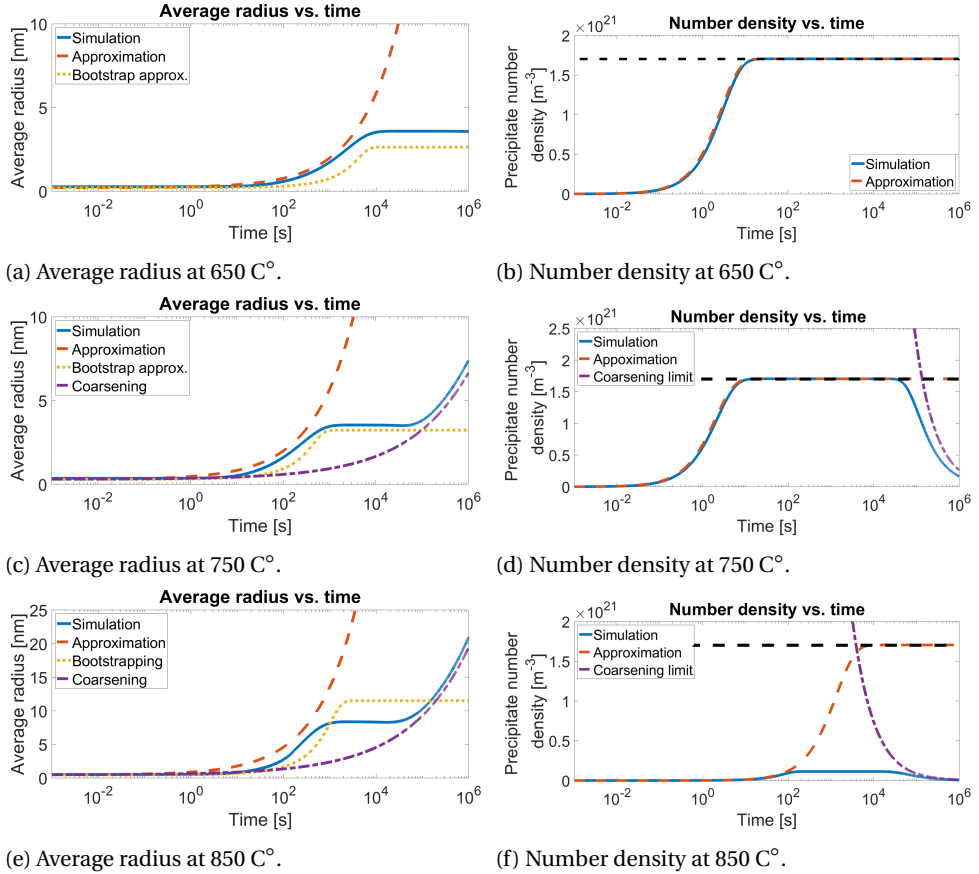


Figure 2.1: Average radius and number density of NbC precipitates at dislocations under isothermal conditions for different temperatures. The matrix composition in weight percentages is; Fe 98.4695%, Mn 1.34%, Si 0.06%, Nb 0.03%, Al 0.01%, C 0.076%, N 0.0061%, P 0.0058%, and S 0.0026%. In the blue solid line the results of the multi-class KWN model by Den Ouden [13] are given. In red dashed line the approximations from Eqs. (2.21) and (2.22) for the number density and average radius respectively are given. For the average radii (Figs. 2.1a, 2.1c, and 2.1e) in the yellow dotted line the bootstrapping results from Eq. (2.30) are given, and the purple dash-dotted line is the average radius following LSW theory [27, 28], see Eq. (2.34). And for the number density (Figs. 2.1b, 2.1d, and 2.1f) the purple dash-dotted line the maximum number density following the LSW theory, Eq. (2.36).

In figure 2.1f not all available sites are occupied, additional input is required to capture this as well, which is presented in Section 2.2.7.

2.2.4. BOOTSTRAPPING AND APPROXIMATING MATRIX CONCENTRATION

EQS. (2.21) and (2.22) are rather rough approximations; once the matrix concentration is changing due to growing precipitates the approximation breaks down, because especially the activation energy ΔG^* in the exponent of the nucleation equation, (eq. (2.13)) is sensitive to changes in the concentration [19]. To overcome this limitation ‘bootstrapping’ is performed: this bootstrapping implies substituting the previous ap-

proximations to the average size and number density. The matrix concentration, and the mass conservation law are suitable equations for this substitution. Essentially a one-step iteration is performed based on previous results. Bootstrapping applied to the evolution of the matrix concentration also leads to the derivation of a second characteristic time τ_λ from the changing matrix concentration:

$$\frac{d}{dt} [C_m] = \frac{d}{dt} \left[C_m^{\text{init}} - \frac{4\pi(C_m^P - C_m^{\text{init}})}{3} (N\bar{R}^3) \right], \quad (2.24)$$

here C_m^{init} is the initial concentration of m , Eq. (2.24) returns:

$$\frac{dC_m}{dt} = -\frac{4\pi(C_m^P - C_m^{\text{init}})}{3} \left(3N(t)\bar{R}^2(t) \frac{d\bar{R}}{dt} + (R^*)^3 \frac{dN}{dt} \right), \quad (2.25)$$

To approximate a solution for this equation some simplifications are made. First the loss of over-saturation by the newly nucleating precipitates is neglected. This may be done as the nucleation rate is high at the start of nucleation, where R^* is small, i.e., the product $(R^*)^3(dN/dt)$ is small, so a negligible amount of the solute over-saturation is consumed. When the concentration in the matrix decreases, the critical radius will increase, but the nucleation rate will also decrease. So in fact it is assumed that the over-saturation mainly decreases due to precipitate growth. As an additional assumption this growth will mainly take place when the precipitate number density has reached the maximum available number of nucleation sites, N_{total} . In section 2.2.7 this last assumption will be relaxed. So instead of using $N(t)$ it is substituted with N_{total} . Eqs. (2.21) and (2.22) can be substituted into eq. (2.25) to give:

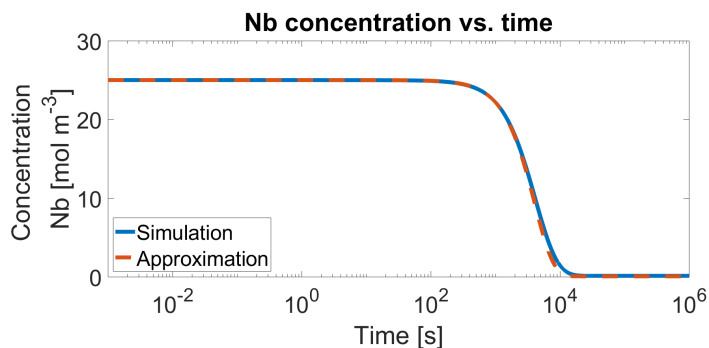
$$\begin{aligned} \frac{dC_m}{dt} &= -4\pi(C_m - C_m^{\text{init}}) \frac{(C_m^P - C_m^{\text{init}}) N_{\text{total}} D_{\text{eff}}}{C_m^P - C_m^{\text{eq}}} \sqrt{2D_{\text{eff}} \frac{C_m^{\text{init}} - C_m^{\text{eq}}}{C_m^P - C_m^{\text{eq}}}} \sqrt{t} \\ &\equiv -4\pi(C_m - C_m^{\text{init}}) \frac{\sqrt{t}}{\tau_\lambda^{3/2}}, \end{aligned} \quad (2.26)$$

where $\tau_\lambda = \frac{C_m^P - C_m^{\text{eq}}}{[(C_m^P - C_m^{\text{init}}) N_{\text{total}}]^{2/3} D_{\text{eff}} (2C_m^{\text{init}} - 2C_m^{\text{eq}})^{1/3}}$, is time-independent by virtue of the earlier restrictions and assumptions. Eq. (2.26) can be solved to yield:

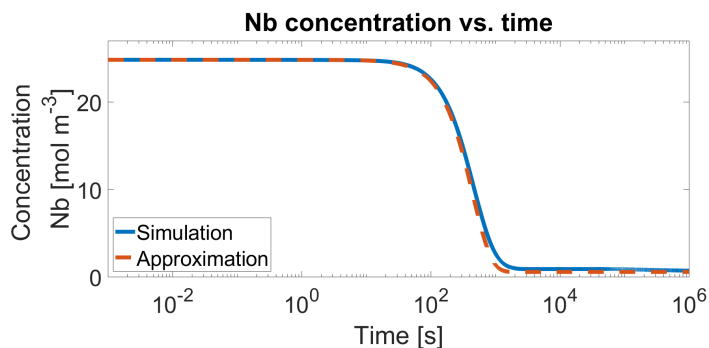
$$C_m(t) = (C_m^{\text{init}} - C_m^{\text{eq}}) \exp\left(-\frac{2}{3} \left[\frac{t}{\tau_\lambda}\right]^{3/2}\right) + C_m^{\text{eq}}. \quad (2.27)$$

Here it was assumed that for $t = 0$, $C_m(0) = C_m^{\text{init}}$. In Figure 2.2 the results are shown for NbC precipitates under isothermal conditions.

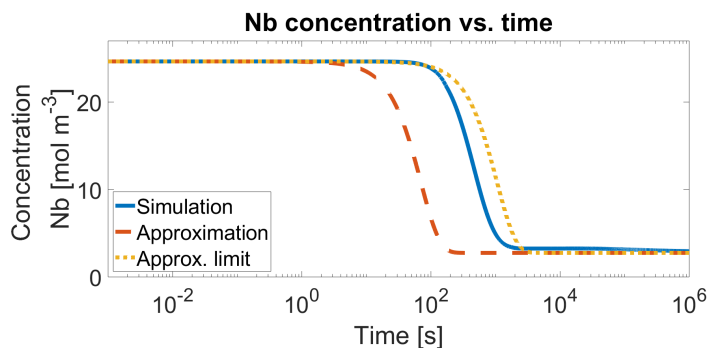
From the analytical expression in Eq. (2.27) it is also possible to define a start and end time, in a similar fashion as with the nucleation times in eq. (2.23). The starting-time, $t_{g,5\%}$, is defined as the time at which the difference between C_m^{init} and C_m^{eq} (the initial over-saturation) has decreased by 5%. The end-time, $t_{g,95\%}$, is defined as the time



(a) Matrix concentration Nb at 650 C°.



(b) Matrix concentration Nb at 750 C°.



(c) Matrix concentration Nb at 850 C°.

Figure 2.2: The time evolution of the matrix concentration of Nb under isothermal conditions for dislocation NbC precipitates. In the solid blue lines the simulated matrix concentration from the same KWN model, and in the red dashed lines the approximation from Eq. (2.27). In Fig. 2.2c the yellow dotted line uses an alternate value for N_{total} , namely N_{max} see Eq. (2.40).

at which the consumption of solute over-saturation has more-or-less ended, which is

when the initial over-saturation has decreased by 95%,

$$t_{g,5\%} = \left[-\frac{3}{2} \ln \left(\frac{19}{20} \right) \right]^{\frac{2}{3}} \tau_{\lambda} = 0.18 \tau_{\lambda}, \quad t_{g,95\%} = \left[-\frac{3}{2} \ln \left(\frac{1}{20} \right) \right]^{\frac{2}{3}} \tau_{\lambda} = 2.72 \tau_{\lambda}. \quad (2.28)$$

These times form good indicators for when the assumption that τ_{η} and Σ are time-independent loses its validity, as they tell how much the initial over-saturation has decreased, which is implicitly assumed to be constant. As with the nucleation times the quotient is also a dimensionless constant, $\frac{t_{g,95\%}}{t_{g,5\%}} = 15.05$. Using Eq. (2.27) an improvement can be made to eq. (2.20). A time-dependence is added to eq. (2.20) by substituting eq. (2.27). The new expression reads:

$$\frac{d\bar{R}}{dt} = \frac{D_{\text{eff}}}{\bar{R}} \frac{C_m - C_m^{eq}}{C_m^P - C_m^{eq}} \exp \left(-\frac{2}{3} \left[\frac{t}{\tau_{\lambda}} \right]^{\frac{3}{2}} \right). \quad (2.29)$$

Now Eq. (2.29) can be solved to return an improved solution to the average radius development over eq. (2.22),

$$\bar{R}(t) = \sqrt{\frac{12^{2/3} \Sigma}{3} \tau_{\lambda} \left[\Gamma \left(\frac{2}{3} \right) - \Gamma \left(\frac{2}{3}, \frac{2}{3} \left[\frac{t}{\tau_{\lambda}} \right]^{\frac{3}{2}} \right) \right]} + (\bar{R}(0))^2. \quad (2.30)$$

Where $\Gamma(x)$ is the gamma-function, and $\Gamma(x, y)$ is the upper incomplete gamma-function. The result is also shown in Figures 2.1a, 2.1c, and 2.1e (dotted lines). In the worked-out examples the same plateau as with the simulated result shows up, at roughly the same time. This finite limit for the average radius is due to the asymptotic behaviour of the upper incomplete gamma function. The asymptotic behaviour is the result of the use of the average radius, and the assumption that the over-saturation is completely consumed in the growth stage by the precipitates. The improved approximation then suggests an average radius at which the nucleation and growth stage ends before coarsening starts.

The average radius right before coarsening is an important value, since it provides information as to what the maximum Zener pinning would be. This follows as the Zener pinning is proportional to the ratio of the volume fraction and the average radius. At the start of coarsening the maximum volume fraction is reached approximately, so the smaller the average radius at which this volume fraction is reached the higher the Zener pinning.

Now τ_{η} and τ_{λ} have been defined, they can both be used as characteristic times for nucleation and growth respectively. Under the restrictions given in section 2.2.3 $\tau_{\lambda} \gg \tau_{\eta}$, this indicates that the loss of over-saturation becomes only significant after nucleation has virtually stopped. The form of Eqs. (2.21) and (2.27) provides a handle on how far the nucleation or decrease in over-saturation has progressed, after τ_{η} units of time $\approx 63.2\%$ of the maximum number density is reached, similarly after $(3/2)^{\frac{2}{3}} \tau_{\lambda}$ units of time $\approx 63.2\%$ of the over-saturation has been consumed by the precipitates. When $\tau_{\lambda} \leq \tau_{\eta}$ the approximations that were made need corrections to be able to provide a useful result. This is analysed in section 2.2.7.

2.2.5. INCUBATION TIME

SOME additional remarks must be made regarding the incubation time τ_{inc} . The incubation time has been considered negligible in this work as in many cases $\tau_{\text{inc}} \ll \tau_{\eta}$. However when τ_{inc} is comparable to τ_{η} it cannot be neglected. When it is included in eq. (2.19) as found in literature [3, 22] the solution becomes more complicated and much less intuitive than the result presented in eq. (2.21). Additionally, the approximate result derived here becomes less accurate. However, when $\tau_{\text{inc}} \sim \tau_{\eta}$ it is possible to still use eq. (2.21) by shifting time by τ_{inc} . This shift can be used when nucleation is relatively quick compared to growth, see section 2.2.7. The predicted average radius and matrix concentration, may be shifted in time similarly. The use of this shift has been verified, an example is presented in Figure 2.2. Note that when $\tau_{\text{inc}} \sim \tau_{\lambda}$ and $\tau_{\text{inc}} \geq \tau_{\eta}$ one cannot neglect incubation time nor shift the approximations as described above because then nucleation and loss of over-saturation interfere.

However in this work the timescale for nucleation τ_{η} is given as $\tau_{\eta} = \frac{1}{Z\beta^* \exp\left(\frac{-\Delta G^*}{k_B T}\right)}$, and for consumption of over-saturation τ_{λ} goes with $\tau_{\lambda} \sim 1/((N_{\text{total}})^{2/3} D_{\text{eff}})$. It may be noted that these times as well as τ_{inc} increase when temperature, dislocation density, or diffusivity decrease, and vice-versa, albeit at a different rate for each timescale. In particular note that $\tau_{\text{inc}}/\tau_{\eta} = \exp\left(\frac{-\Delta G^*}{k_B T}\right)/Z$, which has an absolute maximum in the domain $T = [0, \infty)$. When at this maximum $\tau_{\text{inc}} \ll \tau_{\eta}$, the incubation time can be neglected. In the examples of section 2.2.3 the maximum is at $\tau_{\text{inc}}/\tau_{\eta} \approx 2.2 \cdot 10^{-3}$ at $T \approx 670^\circ\text{C}$, so incubation time can safely be neglected. Alternatively in the examples of section 2.2.3 in the order of ascending temperature, i.e., 650°C , 750°C and 850°C we find $Z = 0.38, 0.19, 0.07$ and $\beta^* = 3.6 \cdot 10^2, 6.3 \cdot 10^3, 1.0 \cdot 10^5 \text{ s}^{-1}$ with the incubation times $\tau_{\text{inc}} = 9.7 \cdot 10^{-3}, 2.3 \cdot 10^{-3}, 9.6 \cdot 10^{-4} \text{ s}$. And $\tau_{\lambda} = 2.4 \cdot 10^5, 2.7 \cdot 10^4, 4.3 \cdot 10^3 \text{ s}$, so incubation time is not significant for the results presented here.

2.2.6. COARSENING

THE approximate solutions derived so far only consider nucleation and growth. As shown in Figure 2.1, coarsening in this approximation cannot be included, because the mean particle size only is considered. However, it is possible to use the LSW theory [27, 28] for this purpose. The LSW theory solves the precipitate size distribution of eq. (2.1) in the coarsening limit, and gives a description of the precipitate growth during coarsening. The resulting curve for the examples mentioned before can be found in the purple dash-dotted lines in Fig. 2.1, where the coarsening growth rate found in Eq. (2.33) is plotted from $t=0$. When coarsening occurs in the simulation, the LSW theory and the simulation outcome follow the same curve, i.e., have the same time-dependence. Coarsening must be modelled explicitly for the mean-radius approach [3]:

$$\frac{d\bar{R}}{dt} = \frac{4}{27} \frac{C_m^{eq}}{C_m^P - C_m^{eq}} \frac{D_{\text{eff}}}{\bar{R}^2} \frac{2\gamma\nu_{\text{mol}}}{R_{\text{gas}} T}. \quad (2.31)$$

For clarity Ω is defined as:

$$\Omega = \frac{4}{27} \frac{C_m^{eq}}{C_m^P - C_m^{eq}} D_{\text{eff}} \frac{2\gamma\nu_{\text{mol}}}{R_{\text{gas}} T}. \quad (2.32)$$

This can be solved as an ordinary differential equation,

$$\bar{R}(t) = [3\Omega t]^{1/3} + \bar{R}_1 \Rightarrow \bar{R}(t) = \left[\frac{4}{9} \frac{C_m^{eq}}{C_m^P - C_m^{eq}} D_{\text{eff}} \frac{2\gamma v_{\text{mol}}}{R_{\text{gas}} T} \right]^{1/3} t^{1/3} + \bar{R}_1. \quad (2.33)$$

Where \bar{R}_1 is the average radius at the start of coarsening [27], provided that eq. (2.33) starts at coarsening, alternatively one can use the asymptotic value from eq. (2.30). LSW theory is only valid on large time-scales, i.e., when coarsening would normally occur. The coarsening curves in this work were plotted from $t = 0$, using $\bar{R}_1 = \bar{R}(0) = R^*$, as it is known that the LSW result should emerge at long time-scales. Here it is found that the average radius of the precipitates grows with $t^{1/3}$. This time-dependence is confirmed when eq. (2.33) is included in the example simulations in Figure 2.1 for the cases where coarsening occurs. Strictly speaking eq. (2.31) is derived for homogeneously nucleated precipitates. The same time dependency is found by Hoyt [29] for precipitates at grain boundaries, and at dislocations. From Hoyt's article we remark that at low temperatures the time dependency can go to $t^{1/4}$ or even $t^{1/5}$, which was theorised by both Speigh and Kreye [30, 31]. The lower exponent in the time-dependency is a consequence of the decrease of the bulk diffusion, becoming negligible at low temperatures. It has been experimentally observed by Smith in the 1960's [32, 33]. Hoyt analysed precipitates at a grain boundary, the result reads

$$\bar{R}(t) = \left[\frac{4}{9} \frac{2\gamma v_{\text{mol}}^2}{R_{\text{gas}} T} C_m^{eq} \left(D_{\text{bulk}} + \frac{1}{2} \sqrt{aD_{\text{gb}}h} \right) \right]^{1/3} t^{1/3}, \quad (2.34)$$

where h is the convection coefficient, which is a non-negative constant, a is the thickness of the boundary slab, i.e., the grain boundary and its direct neighbour layer, D_{bulk} the bulk diffusivity, D_{gb} is the grain boundary diffusivity, v_{mol} is the molar volume, and γ is the interface energy for the precipitate.

In the multi-class approach there is no explicit coarsening growth rate, the transition from nucleation and growth to coarsening happens naturally, due to the underlying size-distribution and the Gibbs-Thomson effect. However, assuming spherical precipitates, the average radius grows with $t^{1/3}$. Using this proportionality of the growth rate, an upper bound for the number density during coarsening can be found from the conservation law of mass.

$$N \leq \frac{3}{4\pi} \frac{C_m^{\text{init}} - C_m^{eq}}{C_m^P} \frac{1}{\bar{R}^3}. \quad (2.35)$$

Now substituting eq. (2.34) results in an asymptote for the number density:

$$N \leq \frac{3}{4\pi} \frac{C_m^{\text{init}} - C_m^{eq}}{C_m^P} \frac{1}{C_m^{eq}} \left(D_{\text{bulk}} + \frac{1}{2} \sqrt{aD_{\text{gb}}h} \right)^{-1} \frac{1}{t} \equiv \frac{\kappa}{t}. \quad (2.36)$$

This asymptote is shown in Figures 2.1d and 2.1f. From the asymptotic behaviour a coarsening time can be found at equality in Eq. (2.36). In other words, when the number density reaches the maximal density N_{total} , the asymptote from eq. (2.36) will intersect the number density at a time t_{coarse} which can be written as

$$t_{\text{coarse}} = \frac{\kappa}{N_{\text{total}}}, \quad (2.37)$$

t_{coarse} is an estimate of the time at which coarsening starts, thus completing the picture of the precipitation development.

2.2.7. COMPETITION BETWEEN NUCLEATION AND GROWTH

IN Figure 2.1 all potential nucleation sites get occupied at 650C° and 750C° (Figs. 2.1b and 2.1d), but not at 850C° (Fig. 2.1f). This is a consequence of a competition between nucleation rate and growth rate. So not all sites will necessarily be used, in particular when the nucleation rate is low compared to the growth rate. When the growth rate is high relative to the nucleation rate, the over-saturation decreases rapidly thus removing the driving force for nucleation before potential nucleation sites had a chance to surpass the critical stage, this can be seen in Figure 2.1f. This means that the fifth restriction listed in section 2.2.3 is not met.

In section 2.2.4 for both τ 's it was shown that it is possible to make a quick analysis of the progress of the nucleation and loss of over-saturation, generally it is assumed that the nucleation and decrease in over-saturation are finished after 5 times the characteristic times that were shown (in fact 99.3% of the transition is done). By this reasoning the nucleation is practically finished after $5\tau_\eta$, when precipitate growth would not occur. For the start of growth, which was originally defined with $t_{g,5\%}$ as a 5% decrease in over-saturation, one might argue (by virtue of linearising the exponential function) that this decrease in over-saturation occurs after about $0.05\tau_\lambda$. Here the end-of-nucleation and start-of-growth have been shifted closer to each other to ensure that they are well separated. Now a dimensionless parameter S may be defined to characterise the condition when all potential nucleation sites will be occupied.

$$S = \log_{10} \left(\frac{0.05\tau_\lambda}{5\tau_\eta} \right) = \log_{10} \frac{\tau_\lambda}{\tau_\eta} - 2. \quad (2.38)$$

When $S > 1$ the nucleation and growth phases are well-separated and the approximations made in sections 2.2.3 and 2.2.4 will return good results. In the case that $S < 1$ not all nucleation sites will be occupied by a precipitate. So N_{total} is not reached, which means that the approximation needs to be adapted. The maximum reached precipitate number density $N_{\text{max}} (< N_{\text{total}})$ is estimated to be reached when the over-saturation is removed by the growing precipitates. N_{max} is estimated by substituting eq. (2.22) into eq. (2.35):

$$N \leq \frac{3}{4\pi} \frac{C_m^{\text{init}} - C_m^{\text{eq}}}{C_m^{\text{p}}} \frac{1}{\left(2D_{\text{eff}} \frac{C_m^{\text{init}} - C_m^{\text{eq}}}{C_m^{\text{p}} - C_m^{\text{eq}}} \right)^{3/2} t^{3/2}}. \quad (2.39)$$

Then N_{max} is found by substituting eq. (2.21) and solving for time t :

$$N_{\text{max}} = N_{\text{total}} \left(1 - e^{-Z\beta^* \exp(-\Delta G^*/(k_B T))t} \right) = \frac{3}{4\pi} \frac{C_m^{\text{init}} - C_m^{\text{eq}}}{C_m^{\text{p}}} \frac{1}{\left(2D_{\text{eff}} \frac{C_m^{\text{init}} - C_m^{\text{eq}}}{C_m^{\text{p}} - C_m^{\text{eq}}} \right)^{3/2} t^{3/2}} \equiv \frac{\vartheta}{t^{3/2}}. \quad (2.40)$$

When N_{max} is reached nucleation ends, so t may be labelled as a new end-of-nucleation time t_{eon} . A direct solution can be found from linearising the exponent using Taylor expansion: $t_{\text{eon}} = [\vartheta\tau_\eta/N_{\text{total}}]^{2/5}$, alternatively the bisection method can be used to find

N_{\max} . This would also return a new coarsening time t'_{coarse} , with $t'_{\text{coarse}} = \kappa / N_{\max}$. This is illustrated in Figure 2.3.

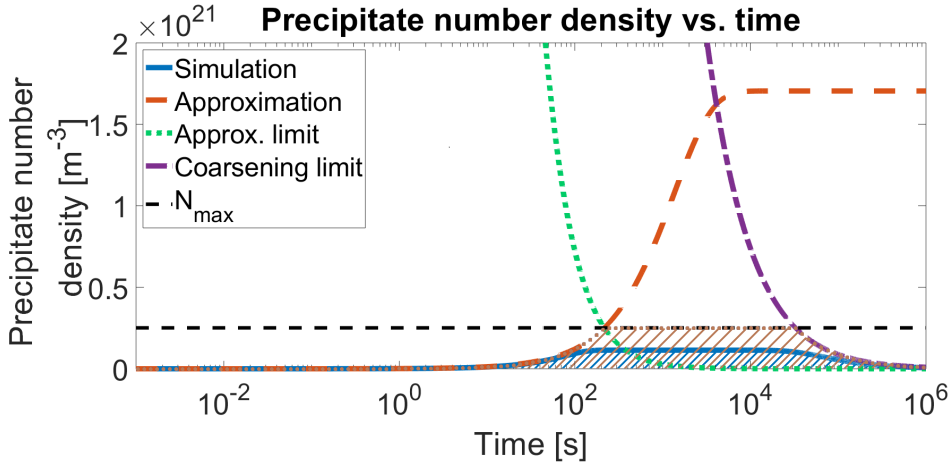


Figure 2.3: Here an example is worked out where N_{total} is not reached. The system is isothermal at 850°C . The solid blue line represents the reference simulation result, the area below is shaded in blue, and the red dashed line the approximation of Eq. (2.21). The growth asymptote from Eq. (2.39) is given in the green dotted line, from which N_{\max} is found. And the coarsening asymptote from Eq. (2.35) is given in the purple dash-dotted line. The maximum number density N_{\max} is also included in the black dashed (horizontal) line. In the brown dotted curve, and the shaded area below, shows the result of the combined approximation results..

2.3. DERIVATION FOR QUASI-ISOTHERMAL PRECIPITATION

TEMPERATURE is generally not constant in an industrial process. Therefore the isothermal restriction is relaxed, which means that τ_η , Σ , and τ_λ can no longer be assumed time independent. The proposed solution is to create quasi-isothermal time intervals, so the temperature-time curve is approximated by a series of isothermal steps. When the difference in temperature between the steps is small τ_η , Σ , and τ_λ can be updated at the beginning of each domain, the i -th time interval is defined as $[t_i, t_{i+1}]$. For each time interval the eqs. (2.21), (2.22), (2.27) and (2.30) are connected at the domain boundaries. Before examining the results for a heating and cooling path this is to be re-examined. Consider eq. (2.21) rewritten for clarity:

$$N(t) = N_{\text{total}} - (N_{\text{total}} - N_{\text{pre}}) e^{-\frac{t}{\tau_\eta}}. \quad (2.41)$$

On the i -th interval it is rewritten as:

$$N_i(t) = N_{\text{total}} - (N_{\text{total}} - N_{i-1}(t_i)) e^{-\frac{t-t_i}{\tau_{\eta,i}}}. \quad (2.42)$$

At each time interval a boundary condition is needed such that all intervals are linked continuously, this means $N_i(t_i) = N_{i-1}(t_i)$ at the start of the i -th interval. Where it is noted that $N_0(t_0) = N_{\text{pre}}$. A similar situation occurs for the growth rate on interval i :

$$R_i(t) = \sqrt{2\Sigma_i(t-t_i) + [R_{i-1}(t_i)]^2}, \quad (2.43)$$

where $R_i(t_i) = R_{i-1}(t_i)$, and $R_0(t_0) = R^*$. And for the concentration on interval i :

$$C_{m,i}(t) = (C_{m,i-1}(t_i) - C_m^{eq}) e^{-\frac{2}{3} \left[\frac{t-t_i}{\tau_{\lambda,i}} \right]^{3/2}} + C_m^{eq}, \quad (2.44)$$

where $C_{m,i}(t_i) = C_{m,i-1}(t_i)$, and $C_{m,0}(t_0) = C_m^{\text{init}}$.

The choice for defining the time-interval size is dependent on the cooling or heating rate, because the parameters are temperature dependent. An exact step size for the temperature change is hard to provide, as there are multiple parameters that change at different rates under the influence of temperature. However, it is possible to calculate the parameter values and check the change with each temperature domain, if this change becomes too large a new domain starts. Smaller temperature steps will improve the approximation, however note that common temperatures in heat treatments for steel are higher than $> 500\text{C}^\circ$. Therefore a constant step-size of 1C° could be sufficient, as the change in temperature in each step is much less than 1%, the change in parameter values for each interval is also small. With these quasi-isothermal intervals, and the corrections made in Eqs. (2.42), (2.43), and (2.44) to the approximation, it is possible to approximate the precipitate development for non-isothermal processes. In Figure 2.4a reheating curve is used, in Figure 2.4d the dashed line suffers from a computational artefact therefore a jump is seen, the maximum concentration is forced externally as the initial concentration. In Figure 2.5 two cooling curves are given, one for the minimum coil temperature, and one for the average temperature.

2.4. DISCUSSION ON VALIDITY AND LIMITATIONS

THE approximations are based on a number of assumptions. It is therefore necessary to examine the validity of the assumptions:

1. Isothermal: the most influential parameter is the temperature. Most practical applications are not operating under isothermal conditions. Therefore it was demonstrated that the non-isothermal time-domain can be divided into several isothermal intervals. On each interval the parameters τ_η , Σ , and τ_λ are evaluated, and considered constant on the specific interval.
2. Matrix concentration: the second most important condition is the rate of change in the matrix concentration. This issue is partially resolved by the fact that the approximation is aimed at the initial stage of precipitation, when the concentration is practically constant. After the initial stage the matrix concentration will be changing, but the change can be corrected for in the growth rate to the first order. A correction can be made using the bootstrapping method to find the concentration time-dependence, see eq. (2.27). The result can be applied to correct the growth rate, as seen in eq. (2.30). Where it must be noted that the approximation does not include coarsening. Another problem that can arise is that the nucleation rate is too low, in that case the original number density limit N_{total} is not reached before the over-saturation disappears. A new number density limit, N_{max} , is estimated by using the physical limits on the precipitate population. As this is an estimate based on approximations, the value of N_{max} is first and foremost an estimate of the order of magnitude of the maximum number density. Still, as it is a

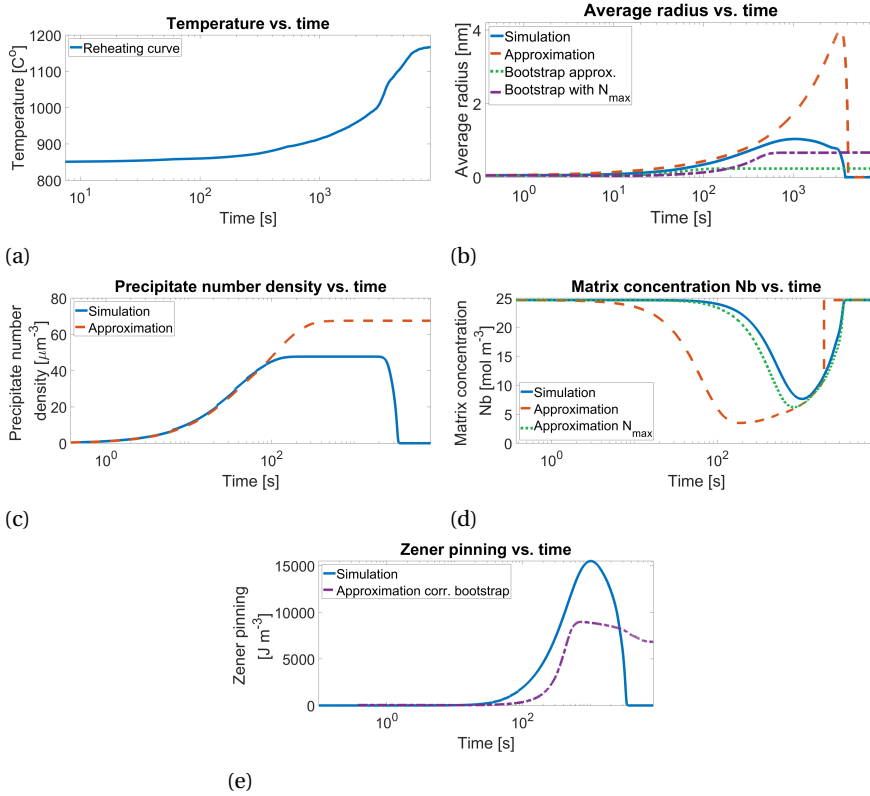


Figure 2.4: Reheating example, in 2.4a the temperature-time curve, in 2.4b the average radius, in 2.4c the precipitate number density, in 2.4d the matrix concentration of Nb, and in 2.4e the calculated Zener pinning pressure. The blue solid lines show the simulation results, the red dashed lines show the approximations from Eqs. (2.21), (2.22) and (2.27). The result of Eq. (2.30) is also given in 2.4b, and a correction to Eq. (2.27) is given in 2.4c.

great improvement over using N_{total} , this new limit is applied to further enhance the concentration time-dependence. With these corrections in combination with the LSW theory it is possible to approximate the entire precipitate development cycle, as demonstrated in Figures 2.1 and 2.3.

3. Number of precipitate types and sites: the approximation only counts one type of precipitate, e.g., M_xC_y , and also at one nucleation site. Now if there are multiple precipitate types that do not interfere, i.e., compete for sites or resources they could easily coexist. However competition for, say nitrogen or nucleation sites, is not included. We propose to use this approximation as a simple estimator to predict the precipitation behaviour of the system. One can think of estimating which type of precipitate will appear first or which type will reach the coarsening stage first. This provides key insight into which type of precipitate will dominate the precipitate development of the entire system. It is technically possible to in-

clude competition. However this complicates calculations in such a way that the approximate approach loses its appealing feature, which is firstly to provide quick intuitive results.

2

2.5. CONCLUSIONS

AN approximation to the isothermal mean-value precipitation model was derived. First for cases where all available nucleation sites are occupied, the average radius and the number density were approximated. Based on the solutions for average radius and number density an approximation to the time-dependence of the matrix concentration, and from that a correction to the average radius, were found as well. The approximation was then applied under less restrictive conditions, first in the situation where not all sites are occupied before the end of nucleation. Finally the approximation was adapted and applied to non-isothermal situations.

In the derivations the parameters τ_η , Σ , and τ_λ have been defined, where τ_η , and τ_λ are the characteristic times for nucleation and loss of over-saturation respectively (see eqs. (2.19) and (2.26)), and Σ is a characteristic parameter for growth (see eq. (2.20)). An intuitive characterisation can be made based on these parameters, for instance when all sites are occupied five times can be defined: (i) a start-of-nucleation time, $t_{5\%}$; (ii) an end-of-nucleation time, $t_{95\%}$; (iii) a start-of-growth time $t_{g,5\%}$; (iv) an end-of-growth time $t_{g,95\%}$; (v) a coarsening time t_{coarse} .

Two dimensionless constants were found by taking the quotients of the end and start times: (i) for nucleation $t_{95\%} / t_{5\%} = 58.4$; (ii) for growth, i.e., when the over-saturation is consumed $t_{g,95\%} / t_{g,5\%} = 15.05$. Another dimensionless parameter, $S = \log_{10}(\tau_\lambda / \tau_\eta) - 2$, was found that characterises the precipitation process as it tells whether the nucleation occurs faster than the growth of the precipitates or not. Secondly it provides an indication to the correctness of the assumption that τ_η , Σ , and τ_λ are time-independent. Parameter S describes the separation of the nucleation and loss of over-saturation during growth. If $S > 1$, these two events are well separated, but if $S < 1$ nucleation will not fill all available nucleation sites and growth will occur simultaneously with nucleation. In the $S < 1$ regime three additional parameters were found: (i) The maximally reached number density, N_{max} ; (ii) the 'new' end-of-nucleation time, t_{eon} ; (iii) and an updated coarsening time, t'_{coarse} .

Together these times and parameters provide an intuitive insight in the precipitate radius and number density development during precipitation before any numerical simulations need to be performed, providing much faster and clear process information. Which is useful for both simulations, and for process control. With this approximation it is possible to get on-line insight in the final product. As demonstrated, the approximation can be applied to a quasi-isothermal approach in which non-isothermal cases can be approximated. The quasi-isothermal approach can be used to approximate results for experimental and industrial precipitate systems.

REFERENCES

- [1] R. J. Slooter, M. H. F. Sluiter, W. G. T. Kranendonk, and C. Bos. Approximation and characteristic times in precipitation modelling. *ISIJ international*, 61(5), 2021.

- [2] T. Gladman. *The physical metallurgy of microalloyed steels*. CRC Press, second edition, 2001.
- [3] A. Deschamps and Y. Bréchet. Influence of predeformation and ageing of an Al-Zn-Mg alloy - II. modeling of precipitation kinetics and yield stress. *Acta materialia*, 47(1):293–305, 1999.
- [4] A. J. Ardell. Precipitation hardening. *Metallurgical transactions A*, 16A:2131–2165, December 1985.
- [5] A. Deschamps, F. Livet, and Y. Bréchet. Influence of predeformation on ageing in an Al-Zn-Mg alloy - I. microstructure evolution and mechanical properties. *Acta materialia*, 47(1):281–292, December 1999.
- [6] G. E. Dieter Jr. *Mechanical metallurgy*. McGraw-Hill book company, second edition, 1988.
- [7] S. Nandy, K. K. Ray, and D. Das. Process model to predict yield strength of AA6063 alloy. *Materials science and engineering: A*, 644:413–424, 2015.
- [8] S. Esmaeili, D. J. Lloyd, and W. J. Poole. A yield strength model for the Al-Mg-Si-Cu alloy AA6111. *Acta materialia*, 51:2243–2257, 2003.
- [9] S. Esmaeili and D. J. Lloyd. Modeling of precipitation hardening in pre-aged AlMgSi(Cu) alloys. *Acta materialia*, 53:5257–5271, 2005.
- [10] H. S. Zurob, C. R. Hutchinson, Y. Brechet, and G. Purdy. Modeling recrystallization of microalloyed austenite: effect of coupling recovery, precipitation and recrystallization. *Acta materialia*, 50:3075–3092, 2002.
- [11] B. Dutta, E. J. Palmiere, and C. M. Sellars. Modelling the kinetics of strain induced precipitation in Nb microalloyed steels. *Acta materialia*, 49:785–794, 2001.
- [12] R. Kampmann and R. Wagner. Kinetics of precipitation in metastable binary alloys - Theory and application to Cu-1.9 at% Ti and Ni 14 at% Al. In P. Haasen, V. Gerold, R. Wagner, and M. F. Ashby, editors, *Decomposition of alloys: the early stages: proceedings of the 2nd acta-scripta metallurgica conference*, number 2 in 2. Acta metallurgica, Pergamon press, 1984.
- [13] D. den Ouden, L. Zhao, C. Vuik, J. Sietsma, and F. J. Vermolen. Modelling precipitate nucleation and growth with multiple precipitate species under isothermal conditions: Formulation and analysis. *Computational materials science*, 79:933–943, 2013.
- [14] M. Perez, M. Dumont, and D. Acevedo-Reyes. Implementation of classical nucleation and growth theories for precipitation. *Acta materialia*, 56:2119–2132, March 2008.
- [15] Q. Du and Y. Li. An extension of the Kampmann-Wagner numerical model towards as-cast grain size prediction of multicomponent aluminum alloys. *Acta Materialia*, 71:380–389, June 2014.

- [16] Y. Li, B. Holmedal, H. Li, L. Zhuang, J. Zhang, and Q. Du. Precipitation and strengthening modeling for disk-shaped particles in aluminum alloys: Size distribution considered. *Materialia*, 4:431–443, 2018.
- [17] J. D. Robson. Modeling precipitate evolution in zirconium alloys during irradiation. *Journal of nuclear materials*, (476):123–131, 2016.
- [18] H. M. Hulburt and S. Katz. Some problems in particle technology, a statistical mechanical formulation. *Chemical engineering science*, 19:555–574, 1964.
- [19] M. Volmer and A. Weber. Keimbildung in übersättigten Gebilden. *Zeitschrift für Physikalische Chemie*, 119:277–301, 1926.
- [20] Ya. B. Zeldovich. On the theory of new phase formation: cavitation. *Acta physicochim USSR*, 18:1–22, 1943.
- [21] R. Becker and W. Döring. Kinetische Behandlung der Keimbildung in übersättigten Dämpfen. *Annalen der Physik*, 416(8):719, 1935.
- [22] J. D. Robson. Modelling the overlap of nucleation, growth and coarsening during precipitation. *Acta materialia*, 52(15):4669–4676, 2004.
- [23] C. Zener. Theory of growth of spherical precipitates from solid solution. *Journal of applied physics*, 20:950–953, October 1949.
- [24] R. Gómez-Ramírez and G. M. Pound. Nucleation of a second solid phase along dislocations. *Metallurgical transactions*, 4(6):1563–1570, June 1973.
- [25] S. Okaguchi and T. Hashimoto. Computer model for prediction of carbonitride precipitation during hot working in Nb-Ti bearing HSLA steels. *ISIJ international*, 32(3):283–290, 1992.
- [26] K. Narita. Physical chemistry of the groups IVa (Ti, Zr), Va (V,Nb,Ta) and the rare earth elements in steel. *Transactions of the iron and steel institute of Japan*, 15:145–152, 1975.
- [27] I. M. Lifshitz and V. V. Slyozov. The kinetics of precipitation from supersaturated solid solutions. *Journal of physical chemistry solids*, 19(1-2):35–50, 1961.
- [28] C. Wagner. Theorie der Alterung von Niederschlägen durch Umlösen. *Zeitschrift für elektrochemie*, 65:581–594, 1961.
- [29] J. J. Hoyt. On the coarsening of precipitation located on grain boundaries and dislocations. *Acta metallurgica et materialia*, 39(9):2091–2098, September 1991.
- [30] M. V. Speigh. Growth kinetics of grain-boundary precipitates. *Acta metallurgica*, 16(1):133–135, January 1968.
- [31] H. Kreye. Influence of dislocations on the growth of particles. *Zeitschrift für Metallkunde*, 61:108, 1970.

- [32] A. F. Smith. The isothermal growth of UAl_2 precipitates in uranium containing 250 p.p.m. iron 700 p.p.m. aluminium. *Journal of the less common metals*, 9(4):233–243, October 1965.
- [33] A. F. Smith. The isothermal growth of manganese precipitates in a binary magnesium alloy. *Acta metallurgica*, 15(12):1867–1873, December 1967.

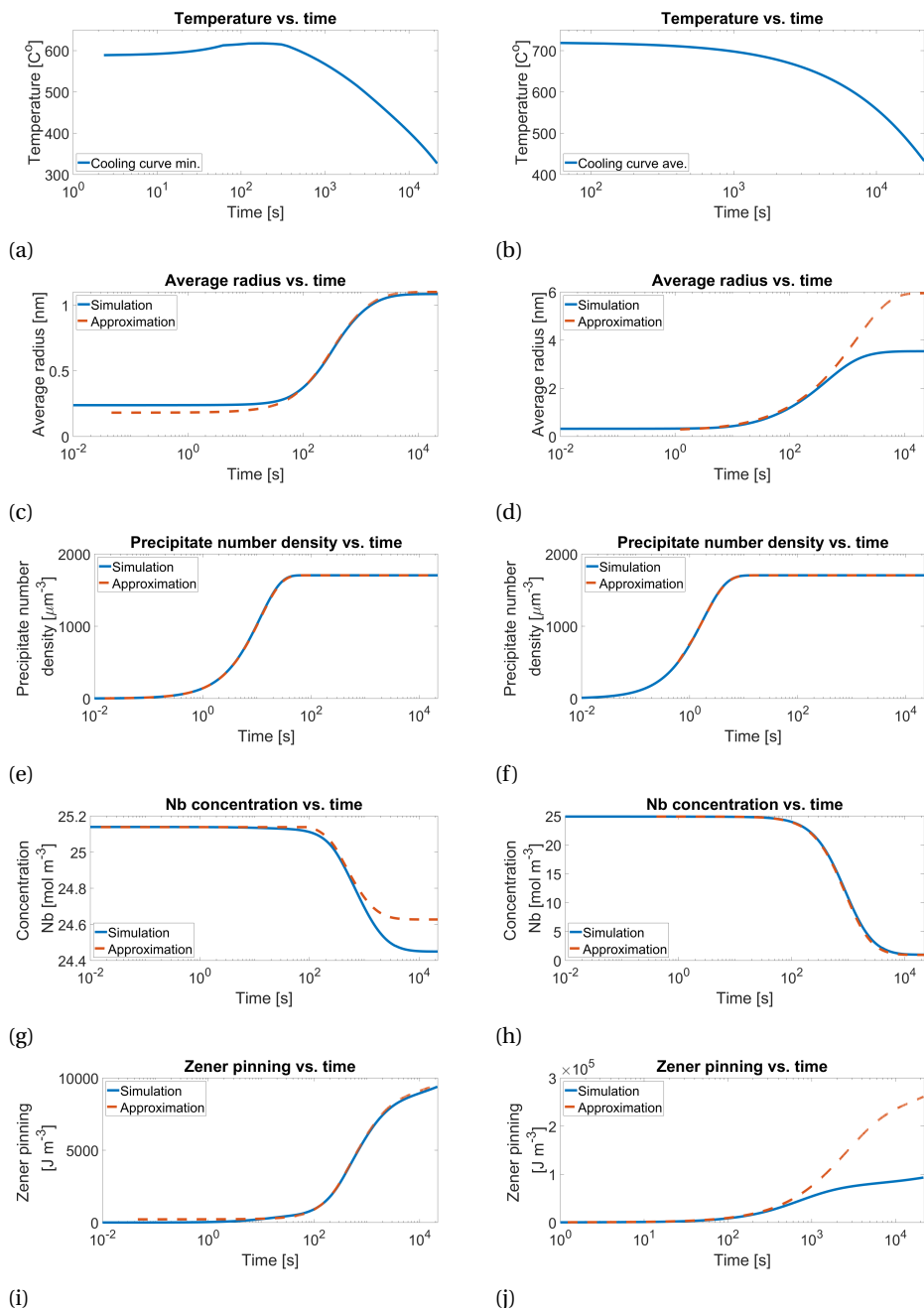


Figure 2.5: Similar to Fig. 2.4, but now for two calculated cooling curves at two different locations in one steel coil. In 2.5a, 2.5c, 2.5e, 2.5g, and 2.5i respectively the temperature-time curve, the average radius, the precipitate number density, the matrix concentration of Nb, and the calculated Zener pinning pressure at the minimum temperature, and in the same order 2.5b, 2.5d, 2.5f, 2.5h, and 2.5j for the average temperature. The solid lines show the KWN result, the dashed lines show the approximations. In 2.5j the difference occurs as in this model only an average radius is considered, whereas in the reference KWN model the precipitate volume fraction is determined from the size distribution.

3

A REFERENCE-FREE MEAM POTENTIAL FOR α -Fe AND γ -Fe

*And I gave my heart to know wisdom, and to know madness and folly: I perceived that
this also is vexation of spirit.
For in much wisdom is much grief: and he that increaseth knowledge increaseth sorrow.*

Ecclesiastes 1:17-18

*Croire, comme les politiciens, à la puissance transformatrice des lois, c'est oublier que
derrière les phénomènes visibles, se trouvent toujours des forces invisibles qui les
déterminant.*

Gustave Le Bon

A Reference-Free Modified Embedded Atom Method (RF-MEAM) potential for iron has been constructed. The new potential is made to predict both bcc and fcc (α -Fe and γ -Fe) lattice properties, with a special interest in modelling in the 800-1300 K temperature range. This is the range in which transformations and key processes in steel occur. RF-MEAM potentials can be used directly in commonly used molecular dynamics simulation software (e.g. LAMMPS). The new potential is compared to several other (Modified) Embedded Atom Method (MEAM) potentials which are commonly used. It is demonstrated that the new potential combines good characteristics for point defect energies with free surface and stacking fault energies. Also the Nishiyama-Wassermann and Kurdjumov-Sachs orientation relation ratios and interface energies are reproduced, allowing for simulations of α -Fe and γ -Fe interphases.

The contents of this chapter have been published in Journal of Physics: Condensed Matter [1].

3.1. INTRODUCTION

A key component for molecular dynamics (MD) simulations is an interatomic potential capable of predicting experimental material properties accurately. For iron several potentials have been constructed [2–9], several of these potentials were constructed using the Embedded Atom Method (EAM) [2, 4, 5, 8] or Modified Embedded Atom Method (MEAM) [6, 9] formalisms. More recently Machine-Learning Potentials (MLP) like Gaussian Approximation Potentials (GAP) [10] and Neural Network Potentials (NNP) [11] have seen increased interest, however existing MLP's are not fit to experimental but rather Density Functional Theory (DFT) data as MLP's require larger datasets to train than experiments can provide. An issue with DFT is that it finds different material properties for γ -Fe than what is experimentally observed. Additionally MLP's prove impractical for systems containing large numbers ($\sim 10^6$) of atoms as the MLP formalisms are computationally demanding. Furthermore current MLP's are made for highly specialised applications, e.g., dislocation dynamics [11], whereas the potential in this work is aimed at general simulation at finite temperatures.

The original EAM formalism has some shortcomings, particularly for systems where directional bonding plays a role, e.g., elements from the middle of the transition metal series especially bcc metals such as Fe, and semi-conductors [12]. The MEAM formalism has subsequently been made to address the issues concerning directional bonding. However MEAM potentials are tied to a particular reference structure and its associated zero-temperature Rose universal equation of state (EoS) to find its total energy [13]. Timonova and Thijssse [14] have developed an improved MEAM formalism which they have called Reference Free (RF)-MEAM. RF-MEAM removes the dependency of the potential on the Rose equation, thus removing the need for a particular reference structure, hence the name. The RF-MEAM formulation is used here to construct an improved interatomic potential for iron, applicable to both the ferrite (bcc) and austenite (fcc) phase.

Many EAM potentials have a similar analytical form as the RF-MEAM potential, e.g., [2, 4, 5, 15, 16]. It is therefore convenient to use these EAM potentials as a starting-point for fitting RF-MEAM potentials. The use of a prior EAM potential eases the finding of an acceptable local minimum from the many local minima in the parameter space. Existing EAM potentials can be enhanced by adding angular functions for the local electron density. In this work this method is illustrated for iron in Section 3.2, but it may be applied to other systems for which an EAM potential is available, e.g., vanadium [15], or a system containing both iron and carbon [16].

The widely used EAM potential by Ackland et al. [2] was chosen as the point of departure to construct a RF-MEAM potential as formulated by Duff et al. [17]. The Ackland potential performs well for predicting several properties of α -Fe, notably various point defects. Simultaneously there is room for improvement in the description of the γ -Fe phase, as the elastic constants and lattice parameter are not well predicted by the potential for this phase. The new potential is fitted to experimental data where possible, as there is no direct experimental data available for the elastic constants of γ -Fe at 0 K an extrapolation of high-temperature neutron scattering data [18] is performed. Details for this extrapolation are provided in Section 3.2.3.

The potential presented in this work performs well for both the α -Fe and γ -Fe lattice parameter, elastic constants, and several point-defects. This is not only an improve-

ment on the EAM potentials, but also on some alternative MEAM potentials [6, 9] that describe the formation energies of interstitials [6] and vacancies [9] less well. Results demonstrating the effectiveness of the new potential are presented in Section 3.3. The ability to predict lattice properties for both α -Fe and γ -Fe lattices is particularly useful in modelling transformations and processes in steel, where processes may take place in both crystal structures.

In Section 3.2 the experimentally measured data selected for the fit, in particular the elastic parameters for austenite, and the fitting procedure for the potential are described. In Section 3.3 the results of the potential are compared to several other potentials and its performance is discussed. Finally, in Section 3.4 the potential parameters are given.

3.2. FITTING PROCEDURE

3.2.1. RF-MEAM FORMALISM

THE RF-MEAM formalism in this work follows the form used by Duff et al. [17]¹. The total energy function for a system of N atoms of type ζ is given as

$$E_{\text{tot}} = \sum_{i=1}^N E_{\zeta_i}^{\text{emb}}(\rho_i) + \frac{1}{2} \sum_{i \neq j}^N \phi_{\zeta_i, \zeta_j}(r_{ij}). \quad (3.1)$$

Here $\phi_{\zeta_i, \zeta_j}(r_{ij})$ is the pair-potential between atoms i and j , separated by a distance r_{ij} . $E_{\zeta_i}^{\text{emb}}(\rho_i)$ is the embedding energy function given as,

$$E_{\zeta}^{\text{emb}}(\rho) = a_{\zeta} \rho^{\frac{1}{2}} + b_{\zeta} \rho^2 + c_{\zeta} \rho^3 + d_{\zeta} \rho^4. \quad (3.2)$$

where a quartic term was included to accommodate the starting potential from Ackland. ρ_i is the fictitious local electron density at site i ,

$$\rho_i = \frac{2\rho_i^{(0)}}{1 + e^{-T_i}}, \quad (3.3)$$

$$T_i = \sum_{l=1}^3 t_i^{(l)} \left(\frac{\rho_i^{(l)}}{\rho_i^{(0)}} \right)^2. \quad (3.4)$$

The density term $\rho_i^{(0)}$ is the spherical term present in EAM, the terms $\rho_i^{(l)}$ where $l = 1, 2, 3$ are the angular terms which are added in the MEAM formalism. When $t_i^{(l)} = 0$ a standard EAM potential is obtained.

$$\rho_i^{(0)} = \sum_{j \neq i}^N f_{\zeta_j}^{(0)}(r_{ij}), \quad (3.5)$$

$$\left(\rho_i^{(l)} \right)^2 = \sum_{j, k \neq i}^N f_{\zeta_j}^{(l)}(r_{ij}) f_{\zeta_k}^{(l)}(r_{ik}) P^{(l)}(\cos \theta_{jik}). \quad (3.6)$$

¹Part of this is also presented in Chapter 1.

Where $f_{\zeta_i}^{(l>0)}$ are partial electron density contributions, and $P^{(l)}(x)$ are Legendre polynomials, given by Rodrigues' formula $P^{(l)}(x) = \frac{1}{2^l l!} \frac{d^l}{dx^l} (x^2 - 1)^l$.

The (partial) electron density and pair-potentials are sums of cubic splines:

$$f_{\zeta_j}^{(l)}(r) = \sum_{n=1}^m a_{\zeta_i}^{(n,l)} \left(r_{\zeta_i}^{(n,l)} - r \right)^3 H \left(r_{\zeta_i}^{(n,l)} - r \right). \quad (3.7)$$

$$\phi_{\zeta_i, \zeta_j}^{(l)}(r) = \sum_{n=1}^k b_{\zeta_i, \zeta_j}^{(n)} \left(s_{\zeta_i, \zeta_j}^{(n)} - r \right)^3 H \left(s_{\zeta_i, \zeta_j}^{(n)} - r \right). \quad (3.8)$$

Where $H(r)$ is the Heaviside function. In the fitting procedure $a_{\zeta_i}^{(n,l)}$, $r_{\zeta_i}^{(n,l)}$, $b_{\zeta_i, \zeta_j}^{(n)}$, $s_{\zeta_i, \zeta_j}^{(n)}$, $t_i^{(l)}$, a_ζ , b_ζ , c_ζ , and d_ζ are the parameters to be optimised. In contrast to the MEAM formalism the pair-potential is not tied to the reference structure via the Rose EoS. All fitting in this work was done using *MEAMfit v2* [17]; the values of the parameters are given in Section 3.4.

The pair potential as in Eq. (3.8) is valid above a cut-off distance (here 1.2 Å), below the cut-off distance the pair potential is divided into two parts. Below 0.9 Å the Biersack-Ziegler-Littmark [19] form is used. Between 0.9 Å and 1.2 Å an interpolation of the form $e^{(B_0 + B_1 r + B_2 r^2 + B_3 r^3)}$ is made by MEAMfit, with B_i values such that the function and its first derivative are continuous at 0.9 Å and 1.2 Å. The resulting interpolation function is reconstructed within the LAMMPS implementation for RF-MEAM [20].

3.2.2. METHODOLOGY

THE fitting of the RF-MEAM potential was performed using *MEAMfit v2* [17]. The starting point in this work is the EAM potential by Ackland et al. [2], this potential uses cubic splines as in MEAMfit. Since the Ackland potential is effectively an initial guess for the RF-MEAM potential it is important to establish where the prior potential performs well and also where room for improvement exists. The lattice constant for α -Fe is predicted well by the Ackland potential as are point-defects; changes must not infringe upon the qualities of the existing potential. For γ -Fe several changes need to be made, most notably to the elastic constants and lattice parameter. The chosen fit-data is discussed in Sections 3.2.3-3.2.6. as well as the detailed work-flow.

The strategy used in this work is as follows:

1. First the lattice parameter, cohesive energy, and bulk modulus are fitted for perfect α -Fe, γ -Fe, and ϵ -Fe lattices. Here the angular terms do not contribute, so they are not included in the fit yet.
2. Next, the elastic parameters are fitted against data of strained lattices, at this point the angular terms become relevant and are included in the fitting procedure from this stage onward. Note the EAM portion of the potential are still included as optimisation parameters in the fitting procedure.
3. Once the lattice and elastic parameters are fitted, point-defect energies are included, see Section 3.2.5. At this stage inter-atomic forces are relevant, these forces ensure that the crystal remains stable when a point-defect is present. Reference

data for forces are obtained from *Vienna Ab-initio Simulation Package* [21–25] (VASP 5.3.5) simulations.

4. Once the lattice parameters, cohesive energies, elastic constants, and point-defects are reproduced satisfactorily the potential can be used in LAMMPS [20] to verify the potential's performance in MD simulations.

The weighting of various fitting targets is chosen such that all the energies, forces, and stresses are equally weighted. This weighting is entered in the fit database used by *MEAMfit v2* [17]. It is important to notice that each supercell returns one energy, six stress values, and for each atom in the supercell three forces. During the optimisation some weights are adjusted to correct for poorly fitted quantities, this is repeated until the resulting fit is satisfactory. *MEAMfit v2* uses a Normalised Weighted RMSE for the optimisation function.

A notorious issue with iron, and other ferromagnetic (FM) systems, is the role of magnetisation. Magnetic ordering plays a key role in the bcc-fcc transition in iron [26]. An in depth study to incorporate magnetisation into an interatomic potential was conducted by Dudarev and Derlet [27]. The potential in that work was fitted to the magnetic ground states for both α -Fe and γ -Fe. Magnetic contributions at finite temperatures are not explicitly included in the potential fitted in this work.

3.2.3. ELASTIC CONSTANTS FOR γ -Fe

THE elastic constants for γ -Fe are experimentally determined at high-temperatures or in stabilised alloys. However, the RF-MEAM potential fitted in this work is fitted to static data, so data at 0 K is needed. In Table 3.1 it can be seen that DFT calculations at high temperature contradict experimental data. Therefore, instead of using DFT, another approach is chosen to approximate the required data using experimental data. In this work an extrapolation was performed using the experimental data of Neuhaus et al. [18], as their data follows the expectations in [28] best where it is assumed that the elastic parameters for γ -Fe will not differ greatly from those of α -Fe. The data points were used for extrapolation using Eq.(3.9) which follows the experimental data for several metals, but most importantly for α -Fe as shown by Varshni [29].

$$C_{ij} = a - \frac{bT^2}{T + c}. \quad (3.9)$$

As there are just two datapoints Eq. (3.9) cannot be used as-is, hence it was assumed that $\partial C_{ij}/\partial T = k$, where $k = \Delta C_{ij}/\Delta T$ is constant, i.e., $c = 0$. Such a linear fit is also performed for the bulk modulus and shear modulus in the work by Lindgren and Gyhlesten Back for pure iron, cf. [30]. A linear fit will produce a value for C_{ij} that is likely too large. Varshni also introduced an asymptotic approximation to Eq. (3.9) [29]:

$$C_{ij} = a - bT^2. \quad (3.10)$$

Effectively the extrapolations with Eqs. (3.9) and (3.10) yield an upper and a lower value to the elastic constants. In Table I the results as well as the experimental values from [18] are given. One expects $dC_{ij}/dT|_{T=0} = 0$ as there is little expansion near absolute zero,

therefore Eq. (3.10) provides a more physically consistent temperature dependence than the linear approximation.

As the value for C_{12} is not explicitly given in [18] but rather $C' = (C_{11} - C_{12})/2$, an additional datapoint is entered, $C' = 0$ at 823 K [31, 32], as this is roughly where the martensitic transformation would occur. Where it is assumed that the martensitic transformation is caused by mechanic instability of the γ -Fe lattice, which is why $C_{11} < C_{12}$ at low temperatures. Here it is used that the paramagnetic γ -Fe phase is unstable at low temperatures. Finally the assumption that $B = (C_{11} + 2C_{12})/3 \approx 204$ GPa at 298 K (from [28]) is included, here C_{11} and C_{12} are solved simultaneously for Eq. (3.10) using a least-squares minimisation. Additionally the data is compared to a theoretical calculation based on calculated (ab initio) lattice parameters [33].

Temperature [K]	Ref.	C_{11} [GPa]	C_{12} [GPa]	C_{44} [GPa]	B [GPa]	Input
Experimental						
1200	[18]	188	156	87	167	
1573	[18]	171	135	68	147	
1428	[34]	154	122	77	133	
1428	[35]	181	156	83	164	
1428	[36]	154	144	78	147	
298	[28]				204	
0	us	212	185	114	194	Eq. (3.10), [18]
0	us	243	224	148	230	Eq. (3.9), [18]
0 [†]	us	198	207	114	204	Eq. (3.10), [18, 34–36] $C' = 0$ at 823 K
Theoretical						
1200	[33]	149	92	135	111	
1300	[33]	145	92	131	110	
1400	[33]	141	91	127	108	
1500	[33]	137	90	123	106	
1600	[33]	132	89	118	103	
1428	[37]	136	88	124	104	
0	[38]	182	126	129	144	
0	us	171	98	157	122	Eq. (3.10), [33]
0	us	200	106	186	137	Eq. (3.9), [33]

Table 3.1: Data for the elastic constants and bulk modulus for γ -Fe, measurement uncertainties are left out. The last row (†) fitted to experimental data was used in the potential fitting procedure. Extrapolations using Eq. (3.9) are performed assuming $c = 0$ as described above.

The extrapolation with Eq.(3.10) using the experimental values from [18, 34–36] performs best with the assumption that $C' = 0$ at 823 K, and the prediction of Ghosh and Olson [28] that $B = 204$ GPa at 298 K. The results can be seen in Figure 3.1. Furthermore, the temperature dependence of the elastic constants is similar to α -Fe as suggested in [28]. The potential is therefore fitted to $B = 204$ GPa, $C_{11} = 198$ GPa, $C_{12} = 207$ GPa, and $C_{44} = 114$ GPa.

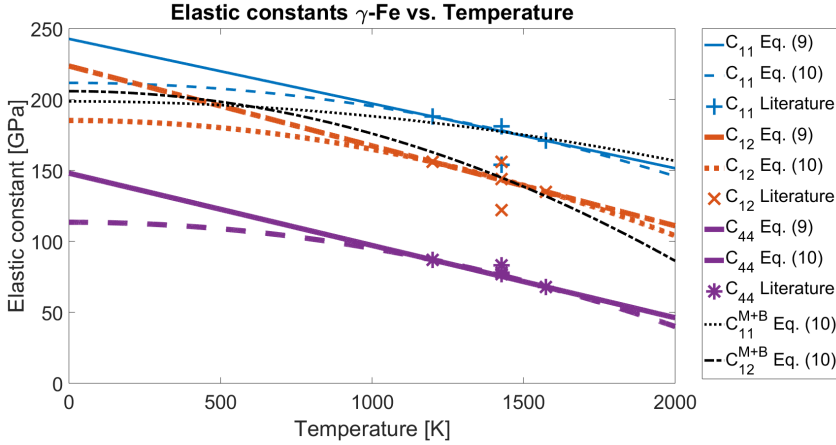


Figure 3.1: Results for extrapolating the elastic constants for γ -Fe from [18], as well as the data from [34–36]. The narrow solid line and dashed line (blue) and the ‘+’ symbols are the linear, quadratic and literature values for C_{11} respectively. The thick dash-dotted line and dotted line (red) and the ‘x’ symbols are the linear, quadratic and literature values for C_{12} resp., and the narrow dotted line and dash-dotted line (black) are the quadratic extrapolation for C_{11} and C_{12} using that $C' = 0$ at 823 K and $B = 204$ GPa at 0 K respectively. The thick solid line and dashed line (purple) and the ‘*’ symbols are the linear, quadratic and literature values for C_{44} respectively.

3.2.4. CRYSTAL STRUCTURE AND ELASTIC CONSTANTS

FIRST the non-angular contributions of the (fictitious) electron-density are optimised, i.e., the EAM portion of the potential where the angular terms are set to 0, i.e., $t_i^{(l)} = 0$ for $l = 1, 2, 3$ as in Eq. (3.4), as well as the pair-potential terms. Fitting is performed on multiple defect free α -Fe lattices with varying lattice parameters. The lattice parameter is varied around the experimental value $a = 2.8605\text{\AA} (\pm 3\%)$ [39, 40], in [40] this value is found by extrapolation to 0 K using thermal expansion [41] with the data of [42]. The cohesive energy is set to $E_{coh} = -4.28$ eV/atom [3, 43]. For the lattice parameters near the equilibrium value the energy is calculated using VASP 5.3.5 (PAW-PBE) to establish the shape of the potential. Note that the PAW-PBE lattice parameter is significantly smaller than the experimental value, therefore the VASP lattice parameters were shifted as detailed in Table 3.2.

After the perfect lattice data (for bcc, fcc, and hcp) is fitted, stresses are included. For α -Fe the elastic constants used are $C_{11} = 243$ GPa, $C_{12} = 138$ GPa, and $C_{44} = 122$ GPa [42]. The elastic constants are determined at 4.2 K, here we assume that the temperature dependence near 0 K is negligible as changes are minimal at low temperatures [42].

The same approach is taken regarding the γ -Fe lattice. The target lattice parameter is $a = 3.562$ Å [39], this value was extrapolated from high temperature measurements and verified using FeNiMn alloys. The energy difference at 0 K is $\Delta E_{bcc \rightarrow fcc} = 0.06$ eV derived by thermodynamic assessment [44]. Ab initio studies suggest a value of 0.1 eV [45, 46] for AFM α -Fe at 0 K. Elastic parameters were extrapolated from high temperature measurements as part of this work as detailed in Section 3.2.3. The potential is fitted to $B = 204$ GPa, $C_{11} = 198$ GPa, $C_{12} = 207$ GPa, and $C_{44} = 114$ GPa.

VASP lattice [Å]	Rescaled lattice [Å]	VASP energy [eV/atom]	Rescaled energy [eV/atom]
2.1645	2.2500	0.9236	0.4812
2.7163	2.8000	-8.0934	-4.2164
2.7406	2.8250	-8.1691	-4.2558
2.7648	2.8500	-8.2059	-4.2749
2.7750	2.8605	-8.2156	-4.2800
2.7891	2.8750	-8.2021	-4.2730
2.8133	2.9000	-8.1980	-4.2709

Table 3.2: VASP data and the rescaled values used for fitting defect free α -Fe lattices.

An additional data point is a ϵ -Fe lattice, where $a = 2.523$ Å, $c/a = 1.603$ [47], the experimental data holds for room-temperature (296 ± 3 K). The values at zero pressure are extrapolations of an empirical function derived in [47]. For the cohesive energy $\Delta E_{bcc \rightarrow hcp} = 0.082$ eV from ab initio calculations [45] was used as there is no direct experimental data available. The cohesive energy of ϵ -Fe is similar to that of γ -Fe or lower as found by some studies [3, 45].

3.2.5. POINT DEFECTS

ESPECIALLY for (relaxed) point defects the RF-MEAM potential improves on the starting (EAM) potential by adding in angular dependencies for the local density function. Using the perfect lattices for α -Fe and γ -Fe using the target lattice parameters as in Section 3.2.4. several point defects are constructed. For α -Fe: a vacancy; a vacancy cluster of first-nearest neighbours (1NN), and second-nearest neighbours (2NN); common interstitials, $\langle 100 \rangle$, $\langle 110 \rangle$, $\langle 111 \rangle$ dumbbells, tetrahedral (TET) and octahedral (OCT). For defects in γ -Fe only a vacancy was included, as there are few experimentally known defect energies and DFT calculations for γ -Fe give results that differ from known experimental values. All the used target values, and their respective sources, are presented in Tables 3.3, 3.4, 3.5, 3.6.

VACANCIES

A notable change to most existing potentials is the vacancy formation energy in α -Fe. Following the work of Glensk et al. [48] it is assumed that previous methods to estimate the vacancy formation energy have systematically given a value that is too low. Therefore values taken from DFT calculations were used. For the vacancy in γ -Fe a DFT value is used for anti-ferromagnetic ordering as it is found that this is the most stable ordering [49]. For the bi-vacancy clusters in α -Fe the binding energies were taken from the detailed work of Domain et al. [50]. In this work the indirect binding energy for cells with 128-2 atoms at constant volume was used, as the vacancy clusters are modelled for large lattices at equilibrium.

INTERSTITIALS

In literature various values for interstitial energies, particularly for dumbbells, are presented. In this work the data by Marinica et al. [48] were used, as it confirms earlier

data [2, 50–52]. Moreover, the various energies in the references show the same general order from most to least stable interstitial. In [53] the $\langle 100 \rangle$ dumbbell is unstable and relaxes to an octahedral site so no value was provided. Other studies, [2, 50–52], show that the formation energy is similar to, or as Marinica suggests higher than that of the octahedral site.

The pair-potential part of the Ackland potential uses a short range cut-off radius of 2.05 Å, this is too large for (unrelaxed) interstitials. Unrelaxed interstitials are included to provide data for interatomic forces, so the cut-off radius must be chosen accordingly. In order to accommodate for this the short range cut-off has been set to 1.2 Å.

3.2.6. STACKING FAULTS AND FREE SURFACES

STABLE stacking fault (USF) energies and free surface (FS) energies are not used in the fit, however the performance of the potential presented in this work has been tested for several USF's and FS's. The reference data is mainly taken from DFT calculations. For α -Fe data is available from an experimental study [54], which has been included in Table 3.6. The theoretical data presented for γ -Fe FS's and for α -Fe USF's is taken directly from DFT calculations.

Orientation relations (OR) between α -Fe and γ -Fe like Nishiyama-Wasserman (NW) and Kurdjumov-Sachs (KS) are also tested, but not fitted to. For the OR's reference data is taken from DFT calculations [55, 56].

3.3. VALIDATION OF THE POTENTIAL AND DISCUSSION

3.3.1. STRUCTURAL PROPERTIES

PHYSICAL properties, as calculated with the RF-MEAM potential presented in this work using LAMMPS [20], are presented in Tables 3.3, 3.4, 3.5, 3.6. The new potential is compared to several other potentials, notably the Ackland potential [2] on which it is built, labelled *Ack04*, the MEAM potential by (B.-J.) Lee et al. [6] (*BJLee*), a second MEAM potential by (T.) Lee et al. [9] (*TLee*). Also added in the comparison are an Analytical Bond-Order Potential by Müller et al. [3] (*Mül07*), another EAM potential by Mendelev et al. [5] (*Mend03*), and finally a recent Angular-Dependent Potential (ADP) by Starikov et al. [57] (*Stari21*). Reference data is provided from various sources. Where possible, experimental data is provided otherwise a theoretical value is used.

The performance of the various listed potentials was checked using LAMMPS. The lattice parameter is determined by isotropic relaxation of the volume of a perfect lattice. For defects, and stacking faults the supercell was relaxed at constant volume. For the free surfaces the surface direction is allowed to expand to allow for relaxation. Except for the free surfaces periodic boundary conditions are used. The stopping criteria are set such that the energy change between iterations is $1 \cdot 10^{-8}$ eV, for forces the 2-norm of the global force vector must be less than $1 \cdot 10^{-8}$ eV/Å. All supercells were constructed using Atomsk [58]. Defect formation energies and surface energies are calculated from the excess energy using the cohesive energy for the relevant state. The total energy for a supercell containing N atoms in a perfect lattice is known, so the energy difference is caused by the introduced defect.

All point defects in α -Fe were simulated in a 1024 atom cubic cell of $8 \times 8 \times 8$ unit

cells. For γ -Fe a cubic cell containing 864 atoms, i.e., $6 \times 6 \times 6$ unit cells was used. The free surfaces have been simulated in a $6 \times 6 \times 6$ unit cell system with periodic boundaries in two directions for both α -Fe and γ -Fe, leaving two 6×6 unit cell free surfaces. For the $6 \times 6 \times 6$ unit cell the separation of the two free surfaces is more than three times the maximum cut-off radius used in the potential. The free surfaces were also simulated for a smaller supercell, where the difference in free surface energy with a $4 \times 4 \times 4$ unit cell is in the order of 0.01 J/m^2 . Finally the unstable stacking faults had an area of 6×6 unit cells, and the cell length perpendicular to the stacking fault is 16 unit cells, i.e., 8 unit cells between stacking faults, here periodic boundaries were used. The separation of the stacking fault interfaces is more than four times the maximum cut-off radius used in the potential.

The lattice parameters and elastic constants found for the RF-MEAM potential reproduce the experimental values for both α -Fe at 0 K and our extrapolated experimental elastic parameters for γ -Fe at 0K. This in contrast to most other potentials as shown in Tables 3.3 and 3.4, except for the potential by T. Lee et al. [9]. In general the γ -Fe lattice parameter is overestimated, except for *Stari21* which was fitted to DFT data. For *Stari21* the $a_{fcc,0K} : a_{bcc,0K}$ ratio agrees with the experimental ratio. However the elastic parameters for *Stari21* are slightly off for α -Fe. The RF-MEAM potential is among the potentials (*BJLee*, and *Stari21*) that find a high bulk modulus for γ -Fe, as was predicted by Ghosh and Olson [28].

3.3.2. POINT DEFECTS

FOR point defects there are greater differences between the various potentials. *TLee* shows values for vacancy clusters in α -Fe, vacancy migration energies which are too low. *Stari21* performs better, however the interstitial formation energies are relatively high. This makes the current RF-MEAM potential more suitable for modelling and simulating defects, most notably vacancy (migration) in α -Fe and γ -Fe than *TLee*. Note that the RF-MEAM potential performs best when combining vacancies and interstitials in a single system, as some other potentials perform well for specific types of point defects. The nearest-neighbour vacancy migration path is presented in Figure 3.2, note the unphysical behaviour observed for the *TLee* potential.

3.3.3. SURFACES AND STACKING FAULTS

THE surface energies and unstable stacking faults which were not part of the fitting procedure, however they are reproduced well for the RF-MEAM potential, Table V. Note, there exist relatively large differences between the various potentials and even some literature sources. Here it is seen that, except for *BJLee* and *Stari21*, other potentials underestimate surface and USF energies. *Stari21* on the other hand finds relatively high energies.

Lastly the NW and KS-OR are evaluated with the new potential. The energies for both OR predicted by the RF-MEAM potential agree with literature [55, 56]. The lattice ratios for α -Fe and γ -Fe follow the experimental data from [39]. This is contrasted by *Mend03* and *Stari21*, which both find very high interface energies for the fcc-bcc OR's. These are valuable characteristics of the RF-MEAM potential when applied to interphase modelling. Hence the RF-MEAM potential is well-suited for static interphase modelling.

	DFT	Exp.	<i>Ack04</i> [2]	<i>Mül-07</i> [3]	<i>Mend-03</i> [5]	<i>BJLee</i> [6]	<i>TLee</i> [9]	<i>Stari-21</i> [57]	RF-MEAM
Lattice properties for various crystal structures, at 0 K									
a_{fcc} [Å]	3.482 [3]	3.562 [39]	3.658	3.611	3.658	3.611	3.589	3.523	3.562
$\Delta E_{bcc \rightarrow fcc}$ [eV]	0.11[3] 0.101 [45] 0.06[46]		0.139	0.030	0.121	0.048	0.009	0.092	0.085
a_{bcc} [Å]	2.832 [3]	2.8605 [39, 40]	2.855	2.860	2.855	2.864	2.851	2.830	2.8604
$\Delta E_{coh,bcc}$ [eV/atom]	-4.28 [3]	-4.28 [43]	-4.013	-4.28	-4.127	-4.29	-4.28	-4.376	-4.281
a_{hcp} [Å]	2.459 [3]	2.523 [47] ⁱ	2.605	2.555	2.607	2.563	2.534	2.502	2.515
c_{hcp}/a_{hcp}	1.58 [3]	1.603 [47] ⁱ	1.600	1.630	1.595	1.614	1.640	1.676	1.640
$\Delta E_{bcc \rightarrow hcp}$ [eV]	0.06[3] 0.082 [45]		0.116	0.027	0.117	0.030	0.015	0.126	0.101
Fcc/bcc ratio inter-atom distances relevant for the KS and NW-OR									
[fcc]//[bcc] at 0 K									
$[\bar{1}10]//[\bar{1}11]$ KS-OR	1.004 [3]	1.017 [39]	1.046	1.031	1.046	1.030	1.028	1.016	1.017
$[\bar{1}10]//[\bar{1}11]$ NW-OR	0.869 [3]	0.881 [39]	0.906	0.893	0.906	0.892	0.890	0.880	0.881
$[\bar{1}10]//[\bar{1}11]$ NW-OR	1.065 [3]	1.079 [39]	1.110	1.093	1.110	1.092	1.090	1.078	1.079
[fcc]//[bcc] at 1100 K									
$[\bar{1}10]//[\bar{1}11]$ KS-OR		1.025 [39]	1.040	1.037	1.040	1.035	1.027	1.013	1.035
$[\bar{1}10]//[\bar{1}11]$ NW-OR		0.888 [39]	0.901	0.898	0.901	0.897	0.889	0.878	0.896
$[\bar{1}10]//[\bar{1}11]$ NW-OR		1.087 [39]	1.103	1.100	1.103	1.098	1.089	1.075	1.098
T_{melt} [K]		1811 [59]	1796	2270	1772	2200	>1900		>1950

Table 3.3: A comparison between various potentials and experimental or DFT data. Bold values are used to fit the RF-MEAM potential to.

ⁱ The lattice parameter for ϵ -Fe holds for a temperature of 296 ± 3 K.

Finally for the common $\{110\}$ -plane and $\{112\}$ -plane general stacking faults (GSF) in bcc, when shifting in the $\langle 111 \rangle$ -direction are simulated. The supercell used is $6 \times 6 \times 16$ bcc unit cells in size with periodic boundary conditions. The stopping criteria are the same as for other simulations. The stacking fault is simulated by incrementally moving

			<i>Ack04</i> [2]	<i>Mül-07</i> [3]	<i>Mend-03</i> [5]	<i>BJLee</i> [6]	<i>TLee</i> [9]	<i>Stari-21</i> [57]	RF- MEAM
Elastic parameters [GPa] 0 K									
	DFT [3]	Exp. [42]							
C_{11}^{bcc}	277	243	243	225	243	243	228	250	243
C_{12}^{bcc}	147	138	145	142	145	138	135	108	142
C_{44}^{bcc}	96	122	116	126	116	122	118	110	117
B^{bcc}	190	173	178	169	178	173	166	155	175
	Extrap.	Exp. [18]							
C_{11}^{fcc}	198	188 ⁱ	102	204	67	204	192	201	215
C_{12}^{fcc}	207	156 ⁱ	91	144	40	171	148	173	175
C_{44}^{fcc}	114	87 ⁱ	55	101	10	86	80	55	151
B^{fcc}	204	167 ⁱ	95	164	49	182	163	183	188

Table 3.4: Comparison between potentials for the elastic parameters of α -Fe and γ -Fe, fit-targets are bold.
ⁱ The experimental data for γ -Fe is measured at 1200 K.

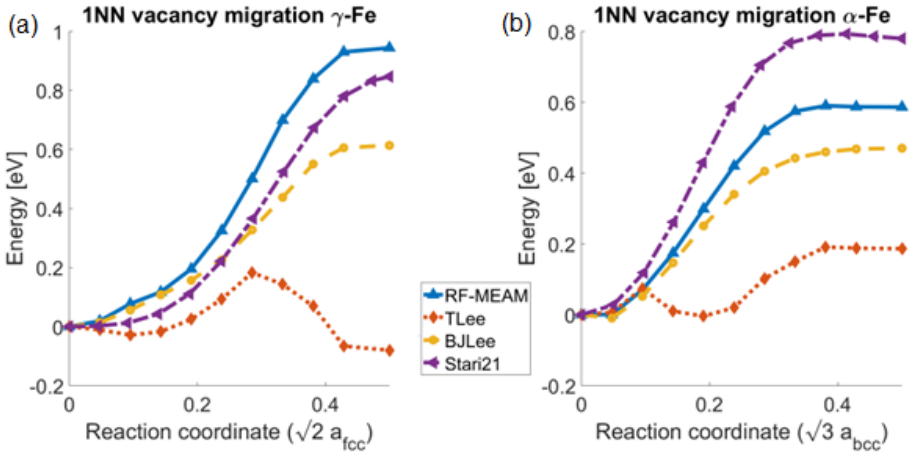


Figure 3.2: Vacancy migration energy for first nearest-neighbour atom in γ -Fe (a), and α -Fe (b) calculated using the Nudged-Elastic Band (NEB) method. The position of the moving atom is given between 0 and 0.5, where 0 is a vacancy in an otherwise perfect lattice and 0.5 is the halfway point between the vacancy and the original lattice site. The solid line corresponds to the potential presented in this work, the dotted line for *TLee*, the dashed line is for *BJLee*, and the dash-dotted line belongs to *Stari21*.

one half of the supercell with respect to the other along the $\langle 111 \rangle$ -direction. Relaxation of atoms is only allowed perpendicular to the stacking fault plane, as in [57, 70]. In Figure 3.3 the RF-MEAM potential is compared to *BJLee*, *TLee*, and *Stari21*. The GSF energies for both planes are similar for the four tested potentials, only *Stari21* produces higher values. The higher values correspond to DFT results [70], to which *Stari21* was originally fitted.

			Ack04 [2]	Mül- 07 [3]	Mend- 03 [5]	BJLee [6]	TLee [9]	Stari- 21 [57]	RF- MEAM
Point defect energies [eV] at 0 K									
	DFT	Exp.							
$E_{vac,bcc}^f$	2.2 [60] 2.47 [48, 62]	1.40[61] 1.59-1.89 [59]	1.72	1.56	1.71	1.77	1.68	2.05	1.99
$E_{vac,bcc}^m$	0.7[60]	0.55[59]- 0.85[63]	0.57	0.57	0.47	0.47	0.19	0.79	0.59
$E_{vac,fcc}^f$	1.82- 2.27 [49]	1.40[63]- 1.71[61]	1.77	1.92	1.75	1.92	2.67	1.97	1.93
$E_{vac,fcc}^m$		1.55[63] 0.75-1.2 [64] ⁱ	0.45	0.32		0.57	0.20	0.85	0.94
$E_{1NN,vac,bcc}^b$	0.15 [50]		0.15	0.20		0.00	-0.60	0.09	0.18
$E_{2NN,vac,bcc}^b$	0.29 [50]		0.26	0.13		0.25	0.07	0.20	0.26
$E_{SIA\langle 100 \rangle,bcc}^f$	4.64[65]			4.59	4.02	6.23	4.54	5.00	4.42
$E_{SIA\langle 110 \rangle,bcc}^f$	3.52 [53] 3.64[65]		3.59	4.19	3.52	4.90	3.67	4.25	4.04
$E_{SIA\langle 111 \rangle,bcc}^f$	3.94 [53] 4.34[65]			5.51	4.33	5.02	4.04	4.79	4.19
$E_{SIA\langle TET \rangle,bcc}^f$	4.13 [53]				4.16	5.53	3.98	4.59	4.46
$E_{SIA\langle OCT \rangle,bcc}^f$	4.16 [53]		4.22		4.19	6.40	4.42	- ⁱⁱ	4.40

Table 3.5: Comparison between potentials for energies associated with point defects. Bold values were used as target values in the fit. Various energies are listed as: formation energies E^f , migration energies E^m , and binding energies E^b are included.

ⁱ This value is derived from the activation energy presented in [64] of 3.02 eV/atom, where the author of this work has subtracted the vacancy formation energies from [49].

ⁱⁱ Unstable, collapses to $\langle 110 \rangle$.

3.3.4. THERMAL EXPANSION

FOR thermal expansion four perfect lattices ($5 \times 5 \times 5$ unit cells) with different lattice parameters are heated using the NVT ensemble setting in LAMMPS. The cell is simulated for 2.5 ns, such that the equilibrium pressure can be determined. The equilibrium lattice parameter is determined by using that $P = -dE/dV$. A linear fit to the equilibrium pressure with respect to volume is made, for the equilibrium lattice parameter $P(V) = 0$.

At 300 K (room temperature) the calculated lattice parameter in α -Fe is 2.864 Å, and at 1100 K the α -Fe lattice parameter is predicted to be 2.886 Å, which is in agreement with the results from Acet [39]. Moreover the expansion in the temperature range 800K to 1300K, shown in Figure 3.4, follows the values presented in [39].

The thermal expansion of the RF-MEAM potential differs from other potentials. For α -Fe the growth is repressed particularly for temperatures below 700 K, and for γ -Fe

			<i>Ack04</i> [2]	<i>Mül-07</i> [3]	<i>Mend-03</i> [5]	<i>BJLee</i> [6]	<i>TLee</i> [9]	<i>Stari-21</i> [57]	RF- MEAM
Free surfaces [J/m ²] 0 K									
	DFT	Exp.							
$E_{100,bcc}$	2.29[66] 2.32[67]	2.40[54] ⁱ	1.75	1.67	1.78	2.49	1.49	2.63	2.02
$E_{110,bcc}$	2.27[66] 2.19[67]	2.40[54] ⁱ	1.62	1.36	1.65	2.36	1.60	2.42	1.91
$E_{111,bcc}$	2.52[66] 2.36[67]	2.40[54] ⁱ	1.96	1.84	2.00	2.58	1.62	2.77	2.28
$E_{211,bcc}$		2.40[54] ⁱ	1.85	1.67	1.89	2.47	2.38	2.65	2.15
$E_{100,fcc}$	2.13[68] 2.15[68]		1.64	1.65	1.57	2.40	1.59	2.57	1.98
$E_{110,fcc}$	2.26[68] 2.27[68]		1.77	1.84	1.71	2.40	1.85	2.65	2.11
$E_{111,fcc}$	2.08[68] 2.11[68]		1.58	1.39	1.44	2.18	1.64	1.68	1.81
Unstable stacking faults [J/m ²] in bcc									
(001)/[$\frac{1}{2}$ 00]	1.79[69] 1.86[69]		1.89	2.15	1.85	2.26	2.01	2.28	2.31
(011)/[$\frac{1}{2}$ 00]	1.40[69] 1.43[69]		1.78	1.93	1.75	2.01	1.39	1.78	1.87
(011)/[$\frac{1}{2}$ $\frac{1}{4}$ 0]	0.47[69] 0.59[69]		-	0.90	0.66	-	-	-	0.63
KS and NW-OR [J/m ²] at 0 K									
E_{KS}	0.41[55] 0.27[56]				0.920	0.312	0.363	1.805	0.326
E_{NW}	0.32[56]				0.778	0.254	0.341	1.536	0.257

Table 3.6: Several free surfaces and unstable stacking fault energies are presented, as are the KS and NW OR interface energies. None of the values were used as targets in the fitting procedure.

ⁱ The experimental surface energies from [54] are taken for a polycrystalline surface.

the lattice is not stable at low temperatures. This instability needs to be taken into account when using the potential in finite temperature simulations for γ -Fe. The instability makes it difficult to accurately determine the lattice parameter at 700 K, so there is a jump in Figure 3.4.

Most other potentials show only linear growth for the γ -Fe lattice parameter, however this is not physical. At low temperatures the thermal expansion should be small and gradually increase to a linear growth as is seen for the literature data. The RF-MEAM potential and *Stari21* display this for both α -Fe and γ -Fe, where *TLee* only has linear expansion. A peculiarity of *Stari21* is that at room temperature the equilibrium lattice parameter has decreased which is unphysical behaviour.

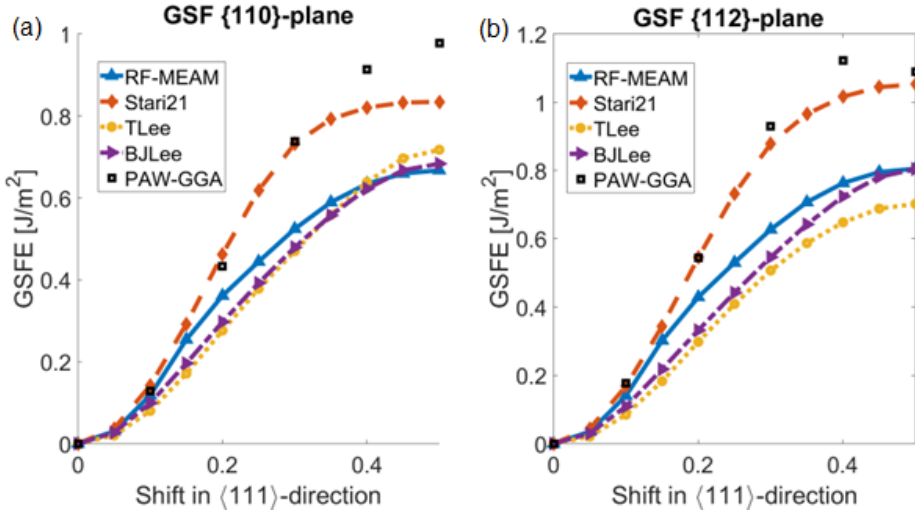


Figure 3.3: GSFE for the {110} and {112}-planes. A shift is introduced in the <111>-direction the solid lines belong to the RF-MEAM potential, the dashed lines to *Stari21*, the dotted lines to *TLee*, and the dash-dotted lines to *BJLee*. The black squares are DFT results using PAW-GGA taken from [70]. The outlier here is *Stari21* which produces a consistently high surface and USF energy too.

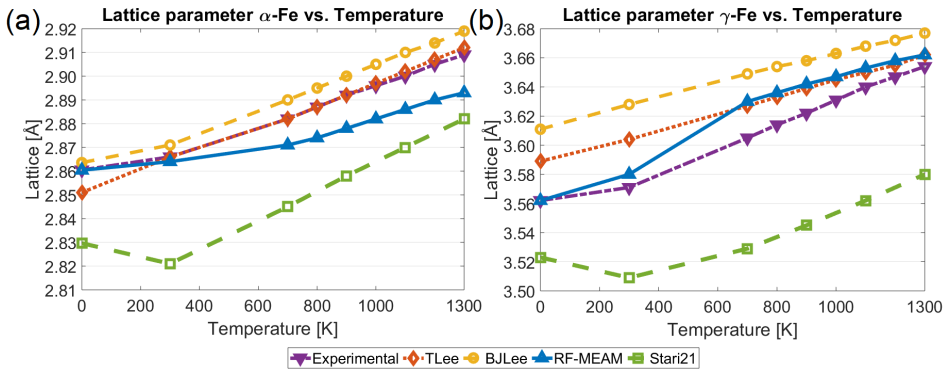


Figure 3.4: Dependence of the α -Fe (a) and γ -Fe (b) lattice constants on the temperature. In the dash-dotted line the experimental data from Acet et al. [39] is presented, we compare the results of *BJLee* (dashed line, circle markers), *TLee* (dotted line), *Stari21* (dashed line, square markers), and the RF-MEAM potential (solid line) presented in this work.

3.3.5. DISCUSSION

MOST Fe-potentials are constructed with specific targets in mind; The *TLee* potential is made to model the bcc to fcc transition, but it fails when modelling vacancy structures. The ADP potential *Stari21* is made with dislocations and point defects in mind, but is not well-suited for surfaces and stacking faults, or the fcc-bcc interface. The RF-MEAM potential presented here was fitted to simulate experimental data where possible. However, this is challenging as a wealth of fitting data, such as atomic forces, are

available from DFT only. For the general structural data fitting to experimental data at 0 K was accomplished, however the elastic constants of γ -Fe at 0 K are fitted to extrapolated experimental data.

The new RF-MEAM potential can describe vacancy systems well, it also follows the free surface energies, and fcc-bcc OR energies. Hence, the RF-MEAM potential is most suitable when simulating vacancy systems and surfaces or stacking faults, and particularly the interphase relation between α -Fe and γ -Fe. It must be noted that static simulations here work better than finite temperature simulations as the thermal expansion of both phases is slightly off. In Figure 3.5, the specific strengths of the listed potentials in comparison to the RF-MEAM potential are visualised.

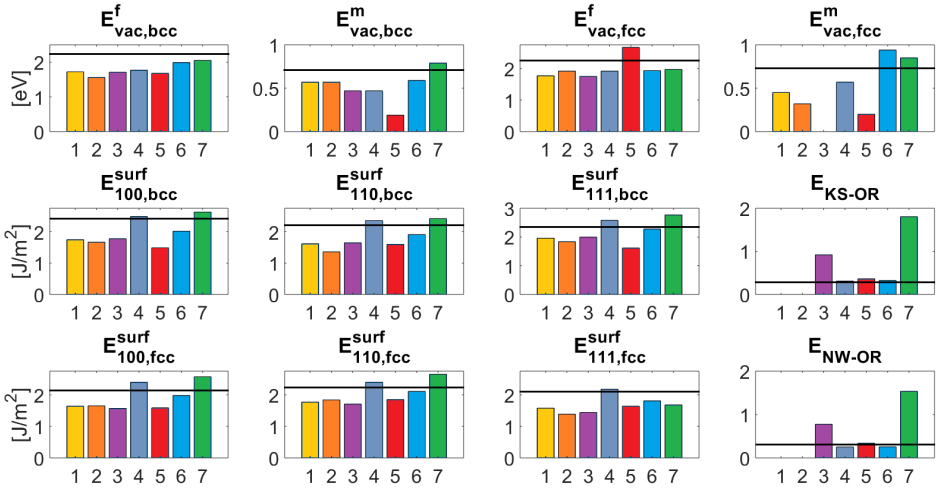


Figure 3.5: Visualisation of some of the strengths and weaknesses of various potentials as presented in Tables 3.5 and 3.6. Bar 1 corresponds to *Ack04*, then 2:*Mü07*, 3:*Mend03*, 4:*BJLee*, 5:*TLee*, 6:RF-MEAM, 7:*Stari21*. The black horizontal line corresponds to literature data, for vacancies the fitting targets are used. For the bcc free surface [67] is used, for fcc free surfaces [68], and for the OR's [56].

3.4. THE POTENTIAL

$(\chi = \text{Fe})$	Value	Unit	Cut-offs (\AA)
Embedding function			
a_{Fe}	- 1.000 000 0000	eV	
b_{Fe}	- 0.000 673 1412	eV	
c_{Fe}	0.000 000 0000	eV	
d_{Fe}	0.000 000 0765	eV	
Electron-density pre-factors			
$t_{\text{Fe}}^{(1)}$	0.007 220 8979		
$t_{\text{Fe}}^{(2)}$	0.000 679 3420		
$t_{\text{Fe}}^{(3)}$	0.000 000 0000		

Pairwise functions (ED)

$f_{\text{Fe}}^{(l=0)} \left(a_{\text{Fe}}^{(1,0)}, r_{\text{Fe}}^{(1,0)} \right)$	11.686 859 4080	0.0-2.4
$f_{\text{Fe}}^{(l=0)} \left(a_{\text{Fe}}^{(2,0)}, r_{\text{Fe}}^{(2,0)} \right)$	-0.554 710 7401	0.0-3.2
$f_{\text{Fe}}^{(l=0)} \left(a_{\text{Fe}}^{(3,0)}, r_{\text{Fe}}^{(3,0)} \right)$	0.506 935 2708	0.0-4.2
$f_{\text{Fe}}^{(l=1)} \left(a_{\text{Fe}}^{(1,1)}, r_{\text{Fe}}^{(1,1)} \right)$	-45.831 339 9973	0.0-2.5
$f_{\text{Fe}}^{(l=1)} \left(a_{\text{Fe}}^{(2,1)}, r_{\text{Fe}}^{(2,1)} \right)$	20.351 730 7168	0.0-3.2
$f_{\text{Fe}}^{(l=1)} \left(a_{\text{Fe}}^{(3,1)}, r_{\text{Fe}}^{(3,1)} \right)$	-7.732 949 7788	0.0-4.0
$f_{\text{Fe}}^{(l=1)} \left(a_{\text{Fe}}^{(4,1)}, r_{\text{Fe}}^{(4,1)} \right)$	1.258 181 8551	0.0-4.8
$f_{\text{Fe}}^{(l=2)} \left(a_{\text{Fe}}^{(1,2)}, r_{\text{Fe}}^{(1,2)} \right)$	148.513 244 8477	0.0-2.5
$f_{\text{Fe}}^{(l=2)} \left(a_{\text{Fe}}^{(2,2)}, r_{\text{Fe}}^{(2,2)} \right)$	-22.814 750 5687	0.0-3.2
$f_{\text{Fe}}^{(l=2)} \left(a_{\text{Fe}}^{(3,2)}, r_{\text{Fe}}^{(3,2)} \right)$	11.515 010 6233	0.0-4.0
$f_{\text{Fe}}^{(l=2)} \left(a_{\text{Fe}}^{(4,2)}, r_{\text{Fe}}^{(4,2)} \right)$	-2.026 949 8368	0.0-4.8
$f_{\text{Fe}}^{(l=3)} \left(a_{\text{Fe}}^{(1,3)}, r_{\text{Fe}}^{(1,3)} \right)$	2 600.091 135 3033	0.0-2.5
$f_{\text{Fe}}^{(l=3)} \left(a_{\text{Fe}}^{(2,3)}, r_{\text{Fe}}^{(2,3)} \right)$	73 863.832 500 2631	0.0-3.2
$f_{\text{Fe}}^{(l=3)} \left(a_{\text{Fe}}^{(3,3)}, r_{\text{Fe}}^{(3,3)} \right)$	46.883 735 1394	0.0-4.0
$f_{\text{Fe}}^{(l=3)} \left(a_{\text{Fe}}^{(4,3)}, r_{\text{Fe}}^{(4,3)} \right)$	21.185 129 1577	0.0-4.8

Pairwise functions (PP)

$\phi_{\text{Fe,Fe}} \left(b_{\text{Fe,Fe}}^{(1)}, s_{\text{Fe,Fe}}^{(1)} \right)$	-71.414 445 4775	eV	1.2-1.8
$\phi_{\text{Fe,Fe}} \left(b_{\text{Fe,Fe}}^{(2)}, s_{\text{Fe,Fe}}^{(2)} \right)$	104.948 192 6512	eV	1.2-1.95
$\phi_{\text{Fe,Fe}} \left(b_{\text{Fe,Fe}}^{(3)}, s_{\text{Fe,Fe}}^{(3)} \right)$	-87.705 791 6224	eV	1.2-2.2
$\phi_{\text{Fe,Fe}} \left(b_{\text{Fe,Fe}}^{(4)}, s_{\text{Fe,Fe}}^{(4)} \right)$	69.650 061 9465	eV	1.2-2.3
$\phi_{\text{Fe,Fe}} \left(b_{\text{Fe,Fe}}^{(5)}, s_{\text{Fe,Fe}}^{(5)} \right)$	-13.927 442 2124	eV	1.2-2.4
$\phi_{\text{Fe,Fe}} \left(b_{\text{Fe,Fe}}^{(6)}, s_{\text{Fe,Fe}}^{(6)} \right)$	1.192 148 8095	eV	1.2-2.5
$\phi_{\text{Fe,Fe}} \left(b_{\text{Fe,Fe}}^{(7)}, s_{\text{Fe,Fe}}^{(7)} \right)$	-20.708 542 6576	eV	1.2-2.6
$\phi_{\text{Fe,Fe}} \left(b_{\text{Fe,Fe}}^{(8)}, s_{\text{Fe,Fe}}^{(8)} \right)$	45.457 894 2098	eV	1.2-2.65
$\phi_{\text{Fe,Fe}} \left(b_{\text{Fe,Fe}}^{(9)}, s_{\text{Fe,Fe}}^{(9)} \right)$	-23.636 881 0075	eV	1.2-2.7
$\phi_{\text{Fe,Fe}} \left(b_{\text{Fe,Fe}}^{(10)}, s_{\text{Fe,Fe}}^{(10)} \right)$	0.289 112 8787	eV	1.2-2.8
$\phi_{\text{Fe,Fe}} \left(b_{\text{Fe,Fe}}^{(11)}, s_{\text{Fe,Fe}}^{(11)} \right)$	-0.8240766547	eV	1.2-3.0
$\phi_{\text{Fe,Fe}} \left(b_{\text{Fe,Fe}}^{(12)}, s_{\text{Fe,Fe}}^{(12)} \right)$	1.593 369 4153	eV	1.2-3.3
$\phi_{\text{Fe,Fe}} \left(b_{\text{Fe,Fe}}^{(13)}, s_{\text{Fe,Fe}}^{(13)} \right)$	-0.247 520 6962	eV	1.2-3.7
$\phi_{\text{Fe,Fe}} \left(b_{\text{Fe,Fe}}^{(14)}, s_{\text{Fe,Fe}}^{(14)} \right)$	-0.090 529 8856	eV	1.2-4.2
$\phi_{\text{Fe,Fe}} \left(b_{\text{Fe,Fe}}^{(15)}, s_{\text{Fe,Fe}}^{(15)} \right)$	0.114 524 7138	eV	1.2-4.7
$\phi_{\text{Fe,Fe}} \left(b_{\text{Fe,Fe}}^{(16)}, s_{\text{Fe,Fe}}^{(16)} \right)$	-0.031 104 9596	eV	1.2-5.3

Table 3.7: The parameters of the RF-MEAM potential for Fe found in this study, the parameters are labelled as in the Equations (3.1)-(3.8) in Section 3.2.1.

3.5. CONCLUSIONS

IN this Chapter a RF-MEAM potential for iron has been obtained for the purpose of simulating both α -Fe and γ -Fe. The presented potential reproduces many experimental material properties, such as defects, interfaces or surfaces, better than prior (M)EAM potentials. The current RF-MEAM potential is ready to for use in LAMMPS for calculations on large systems, for which MLP's are still impractical.

The potential presented in this work predicts accurate lattice properties and defect energies, most notably for vacancies, and self-diffusion. Additionally surface energies and stacking fault energies are predicted well. Orientation relations between the bcc and fcc lattice are predicted well for both NW and KS. The thermal expansion in the 800 K to 1300 K temperature range follows the experimental data well. Therefore the potential presented here can be used for simulations in α -Fe, and in γ -Fe, as well as in inter phase simulations.

REFERENCES

- [1] R. J. Sluiter, M. H. F. Sluiter, W. G. T. Kranendonk, and C. Bos. A Reference-Free MEAM potential for α -Fe and γ -Fe. *Journal of Physics: Condensed Matter*, 34:505901, 2022.
- [2] G. J. Ackland, M. I. Mendeleev, D. J. Srolovitz, S. Han, and A. V. Barashev. Development of an interatomic potential for phosphorus impurities in α -iron. *Journal of physics: Condensed matter*, 16:S2629–S2642, 2004.
- [3] M. Müller, P. Erhart, and K. Albe. Analytic bond-order potential for bcc and fcc iron-comparison with established embedded-atom method potentials. *Journal of physics: Condensed matter*, 19:326220, 2007.
- [4] G. J. Ackland, D. J. Bacon, A. F. Calder, and T. Harry. Computer simulation of point defect properties in dilute Fe-Cu alloy using many-body interatomic potential. *Philosophical magazine A*, 75(3):713–732, 1997.
- [5] M. I. Mendeleev, S. Han, D. J. Srolovitz, G. J. Ackland, D. Y. Sun, and M. Asta. Development of new interatomic potentials appropriate for crystalline and liquid iron. *Philosophical magazine*, 83(35):3977–3994, 2003.
- [6] B.-J. Lee, M. I. Baskes, H. Kim, and Y. K. Cho. Second nearest-neighbour modified embedded atom method potentials for bcc transition metals. *Physical review B*, 64:184102, 2001.
- [7] R. A. Johnson. Interstitials and vancancies in α -iron. *Physical review*, 134(5A):A1329–A1336, 1964.

- [8] R. Alexander, L. Proville, C. S. Becquart, A. M. Goryeava, J. Dérès, C. Lapointe, and M. C. Marinica. Interatomic potentials for irradiation-induced defects in iron. *Journal of Nuclear Materials*, 535:152141, 2020.
- [9] T. Lee, M. I. Baskes, S. M. Valone, and J. D. Doll. Atomistic modeling of thermodynamic equilibrium and polymorphism of iron. *Journal of physics: condensed matter*, 24:225404, 2012.
- [10] D. Dragoni, T. D. Daff, G. Csányi, and N. Marzari. Achieving DFT accuracy with a machine-learning interatomic potential: Thermomechanics and defects in bcc ferromagnetic iron. *Physical Review Materials*, 2:013808, 2018.
- [11] H. Mori and T. Ozaki. Neural network atomic potential to investigate the dislocation dynamics in bcc iron. *Physical Review Materials*, 4:040601(R), 2020.
- [12] A. E. Carlsson. Beyond pair potentials in elemental transition metals and semiconductors. *Solid state physics*, 43:1–91, 1990.
- [13] J. H. Rose, J. R. Smith, F. Guinea, and J. Ferrante. Universal features of the equation of state of metals. *Physical Review B*, 29(6):2963–2969, 1984.
- [14] M. Timonova and B. J. Thijsse. Optimizing the MEAM potential for silicon. *Modelling and Simulation in Materials Science and Engineering*, 19:015003, 2011.
- [15] M. I. Mendeleev, S. Han, W.-J. Son, G. J. Ackland, and D. J. Srolovitz. Simulation of the interaction between Fe impurities and point defects in V. *Physical review B*, 76:214105, 2007.
- [16] C. S. Becquart, J. M. Raulot, G. Bencteux, C. Domain, M. Perez, S. Garruchet, and H. Nguyen. Atomistic modeling of an Fe system with a small concentration of C. *Computational materials science*, 40:119–129, 2007.
- [17] A. I. Duff, M. W. Finnis, P. Maugis, B. J. Thijsse, and M. H. F. Sluiter. MEAMfit: A reference-free embedded atom method (RF-MEAM) energy and force-fitting code. *Computer physics communications*, 196:439–445, 2015.
- [18] J. Neuhaus, M. Leitner, K. Nicolaus, W. Party, B. Hennion, and A. Hiess. Role of vibrational entropy in the stabilization of the high-temperature phases of iron. *Physical review B*, 89:184302, 2014.
- [19] J. F. Ziegler, J. P. Biersack, and U. Littmark. *The stopping and range of ions in solids*, volume 1. Pergamon, 1985.
- [20] P. Srinivasan, A. I. Duff, T. A. Mellan, M. H. F. Sluiter, L. Nicola, and A. Simone. The effectiveness of reference-free modified embedded atom method potentials demonstrated for NiTi and NbMoTaW. *Modelling and simulation in materials science and engineering*, 27:065013, 2019.
- [21] G. Kresse and J. Hafner. Ab initio molecular dynamics for liquid metals. *Physical Review B*, 47(1):558–561, 1993.

- [22] G. Kresse and J. Hafner. Ab initio molecular-dynamics simulation of the liquid-metal-amorphous-semiconductor transition in germanium. *Physical Review B*, 49(20):14251–14269, 1994.
- [23] G. Kresse and J. Furthmüller. Efficient iterative schemes for ab initio total-energy calculations using a plane-wave basis set. *Physical Review B*, 54(16):11169–11186, 1996.
- [24] G. Kresse and J. Furthmüller. Efficiency of ab-initio total energy calculations for metals and semiconductors using a plane-wave basis set. *Computational Materials Science*, 6:15–50, 1996.
- [25] G. Kresse and D. Joubert. From ultrasoft pseudo potentials to the projector augmented-wave method. *Physical Review B*, 59(3):1758–1775, 1999.
- [26] H. Hasegawa and D. G. Pettifor. Microscopic theory of the temperature-pressure phase diagram of iron. *Physical review letters*, 50(2):130–133, 1983.
- [27] S. L. Dudarev and P. M. Derlet. A ‘magnetic’ interatomic potential for molecular dynamics simulations. *Journal of physics: condensed matter*, 17:7097–7118, 2005.
- [28] G. Ghosh and G. B. Olson. The isotropic shear modulus of multicomponent Fe-base solid solutions. *Acta materialia*, 50:2655–2675, 2002.
- [29] Y. P. Varshni. Temperature dependence of the elastic constants. *Physical review B*, 2(10):3952–3958, 1970.
- [30] L.-E. Lindgren and J. Gyhlesten Back. Elastic properties of ferrite and austenite in low alloy steel versus temperature and alloying. *Materialia*, 5:100193, 2019.
- [31] J. Kundrak, Z. Gácsi, K. Gyáni, V. Bana, and G. Tomolya. X-ray diffraction investigation of white layer development in hard-tuned surfaces. *International journal of advanced manufacturing technology*, 62:457–469, 2012.
- [32] Z. Nishiyama, M. E. Fine, M. Meshii, and C. M. Wayman. *Martensitic transformation*. Academic press, first edition, January 1978.
- [33] B. Hutchinson, M. Malmström, J. Lönnqvist, P. Bate, H. Ehteshami, and P. A. Korzhavyi. Elasticity and wave velocity in fcc iron (austenite) at elevated temperatures - Experimental verification of *ab-initio* calculations. *Ultrasonics*, 87:44–47, 2018.
- [34] J. Zarestky and C. Stassis. Lattice dynamics of γ -Fe. *Physical review B*, 35(9):4500–4502, 1987.
- [35] N. Singh. Lattice dynamics of γ -iron at 1428 K. *Physica status solidi B*, 156:K33–K36, 1989.
- [36] F. Gao, R. L. Johnston, and J. N. Murrel. Empirical many-body potential energy functions for iron. *Journal of physical chemistry*, 97(46):12073–12082, 1993.

- [37] H. Ehteshami and P. A. Korzhavyi. Thermophysical properties of paramagnetic Fe from first principles. *Physical Review B*, 96:224406, 2017.
- [38] H. L. Zhang, N. Al-Zoubi, B. Johansson, and L. Vitos. Alloying effects on the elastic parameters of ferromagnetic and paramagnetic Fe from first-principles theory. *Journal of applied physics*, 110:073707, 2011.
- [39] M. Acet, M. Zähres, and E. F. Wassermann. High-temperature moment-volume instability and anti-Invar of γ -Fe. *Physical review B*, 49(9):6012–6017, 1994.
- [40] M. Souissi and H. Numakura. Elastic properties of Fe-C and Fe-N martensites. *ISIJ international*, 55(7):1512–1521, 2015.
- [41] F. Nix and D. MacNair. The thermal expansion of pure metals: Copper, gold, aluminum, nickel, and iron. *Physical Review*, 60:597–605, 1941.
- [42] J. A. Rayne and B. S. Chandrasekhar. Elastic constants of iron from 4.2 to 300 K. *Physical review*, 122(6):1714–1716, 1961.
- [43] C. Kittel. *Intriduction to solid state physics*. Wiley, sixth edition, 1986.
- [44] Q. Chen and B. Sundman. Modeling of thermodynamic properties for bcc, fcc, liquid and amorphous iron. *Journal of phase equilibria*, 22(6):631–644, 2001.
- [45] H. C. Herper, E. Hoffmann, and P. Entel. Ab initio full-potential study of the structural and magnetic phase stability of iron. *Physical review B*, 60(6):3839–3848, 1999.
- [46] T. P. C. Klaver, D. J. Hepburn, and G. J. Ackland. Defect and solute properties in dilute Fe-Cr-Ni austenitic alloys from first principles. *Physical Review B*, 85:174111, 2012.
- [47] H-. K. Mao, W. A. Bassett, and T. Takahashi. Effect of pressure on crystal structure and lattica parameters of iron up to 300 kbar. *Journal of applied physics*, 38(1):272–276, 1967.
- [48] A. Glensk, B. Grabowski, T. Hickel, and J. Neugebauer. Breakdown of the Arrhenius law describing vacancy formation energies: the importance of local anharmonicity revealed by *ab initio* thermodynamics. *Physical review X*, 4:011018, 2014.
- [49] R. Nazarov, T. Hickel, and J. Neugebauer. First-principles study of the thermodynamics of hydrogen-vacancy interaction in fcc iron. *Physical review B*, 82:224104, 2010.
- [50] C. Domain and C. S. Becquart. *Ab initio* calculations of defects in Fe and dilute Fe-Cu alloys. *Physical Review B*, 65:024103, 2001.
- [51] F. Williame, C. C. Fu, M. C. Marinica, and J. Dalla Torre. Stability and mobility of self-interstitials and small interstitial clusters in α -iron: ab initio and emperical potential calculations. *Nuclear instruments and methods in physics research B*, 228:92–99, 2005.

- [52] Z. Chen, N. Kioussis, N. Ghoniem, and D. Seif. Strain-field effects on the formation and migration energies of self interstitials in α -Fe from first principles. *Physical review B*, 81:094102, 2010.
- [53] M.-C. Marinica, F. Willame, and N. Mousseau. Energy landscape of small clusters of self-interstitial dumbbells in iron. *Physical review B*, 83:094119, 2011.
- [54] W. R. Tyson and W. A. Miller. Surface free energies of solid metals estimation from liquid surface tension measurements. *Surface science*, 62:267–276, 1977.
- [55] H. Jin, I. Elfimov, and M. Militzer. First-principles simulations of binding energies of alloying elements to the ferrite-austenite interface in iron. *Journal of applied physics*, 123:085303, 2018.
- [56] T. Nagano and M. Enomoto. Calculation of the interfacial energies between α and γ iron and equilibrium particle shape. *Metallurgical and materials transactions A*, 37A:929–937, 2006.
- [57] S. Starikov, D. Smirnova, T. Pradhan, Y. Lysogorskiy, H. Chapman, M. Mrovec, and R. Drautz. Angular-dependent interatomic potential for large-scale atomistic simulation of iron: Development and comprehensive comparison with existing interatomic models. *Physical Review Materials*, 5:063607, 2021.
- [58] P. Hirel. AtomsK: A tool for manipulating and converting atomic data files. *Computer Physics Communications*, 197:212–219, 2015.
- [59] P. Ehrhart. *Landolt-Börnstein: Numerical data and functional relationships in science and technology*, volume 3. Springer, 1991.
- [60] C. D. Versteyleen, N. H. van Dijk, and M. H. F. Sluiter. First-principles analysis of solute diffusion in dilute bcc Fe- X alloys. *Physical review B*, 96:094105, 2017.
- [61] S. M. Kim and W. J. L. Buyers. Vacancy formation energy in iron by positron annihilation. *Journal of physics F: Metal physics*, 8(5):L103, 1978.
- [62] B. Medasani, M. Haranczyk, A. Canning, and M. Asta. Vacancy formation energies in metals: A comparison of MetaGGA with LDA and GGA exchange-correlation functionals. *Computational Materials Science*, 101:96–107, 2015.
- [63] H. Matter, J. Winter, and W. Trifthäuser. Phase transformations and vacancy formation energies of transition metals by positron annihilation. *Applied physics*, 20:135–140, 1979.
- [64] H. Oikawa. Lattice self-diffusion in solid iron: a critical review. *ISIJ*, 68(10):1489–1497, 1982. Japanese.
- [65] C.-C. Fu, F. Willame, and P. Ordejón. Stability and mobility of mono- and di-interstitials in α -Fe. *Physical review letters*, 92(17):175503, 2004.

- [66] M. J. S. Spencer, A. Hung, I. K. Snook, and I. Yarovskiy. Density functional theory study of the relaxation and energy of iron surfaces. *Surface science*, 513:389–398, 2002.
- [67] P. Błonski and A. Kiejna. Calculation of surface properties of bcc iron. *Vacuum*, 74:179–183, 2004.
- [68] J. Yu, X. Lin, J. Wang, J. Chen, and W. Huang. First-principles study of the relaxation and energy of bcc-Fe, fcc-Fe and AISI-304 stainless steel surfaces. *Applied surface science*, 255:9032–9039, 2009.
- [69] J.-A. Yan, C.-Y. Wang, and S.-Y. Wang. Generalized-stacking-fault energy and dislocation properties in bcc Fe: A first-principles study. *Physical review B*, 70:174105, 2004.
- [70] L. Ventelon and F. Willame. Generalized stacking-faults and screw-dislocation core-structure in bcc iron: A comparison between ab initio calculations and empirical potentials. *Philosophical Magazine*, 90:1063–1074, 2010.

4

ATOMISTIC SIMULATION OF CARBIDE FORMATION IN FERRITE

Est modus in rebus, sunt certi denique fines, quos ultra citraque nequit consistere rectum.

Horatius

For with what judgement ye judge, ye shall be judged: and with what measure ye mete, it shall be measured to you again.

Matthew 7:2

In this study possible routes from dissolved M and C atoms to a M-C (M = Ti, Nb) cluster are studied. Using atomistic modelling to perform relaxation simulations and molecular dynamics (MD) simulations for the Fe-M-C ternary system, the formation of clusters is studied for M. Additionally the stability of M-C clusters is assessed. The clustering of M and C atoms as observed in experiments is also found in simulations. The initial clusters found in this work have a (Fe,M)C composition with a large Fe fraction. Moreover, structurally relaxed clusters reveal that there are growth pathways with a monotone decrease in Gibbs energy, suggesting that the highest energy barrier in the formation of M-C clusters is the diffusion barrier for the atoms forming the cluster.

The development of M-C clusters as found in this study suggests a formation mechanism for nano-precipitation of carbides consisting of several steps; first a C cluster forms, then M atoms attach to the C cluster forming a (Fe,M)C cluster, and in the final step the (Fe,M)C cluster transforms to a NaCl-structured carbide.

The contents of this chapter have been published in *Computational Materials Science* [1], and parts were presented at CALPHAD XLIX [2].

4.1. INTRODUCTION

PREDICTING precipitate development in micro-alloyed steels is a key part in optimally utilizing the precipitation hardening effect. The number of precipitates and their size are determining factors in hardening, e.g., [3, 4]. Understanding the formation of precipitates is therefore of critical importance. In transmission electron microscopy (TEM) and atom probe tomography (APT) it has been shown that various carbides initially form as platelets in the (100) planes of the bcc-Fe lattice [5–11], which can be linked to the Baker-Nutting interface orientation relation (BN-OR) [12]. The initial stoichiometry differs from the final stoichiometry of a metal carbide ‘MC’ (e.g. NbC, TiC, or VC) [6, 8, 13]. Additionally the shape changes over time, [10] observes plate thickening, and [7] shows that a platelet grows into a lenticular shaped particle, but for larger precipitates a spheroidal form has been observed, e.g., [14].

These experiments have shown that the formation of carbides appears to occur in several steps. Wang et al. [8] distinguish an ‘embryo-cluster’, a ‘Guinier-Preston (GP) cluster’, and finally a NaCl-structured nano-precipitate. Both the embryo-cluster and GP-cluster are coherent with the bcc-ferrite matrix, in this work both will be referred to as ‘proto-precipitate’ as they are similar in appearance. The GP-zone clustering has also been observed for Nb-nitrides [6, 9].

In this work the process leading up to the formation of such a proto-precipitate is investigated using static relaxation at 0 K and molecular dynamics (MD) at finite temperatures using Modified Embedded Atom Method (MEAM) potentials in the LAMMPS molecular dynamics simulation software [15]. First the pair interactions for several M-M, M-C and C-C atom pairs are calculated, here the results for the MEAM potentials are compared to Density Functional Theory (DFT) results. From static relaxation of larger clusters it is found that the formation of stable M-rich clusters is preceded by the formation of carbon clusters, or, at higher temperatures by the occurrence of carbon cluster fluctuations, next, on these carbon clusters the M atoms then attach to form a proto-precipitate with an ordered FeMC_3 structure observed for both Nb and Ti. The FeMC_3 clusters are estimated to be thermally stable at temperatures over 1100 K for FeNbC_3 , and FeTiC_3 clusters are estimated to be stable at temperatures near the ferrite-austenite transition temperature of 1185 K. From these findings it can be derived that instead of a classical model for nucleation [16–19], the formation of M-carbides occurs in several steps; i) ordering of C atoms in Fe with local accumulation or clustering of C atoms, ii) attraction of M atoms and stabilisation in a FeMC_3 cluster, and iii) structural transformation to NaCl-structured nano-precipitate. The structural transformation is studied elsewhere [20].

First the methodology used to simulate various clusters is explained in Section 4.2. Then in Section 4.3 the results for various simulations are presented. In Section 4.4 the results are discussed.

4.2. METHODOLOGY

4.2.1. STATIC RELAXATIONS IN FE-M-C

IN order to simulate atom clusters a MEAM potential for the Fe-Nb-C [21] and Fe-Ti-C [22] ternary systems are used. LAMMPS (v 3mar20) [15] was used for static relax-

ations, MD, and Nudged Elastic Bands (NEB) method calculations [23]. Stopping criteria are set such that the energy change between iterations is $1 \cdot 10^{-8}$ eV, and the magnitude of all force components on any atom must be less than $1 \cdot 10^{-8}$ eV/Å. Simulations are performed at constant volume, all supercells consist of a bcc lattice of $n \times n \times n$ bcc unit cells with a lattice parameter fixed at $n \cdot 2.864$ Å which is the equilibrium lattice parameter for bcc Fe for the used potentials [21, 22].

Before examining clusters the relaxation for a single M and a single C atom embedded in the ferrite matrix has been performed, to find the solute excess energy associated with single M and C atoms. It is assumed that M atoms only occupy substitutional bcc lattice sites of the ferrite matrix, and C atoms only occupy octahedral interstitial sites in the bcc lattice. The relaxation is performed in a supercell of $10 \times 10 \times 10$ bcc unit cells, the solute excess energies for the single embedded atoms differ less than 1 meV with the supercell with $20 \times 20 \times 20$ bcc unit cells, which is a difference smaller than 0.5% of the solute excess energies. Therefore we conclude that the influence of the cell size is negligible. The resulting solute excess energies for the single embedded atom are taken as reference energies for a M or C atom fully dissolved, i.e., uniformly distributed, in the ferrite matrix:

$$\Delta E(X) = E(\text{Fe}_i X) - i E_{\text{Fe}}^c. \quad (4.1)$$

Where $\Delta E(X)$ is the solute excess energy ($X = M, C$), and $E(\text{Fe}_i X)$ is the total energy of the cell containing i Fe atoms and a single M or C atom. E_{Fe}^c is the cohesive energy per atom taken from [21, 22], $E_{\text{Fe}}^c = -4.29$ eV, where the reference structure for Fe is bcc. For an isolated Nb atom the solute excess energy is -7.51 eV, for Ti -5.39 eV, and for C -6.06 eV (in the $10 \times 10 \times 10$ bcc unit cell supercell).

Using molecular statics, small clusters of M and C atoms are constructed within a bcc Fe crystal, these small clusters are aimed at investigating the onset formation of a M-C cluster. All clusters are, unless stated otherwise, constructed as single-layered clusters. The energy of the relaxed clusters is compared to the energy of a bcc Fe crystal where the M and C atoms are uniformly distributed in the infinitely diluted limit. To compare energies a binding energy for a supercell containing i Fe atoms, j M atoms and k C atoms with a total energy, $E(\text{Fe}_i \text{M}_j \text{C}_k)$, is determined as

$$E_{\text{bind}} = i E_{\text{Fe}}^c + j \Delta E(M) + k \Delta E(C) - E(\text{Fe}_i \text{M}_j \text{C}_k). \quad (4.2)$$

Where $\Delta E(X)$ is defined in Eq. (4.1). A decrease in total energy translates to a positive binding energy, such a cluster is favourable with respect to the infinitely diluted solid solution. All clusters are simulated in various size cells, when the results differ less than 0.01 eV/atom for the atoms in the M-C cluster between sizes the interference of cell boundaries are considered negligible. This means that for several small clusters a cell containing $10 \times 10 \times 10$ bcc unit cells is used, but larger clusters were relaxed in $20 \times 20 \times 20$ or $40 \times 40 \times 20$ bcc unit cells.

To focus on the essential steps in the precipitate formation, the larger model systems contain clusters with a square shape. The square shape is the simplest shape to roughly approximate the shape observed in experiments [6, 8]. The square shape greatly reduces the number of variations due to symmetry. A second advantage is that different sizes are easily determined, i.e., we may speak of a $n \times n$ square.

4.2.2. DFT CALCULATIONS

DFT calculations were performed using projector-augmented wave (PAW) pseudo potentials as implemented in the Vienna Ab initio Simulation Package (VASP version 5.3.5) [24–28].

For both M-M and M-C pairs we investigate a binding energy E_{bind} at 0 K where a positive value indicates attraction and a negative energy indicates repulsion. To evaluate the binding energy Eqs. (4.1) and (4.2) are used, where instead of the cohesive energy for Fe, E_{Fe}^c , the energy of an Fe atom in a perfect bcc lattice is calculated and used. The solute excess energies are also re-evaluated for the Nb, Ti and C atoms.

The DFT calculations are performed in supercells at a fixed volume determined by the equilibrium lattice parameter for bcc Fe which is found to be 2.833 Å. Three different supercell sizes are used all containing a perfect bcc lattice with $3 \times 3 \times 3$, $4 \times 4 \times 4$, and a $5 \times 5 \times 5$ bcc unit cells, containing 54, 128, and 250 substitutional lattice sites respectively.

For the $3 \times 3 \times 3$ supercell we use 6 k -points along all axes, the k -points are arranged following a regular Γ -centred mesh. For the $4 \times 4 \times 4$ and $5 \times 5 \times 5$ supercell we use 4 k -points along all axes, again using the regular Γ -centred mesh. The electronic wave functions are expanded in terms of plane waves up to a cut-off kinetic energy set at 400 eV for all supercell sizes. In all calculations the precision is set to medium, and convergence criteria for energy and force are set at 0.1 meV and 100 meV/nm respectively.

4.2.3. MOLECULAR DYNAMICS FOR FE-NB-C

As the formation of precipitates occurs at finite temperatures, particularly above 800 K, MD is used to simulate Fe-Nb-C clusters at finite temperatures in a supercell containing $10 \times 10 \times 10$ bcc unit cells. Simulations are performed in ferrite at 1150 K, just below the ferrite-austenite transformation temperature. Two types of system are assessed: first a system containing a random distribution of Nb and C atoms. Vacancies, zero, one or ten, are added to allow for the movement of Nb and Fe atoms. The second type is a system in which a cluster already exists, and here the stability of the cluster is tested. Again vacancies are added to allow for Nb and Fe movement.

MD simulations are performed in LAMMPS [15] using the NPT-ensemble with $P=0$, this is done to represent realistic heating of a steel slab. Before simulation at constant temperature the supercell is heated to the chosen temperature in $1 \cdot 10^5$ time steps. The time step is set at 1 fs, and for each cell a total of $20 \cdot 10^6$ time steps are performed, so the total simulated time is 20 ns. The pressure is relaxed in 800 time steps and the thermostat in 350 time steps, both are chosen to avoid rapid fluctuations but still allow for equilibration well within the run-time of the simulation.

In addition to MD simulations the migration barrier for Nb and C atoms near clusters is examined using the NEB method [23] at $T = 0$ K. For a M atom diffusion requires the presence of a vacancy, but C atoms can move without need for vacancies, between octahedral interstitial sites. NEB calculations are performed in static crystals in $10 \times 10 \times 10$ bcc unit cell supercells at a fixed volume where one atom is moved between an initial and final site and its neighbours are displaced following the NEB principle.

4.3. RESULTS

4.3.1. STATIC RELAXATION

FIRST M-M pair configurations are considered, where two Nb or two Ti atoms are placed on bcc lattice sites in an Fe matrix. Binding energies of the pairs were calculated using both LAMMPS and DFT. Various pairs are illustrated in Figure 4.1, the corresponding binding energies are presented in Tables 4.1 and 4.2. Secondly fifteen C-C pair configurations are considered, also presented in Figure 4.1 and in Table 4.3. Note that positive (negative) energies mean attraction (repulsion). The comparison between the results for the MEAM potentials (in LAMMPS) and DFT reveals some important similarities with relevance for the MC carbide formation.

Nb and Ti carbides can form (semi-)coherent interfaces with ferrite [29, 30] where the M atoms are separated roughly one ferrite lattice parameter. Hence the M-M pairs I-II, I-III, I-IV, and I-V are of great significance. The pairs with the smallest M-M separation, i.e., the I-II and I-III pairs display significant repulsive behaviour. Pairs with greater separation, the I-VI and I-VII pairs, display little interaction for the MEAM potential which even shows (small) attraction for these pairs. This indicates that the MEAM potentials will not form close M atom pairs in the absence of C atoms, in contrast to the DFT results, see Tables 4.1 and 4.2.

Interaction generally weakens when atoms are further apart, e.g., [31], but the interaction for the MEAM potentials seems especially weak. The DFT results show attraction for the I-IV Nb-Nb pair and for the I-V Ti-Ti pair, furthermore the I-VI and I-VII pairs have a repulsive interaction. For the I-II pair a repulsive interaction is found both in the LAMMPS and DFT calculations, although it is part of the coherent carbide-ferrite interface. The repulsive interaction between the M atoms at close range shows that the introduction of carbon is necessary to stabilise this pair in a larger cluster.

For the M-C pairs there is a better agreement between MEAM and DFT, albeit only as to which pairs are favoured, the actual magnitudes of the binding energy differ noticeably. For Nb-C the I-4 pair is favoured and for Ti-C the I-1 pair. There is also agreement for the C-C pairs (Table 4.3), where the O-3 pair is highly favoured in both MEAM and DFT. Moreover, the C-C pairs display significantly positive binding energies. Therefore C clusters may easily form, and are expected to act as a catalyst for the formation of M-C clusters, as shown in Figure 4.2.

From the analysis of the various pair interactions of M and C atoms a pattern seems to exist. Both Nb and Ti prefer similar M-C pair configurations. For the M-M pairs there is a slight difference, where the Nb-Nb pair prefers a I-IV pair (for MEAM only for both M atoms within the same bcc unit cell) and Ti-Ti prefers I-V (also within the same unit cell). The energy difference between the I-IV and I-V pair is small. So there seem to be some parallels between both metals, particularly when we consider the DFT results. Both metals have similar metal bond lengths [32], a key difference however is that the Ti atoms are smaller when embedded in the bcc Fe matrix [33]. This lowers matrix strain around the Ti atoms compared to the strain caused by the Nb atoms.

From simple pairs larger clusters are constructed by adding atoms in various positions on the bcc lattice for M atoms (i.e., replacing an Fe atom) and its octahedral interstitial positions for C atoms. These clusters are made to simulate the onset of M-C cluster formation. It is found that C clusters have highly favourable binding energies, adding C

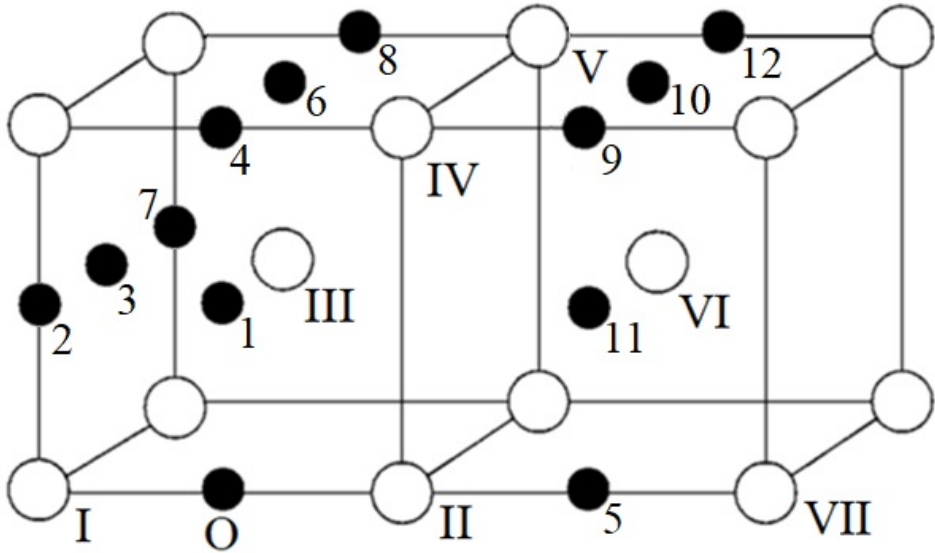


Figure 4.1: Schematic representation of the M-M and M-C pairs. All M atoms are placed at the bcc lattice sites (open circles) labelled with a capital Roman numeral, the carbon atoms may be placed at the closed circles labelled with Arabic numerals.

atoms to a pre-existing C cluster can increase the binding energy more than the binding of the most favourable C-C pair. Combined with the high mobility of C atoms in the ferrite matrix it is concluded that C clusters will form quickly. From the C-C pair interactions we find that the C atom clustering is an ordering effect, as for the various C atoms in the random solution a lot of energy can be gained by forming pairs and larger clusters. We note that for higher C concentrations at temperatures below 800 K spinodal decomposition of the Fe-C solid solution is observed, e.g., [34–41].

In Figure 4.2 several evolution paths, starting from a single C atom, are presented for a M-C cluster inhabiting a single (100) plane. For each atom addition the gain in binding energy is shown. We selectively display paths with favourable binding energy gain for each added atom using Eq. (4.2). These small clusters remain coherent with the bcc lattice after relaxation, and show a (Fe,M)C-like character.

We remark that the (Fe,M)C clusters found in Figure 4.2 display a distinct pattern where the Fe and M atoms lie in a ‘chequerboard pattern’. The emergence of this pattern is likely tied to the matrix strain caused by the size differences between M and Fe atoms as the [100] direction is the elastically soft direction in bcc Fe. Such a chequerboard pattern allows for the observed coherency between the (Fe,M)C cluster lying in a (100) plane and its adjacent (100) planes in the matrix. In Figure 4.3 the ring-shaped cluster shown in Figure 4.2 is expanded, in Table 4.4 the binding energies for added atoms are given. The C atoms also form a particular pattern, which is fully described in Section 4.3.2. Using this pattern the most favourable growth is found to be in-plane. There are sites out of the (100) habit plane of the cluster onto which M atoms can attach, but these are not the

Nb-Nb Cell size	E_{bind} [eV] static relaxation (LAMMPS) [21]					E_{bind} [eV] DFT		
	3 × 3 ×3	4 × 4 ×4	5 × 5 ×5	10 × 10 ×10	20 × 20 ×20	3 × 3 ×3	4 × 4 ×4	5 × 5 ×5
I-II	-0.104	-0.084	-0.079	-0.074	-0.074	-0.216	-0.170	-0.148
I-III	-0.070	-0.052	-0.046	-0.041	-0.041	-0.402	-0.393	-0.335
I-IV	-0.050	-0.035	-0.030	-0.025	-0.025	-0.016	-0.006	0.026
I-V	-0.069	-0.046	-0.038	-0.032	-0.032	-0.053	-0.053	-0.004
I-VI	-0.010	-0.005	0.000	0.004	0.004	-0.040	-0.040	-0.025
I-VII	-	-0.008	-0.001	0.002	0.002	-	-0.034	0.025
Nb-C								
I-O	-1.101	-1.036	-1.021	-1.006	-1.006	-1.366	-1.209	-1.095
I-1	0.002	0.033	0.042	0.050	0.050	-0.108	-0.059	0.018
I-4	0.207	0.229	0.237	0.244	0.244	-0.103	0.070	0.102
I-5	-0.090	-0.065	-0.055	-0.050	-0.049	-0.318	-0.213	-0.145
I-6	-0.045	-0.032	-0.027	-0.022	-0.022	-0.271	-0.097	-0.047
I-8	-0.025	0.005	0.016	0.024	0.024	-0.142	0.018	0.068
I-9	-0.031	-0.030	-0.021	-0.017	-0.015	-0.078	0.012	0.063
I-10	-0.027	-0.015	-0.005	0.002	0.003	-0.089	0.016	0.064
I-11	-0.005	0.011	0.020	0.028	0.028	-0.062	0.023	0.062
I-12	-0.057	-0.058	-0.047	-0.040	-0.039	-0.119	-0.046	0.014

Table 4.1: Pair binding energies for Nb-Nb and Nb-C pairs presented in Figure 4.1. The DFT values were calculated as part of this work following Section 4.2.2. The LAMMPS results are from the static relaxation calculations. The most favourable (or least unfavourable) pair is marked in bold.

most favourable sites. The C atoms enhance the in-plane growth of the chequerboard pattern as shown in Table 4.4.

We label the (Fe,M)C clusters as proto-precipitates, which we consider to be the earliest stages of nano-precipitate formation. Direct construction of a 2D NaCl-structured cluster is not favoured. For both Ti-C and Nb-C clusters a similar behaviour is observed where clusters are formed that lie in the {100} planes of the ferrite matrix, which is also found for nano-precipitates observed in experiments [5–11]. Note that the relaxations are performed at 0 K, so thermal effects are not present.

In Figure 4.2 it is shown that clusters tend to start from a C cluster (here a C-C pair). The two C-C pairs shown in Figure 4.2 have a higher binding energy than the shown M-C pairs in Table 4.3. Moreover, bonding of a M atom to each C-C pair increases the total binding energy more than the binding of a single M atom to a C atom. This result shows that C-C pairs (and clusters), which can form through Fe-C spinodal decomposition, or as a temporal fluctuation, are essential for the formation of M-C clusters, as the M atoms do not display attractive interaction for the M-M pairs in Tables 4.1 and 4.2. Moreover, as some M-M pairs are favourable according to the DFT data, it is worthwhile to note that the bond between M and C atoms is more favourable.

The next step is to investigate the role of vacancies. It is observed, in simulations, that the zone around the cluster, the ‘transition envelope’ or ‘transition zone’, attracts

Ti-Ti Cell size	E_{bind} [eV] static relaxation (LAMMPS) [22]					E_{bind} [eV] DFT		
	3 × 3 ×3	4 × 4 ×4	5 × 5 ×5	10 × 10 ×10	20 × 20 ×20	3 × 3 ×3	4 × 4 ×4	5 × 5 ×5
I-II	-0.047	-0.024	-0.024	-0.024	-0.024	-0.143	-0.136	-0.160
I-III	-0.293	-0.278	-0.277	-0.275	-0.275	-0.237	-0.249	-0.249
I-IV	-0.012	-0.021	-0.019	-0.019	-0.019	0.007	-0.009	-0.016
I-V	-0.026	-0.030	-0.027	-0.026	-0.026	0.019	0.011	0.010
I-VI	0.017	0.012	0.014	0.014	0.014	-0.024	-0.024	-0.027
I-VII	-	-0.037	-0.017	-0.017	-0.017	-	-0.017	-0.013
Ti-C								
I-O	-0.851	-0.818	-0.805	-0.791	-0.790	-0.817	-0.728	-0.628
I-1	0.172	0.186	0.189	0.192	0.192	0.012	0.038	0.093
I-4	0.145	0.141	0.144	0.146	0.145	-0.022	0.103	0.128
I-5	-0.026	0.006	0.005	0.008	0.009	-0.158	-0.103	-0.069
I-6	-0.042	-0.052	-0.053	-0.052	-0.052	-0.150	-0.027	0.005
I-8	-0.036	-0.018	-0.012	-0.009	-0.009	-0.090	0.033	0.057
I-9	-0.017	-0.019	-0.017	-0.015	-0.015	-0.023	0.040	0.063
I-10	-0.004	0.005	0.007	0.010	0.009	-0.039	0.033	0.061
I-11	-0.019	-0.013	-0.008	-0.005	-0.005	-0.040	0.041	0.051
I-12	-0.033	-0.038	-0.038	-0.036	-0.036	-0.059	-0.012	0.024

Table 4.2: Pair binding energies for Ti-Ti and Ti-C pairs presented in Figure 4.1. The DFT values were calculated as part of this work following Section 4.2.2. The LAMMPS results are from the static relaxation calculations. The most favourable (or least unfavourable) pair is marked in bold.

vacancies. The existence of vacancies in this envelope reduces the strain near the cluster, which was also noticed for TiC [8, 42]. The clusters also attract vacancies inside the cluster's (100) habit plane, particularly at the sites where the Fe atoms are in the checkerboard pattern. The vacancies lower the local strain, as the M atoms are generally large compared to the Fe atoms. Moreover the MEAM potential has a strong positive vacancy C atom bond [43].

NEB is used to determine migration barriers for Nb and C atoms near various clusters and at various sites. In some cases the migration barrier for C atoms is decreased near C atoms, particularly in the same (100) plane. This effect is caused by the straining of the ferrite matrix by the C interstitials. The migration barrier for a single C atom in ferrite is 0.77 eV from one octahedral site to a neighbouring octahedral site, e.g., from site 2 to 3 in Figure 4.1. However moving a C atom from a C-C pair oriented as O-2 in Figure 4.1 to form O-3 has a barrier of 0.58 eV a reduction of almost 25 %. For larger C clusters, e.g., for C atoms at O-2-4 (Fig. 4.1) the barrier for the C atom from site 4 moving away from the site 2 atom along the line defined by their initial positions is 0.42 eV, which is a reduction of 45 %. In general the presence of a C cluster lowers the migration barriers for C atoms within strained planes.

For Nb atoms the opposite is true, as the Nb atoms are significantly larger than Fe atoms the presence of C atoms increases the migration barrier. Using NEB simulation in LAMMPS the migration of a Nb atom to a nearest neighbour (1NN) vacancy is 0.35

C-C Cell size	E_{bind} [eV] static relaxation (LAMMPS) [21, 22]					E_{bind} [eV] DFT		
	3 × 3 ×3	4 × 4 ×4	5 × 5 ×5	10 × 10 ×10	20 × 20 ×20	3 × 3 ×3	4 × 4 ×4	5 × 5 ×5
O-1 [†]	-	-	-	-	<-3.000	-2.027	-1.916	1.863
O-2	-1.256	-1.209	-1.198	-1.189	-1.188	-0.861	-0.775	-0.700
O-3	-0.051	0.016	0.040	0.060	0.062	-0.331	-0.221	-0.118
O-4	0.228	0.294	0.314	0.334	0.335	-0.098	0.030	0.136
O-5	-4.940	-2.296	-1.972	-1.899	-1.892	-3.434	-1.923	-1.655
O-6	0.362	0.347	0.348	0.352	0.352	-0.067	0.005	0.083
O-7	0.168	0.185	0.193	0.201	0.201	-0.112	-0.024	0.058
O-8	-0.374	-0.245	-0.202	-0.170	-0.168	-0.147	-0.006	0.092
O-9	-0.029	0.015	0.037	0.059	0.060	-0.229	-0.118	-0.004
O-10	-0.066	0.000	0.008	0.011	0.010	-0.266	-0.115	-0.029
2-11	-0.069	-0.042	-0.032	-0.021	-0.021	-0.191	-0.026	0.032
2-9	-0.079	-0.035	-0.032	-0.034	-0.034	-0.192	-0.019	0.061
2-10	-0.003	0.030	0.056	0.083	0.084	-0.095	0.035	0.142
3-12	-0.284	-0.199	-0.156	-0.128	-0.127	-0.395	-0.251	-0.131
O-12	-0.051	-0.011	0.016	0.040	0.042	-0.057	-0.006	0.103

Table 4.3: C-C pair binding energies for various C-C pairs illustrated in Figure 4.1, demonstrating the supercell size effect. The DFT values were calculated as part of this work following Section 4.2.2. The LAMMPS results are from the static relaxation calculations. In each column the most favourable (or least unfavourable) pair is marked in bold.

[†] The O-1 pair always relaxes to a 2-11 pair using the MEAM potential.

eV, which is comparable to the migration barrier for Fe atoms to a 1NN vacancy which is 0.47 eV (for DFT data cf. [44]). Note that the vacancy formation energy next to a Nb atom is 0.05 eV lower than in the Fe matrix, i.e., the vacancy is bonded with 0.05 eV (DFT returns 0.35 eV [44]). The migration barrier for a Nb atom at site III near a C-C pair at sites O and 2 (Figure 4.1) to site I is almost tripled at 1.03 eV. Similar increases are observed near larger Nb-C clusters, particularly for the movement of Nb atoms not in the (100) plane of the cluster. It is therefore concluded that Nb atoms do not easily move through C clusters, but rather that they remain on the surface of existing C clusters. This does not mean that the Nb layer remains on top of a C cluster as C atoms can attach from bulk and embed the Nb-rich layer, alternatively C atoms from the cluster can move to embed the Nb atoms.

An exception exists for Nb atoms near a cluster or fluctuation, in the same (100) plane as the cluster or fluctuation. These Nb atoms can have a lowered migration barrier for movement in the [100] direction of the cluster or fluctuation, we found barriers as low as 0.21 eV. Where Nb atoms attach to the edge of a (Fe,Nb)C cluster as this is favourable for the binding energy. Which further validates the in-plane growth of (Fe,Nb)C clusters as described above.

The same effects are witnessed for Ti atoms, but as the Ti atoms are smaller than the Nb atoms in the bcc Fe matrix [33] the effects are weaker.

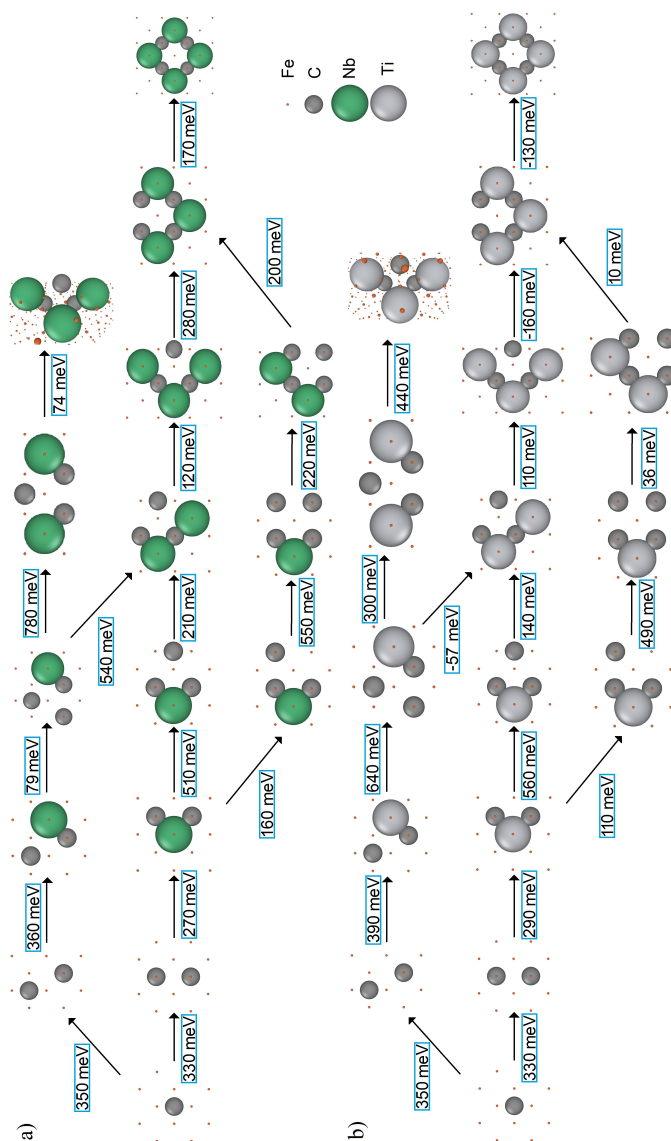


Figure 4.2: Growth path of a M-C cluster in a bcc Fe matrix, calculated with a MEAM potential [21, 22] for static relaxations in LAMMPS. The clusters displayed here all lie within the same (100) plane and can therefore be viewed as 2D clusters (except for the rightmost cluster in the top row, where the C atoms do not lie in the same (100) plane as the Ti atoms). For each added atom the gain in binding energy from the previous cluster is given displaying that there is a path along which each added atom gains additional binding energy for the cluster. Shown clusters are unrelaxed for clarity, however corresponding binding energies are presented for the relaxed clusters. Fe atoms are scaled down for clarity. In a) Nb-C clusters are shown and in b) Ti-C clusters. NB, in MD simulations we observe that the C atoms (for small FeMC_3 clusters) relax slightly out of the (100) plane containing the M atoms, see Figure 4.4c.

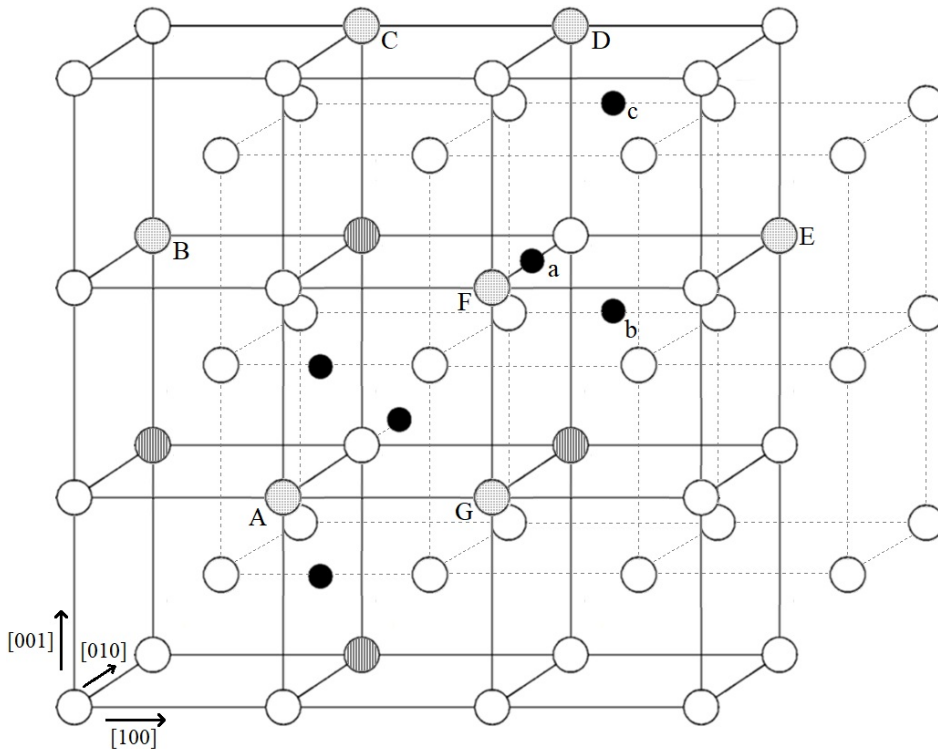


Figure 4.3: The continuation of the growth of clusters shown in Figure 4.2, again the clusters are unrelaxed for clarity. The initial M atoms are given by the striped dark grey bcc sites. The initial C atoms are out-of-M-plane and depicted by the black circles, this displaced form is more stable than what is depicted in Figure 4.2. New M atoms are added at the light grey bcc sites marked by upper case letters, C atoms are added at the black sites labelled with lower case letters.

4.3.2. MOLECULAR DYNAMICS

MD simulations at non-zero temperatures are performed for the Fe-Nb-C ternary system. As the Ti and Nb results are very similar only the results for Nb are presented.

Cluster formation in Fe-Nb-C is simulated in a supercell of $10 \times 10 \times 10$ bcc unit cells. To increase the rate at which clusters can form [45, 46], simulations are performed at somewhat elevated Nb and C concentrations of roughly 0.5 %*at.* and 1 %*at.* The formation of C clusters occurs within a few ns at 1150 K. However only one or two Nb atoms attach to the formed C cluster within the run-time of the simulation, displaying minimal Nb-C cluster formation for various Nb, C, and vacancy concentrations. Note that a vacancy concentration of one vacancy in the $10 \times 10 \times 10$ bcc unit supercell exceeds the equilibrium concentration by a factor of 13600, so even at these vacancy concentrations the simulation time is too short to see cluster formation. The simulated time is 20 ns, but at such vacancy concentrations the number of possible vacancy jumps is much higher than would be possible at the expected vacancy concentration. Therefore a corrected

C and Nb atoms [21]					
Added atom	$\Delta E_{bind.}$ [eV]	Added atom	$\Delta E_{bind.}$ [eV]	Added atom	$\Delta E_{bind.}$ [eV]
a	0.602	a, A	0.510	a, b, c, A	1.939
b	0.190	a, B	0.512	a, b, c, B	1.887
c	-0.294	a, C	0.576	a, b, c, C	2.073
a, b	1.366	a, D	0.793	a, b, c, D	2.257
a, c	0.903	a, E	0.805	a, b, c, E	2.020
b, c	0.434	a, F	-0.349	a, b, c, F	1.197
a, b, c	2.005	a, G	0.642	a, b, c, G	2.006
C and Ti atoms [22]					
Added atom	$\Delta E_{bind.}$ [eV]	Added atom	$\Delta E_{bind.}$ [eV]	Added atom	$\Delta E_{bind.}$ [eV]
a	1.261	a, A	1.222	a, b, c, A	2.879
b	1.116	a, B	1.108	a, b, c, B	2.841
c	0.495	a, C	1.250	a, b, c, C	2.996
a, b	2.195	a, D	1.330	a, b, c, D	3.170
a, c	1.585	a, E	1.340	a, b, c, E	2.856
b, c	1.398	a, F	0.687	a, b, c, F	2.342
a, b, c	2.924	a, G	1.527	a, b, c, G	3.167

Table 4.4: Change in binding energy for atoms added in Figure 4.3 under static relaxation. The C atoms want to attach in the adjacent {100} planes in a pattern shown in Figure 4.3. M atoms continue the checkerboard pattern found in Figure 4.2.

simulated time can be estimated at $13600 \cdot 20$ ns for the cell with 1 vacancy. Here it is noted that the increase in possible jumps mainly occurs for Fe and Nb atoms as they are dependent on vacancies for diffusion, much less so for C atoms which move between octahedral interstitial sites without relying on vacancies in the bcc lattice. This needs to be taken into account if one wishes to adjust the simulated time.

It may be concluded that the formation of Nb-C clusters takes much more than 20 ns even at 1150 K (cf. Hin et al. [45, 46]) making it unpractical for our purposes. The formation of C clusters has been examined experimentally [34–37], the formation of C clusters happens spontaneously as a local ordering effect, where the M atoms can act as anchors for the C atom clusters. These experimental results for C atom clustering are reflected by the MD simulations. The experimentally observed C clusters form in parallel {100} layers [36], while Nb atoms migrate to the surface of C clusters, which provides the basic steps in the formation of a proto-precipitate.

As the focus of this work is on the formation of M-C clusters, which take too long to form in MD simulations, a cluster is constructed, as shown in Figure 4.4a. This constructed cluster is used to assess the stability of the (Fe,M)C cluster, and to study the movement of C atoms around the cluster. The MD simulations are performed at 1150 K. The system is simulated with varying numbers of vacancies, namely 0, 1, and 10. Note that even at 1150 K the expected fraction of vacancies is $e^{-E_{vac}^f/kT} = 3.67 \cdot 10^{-8}$, where E_{vac}^f is the vacancy formation energy in the ferrite matrix which is 1.7 eV for the used potentials [21, 22].

In these simulations it is found that the C atoms in an initial cluster as depicted in

Figure 4.4a move to form a cluster as presented (idealised) in Figure 4.4b and detailed further in Figures 4.4c and d, here the Nb atoms barely move with one vacancy, and still remain somewhat clustered when there are 10 vacancies. This could be a result from vacancies binding to the cluster atoms. In Figures 4.4b-e the Nb-C cluster extends into its adjacent (100) planes as C atoms are placed on top of the (100) plane containing Nb, as we already found in Figure 4.3 and Table 4.4. In fact the C atoms form ‘triangles’ around the Fe atoms in the cluster, as shown in Figures 4.4b-d (also cf. [47]). We note specific features for the M-C cluster:

- The Fe and M atoms form a chequerboard-pattern as shown in Figure 4.4.
- We can distinguish two types of C atoms; i) C lying in ‘rows’ with two C atoms (near a Fe site) on one side of the cluster, and ii) C atoms lying ‘between-rows’. The rows, ideally, lie alternating on both sides of the Fe-M chequerboard pattern situated in a single (100) plane. This is displayed in Figures 4.4c and d.
- Fe atoms in the cluster have three close C neighbours. Two within a ‘row’, the other C atom lies ‘between-rows’. The Fe-C distance is roughly equal for all three C atoms, hence the C atoms form a triangle around the Fe atom. The Fe-C bonds are shown in Figure 4.4c.
- Moreover, the (Fe,M)C cluster found here has a composition of FeMC_3 where the M atoms are outnumbered 1:3 by C atoms. NB. the platelet might contain even more C atoms because the M atoms attach to (larger) C clusters so that the platelet surface is enriched in C.

In the MD simulations (Fe,Nb)C clusters are observed that are coherent with the bcc lattice. The structure of the cluster however differs from the NaCl-structure as described above. The (Fe,M)C cluster has a high Fe and C concentration, these high concentrations are explained by the earlier observation that M atoms are attracted by C clusters. Moreover, the structure of the (Fe,M)C cluster displays an ordering deviating from the NaCl structure, whereas the NaCl-structure is most stable for pure NbC [48], and is observed for larger precipitates [14]. The transformation of the (Fe,M)C cluster to a NaCl structured cluster is studied in [20].

4.3.3. STABILITY OF CLUSTERS AT FINITE TEMPERATURES

IN Section 4.3.1 the initial stage of Fe-M-C clustering has been shown, and in Section 4.3.2 the behaviour of a larger (Fe,M)C cluster at finite temperatures has been investigated where an ordered FeMC_3 cluster is identified as a very stable configuration.

Relaxing clusters at 0 K shows various clusters that have a favourable binding energy, however the stability at finite temperatures remains unknown. To factor in thermal effects an estimate for the change in entropy is made. For the entropy term the configurational term is taken as it is the most dominant contribution and approximated as ideal mixing. Other, e.g., vibrational contributions are collected in a polynomial in the composition as in [49], as the matrix fractions for M and C atoms are small a first-order approximation suffices. Then the other entropy contributions are reduced to a constant excess embedding energy, G_{xs}^{emb} , which is dominated by the ideal mixing entropy, so for

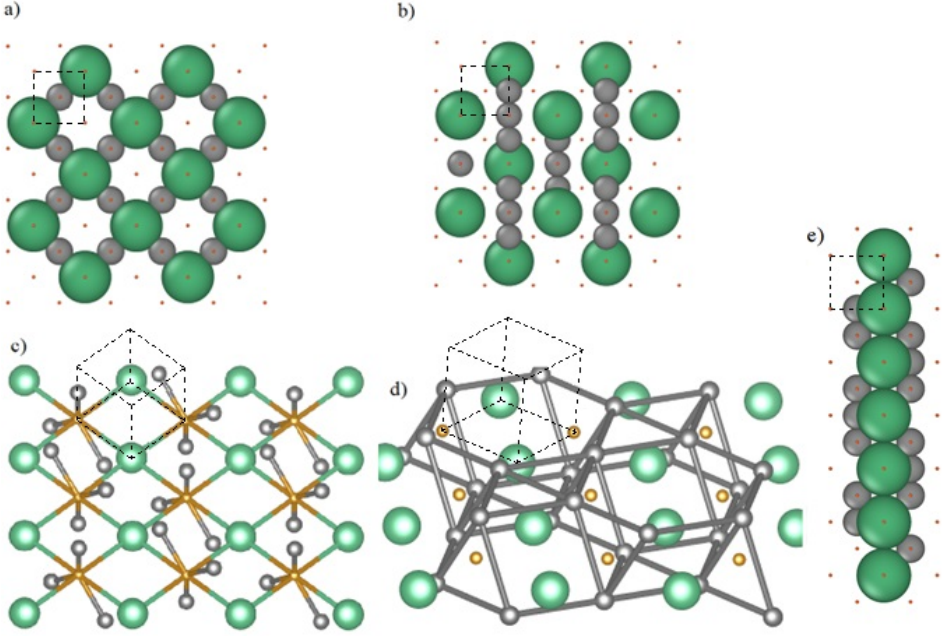


Figure 4.4: a) The initial cluster used in MD simulations. Different colours are used for the various atoms the C atoms are grey, the M atoms are green (largest), and the Fe atoms are brown (smallest). b), c), d) and e) are strongly idealized (and unrelaxed for clarity) version of the most stable cluster as found from MD simulations. In b) a front-view of the cluster is shown, c) the (100) plane in which the Fe and Nb atoms are indicated by the Fe-Nb bonds as well as the C atoms that lie in the adjacent (100) plane indicated by the Fe-C bonds. In d) the C-C bonds shorter than 3.5 Å are depicted, from which the C ‘triangles’ around the Fe atoms are shown. (also cf. supplemental data [47]). Note that the edges of the cluster displayed in Figures b),c), and d) are likely to be ‘decorated’ with more C atoms, an example is given in Figures 4.5b-d. In e) the side of a cluster is shown to demonstrate how the C atoms lie out of the habit plane of the cluster. In each figure the bcc unit cell is outlined by the black dashed lines.

simplicity only the configurational entropy is considered. Then the entropy of the matrix is given as

$$S = k_B \ln(\omega), \quad (4.3)$$

where ω is the number of configurations, and k_B the Boltzmann constant. We define N_{Fe} , N_M , N_{vac} , N_C , N_{vacoct} , as the number of Fe, M, vacancies, C, and vacant octahedral sites respectively. The total number of lattice sites can be defined as \bar{N} where $\bar{N} = N_{Fe} + N_M + N_{vac}$, then $N_C + N_{vacoct} = 3\bar{N}$. Here it is implicitly assumed that Fe and Nb atoms can only occupy bcc lattice sites, and C atoms can only occupy octahedral sites. Then for an ideal mixture:

$$\omega = \frac{\bar{N}!}{N_{Fe}!N_M!N_{vac}!} \cdot \frac{(3\bar{N})!}{N_C!N_{vacoct}!}. \quad (4.4)$$

Now defining the fractions $X_i = N_i / \bar{N}$ for $i \in \{\text{Fe}, \text{M}, \text{vac}\}$, and $Y_j = N_j / (3\bar{N})$ for $j \in \{\text{C}, \text{vacoct}\}$. Using Stirling's approximation it is found that for a system of size \bar{N}

$$\ln(\omega) = -\bar{N} \left(\sum_i X_i \ln(X_i) + 3 \cdot \sum_j Y_j \ln(Y_j) \right). \quad (4.5)$$

For the estimation of the stability of a cluster we compare a system in which all clusters are dissolved, of which $\ln(\omega)$ is given by Equation (4.5), and a system with one cluster consisting of $N_{\text{Fe}}^{\text{cl}}$, N_{M}^{cl} , N_{C}^{cl} , and $N_{\text{vac}}^{\text{cl}}$ sites, the number of Fe, Nb, C, and vacancies in the cluster respectively. Assuming that $\bar{N}^{\text{cl}} = N_{\text{Fe}}^{\text{cl}} + N_{\text{M}}^{\text{cl}} + N_{\text{vac}}^{\text{cl}}$ and that N_{C}^{cl} is small the change in entropy in the matrix is

$$\Delta S^{\text{matrix}} = k \cdot \Delta \ln(\omega) = k \cdot \bar{N}^{\text{cl}} \left(\sum_i X_i \ln(X_i) + 3 \cdot \sum_j Y_j \ln(Y_j) \right). \quad (4.6)$$

Because the cluster is an ordered structure its configurational entropy is assumed to be negligible compared to the entropy change in the matrix. As X_{M} , Y_{C} , and X_{vac} are small, the entropy per alloy atom can be written as

$$S_{\text{M}} = -k \cdot \ln(X_{\text{M}}), \quad S_{\text{C}} = -k \cdot \ln(Y_{\text{C}}), \quad \text{and} \quad S_{\text{vac}} = -k \cdot \ln(X_{\text{vac}}). \quad (4.7)$$

Then for every atom that goes from solid solution to a cluster, the corresponding amount of entropy is lost.

The entropy contribution at a given temperature T can be compared directly to the binding energies found in the static relaxation. This is possible as the concentrations of M and C atoms in micro-alloyed steels are generally quite low (~ 0.05 %_{at.} for M and ~ 0.15 %_{at.} for C). As the concentrations are so low, M and C atoms can be randomly placed in the ferrite matrix (still assuming M atoms only occupy substitutional sites of the bcc lattice, and C atoms occupy octahedral interstitial sites) without interaction. So the energies associated with fully dissolved atoms are good estimates for the mixing enthalpy ΔH_{mix} . The change in free energy due to the forming of a cluster can be written as

$$\begin{aligned} \Delta G &= G^{\text{matrix}} - G^{\text{clus}} = (H^{\text{matrix}} - TS^{\text{matrix}}) - (H^{\text{clus}} - TS^{\text{clus}}) = \\ &= (H^{\text{matrix}} - H^{\text{clus}}) - T\Delta S^{\text{matrix}} \approx E_{\text{bind}} - T\Delta S^{\text{matrix}}. \end{aligned} \quad (4.8)$$

When comparing the binding energy of a cluster to the change in entropy of mixing it is possible to show whether or not it is energetically favourable to form the cluster with respect to the solid solution at the bulk composition at finite temperatures. Note that the existence of more stable clusters with the same number of atoms cannot be excluded.

Applying the Gibbs energy assessment to various clusters shows that there are several M-C clusters that are energetically favourable well into the >1000 K range where MC precipitation is also observed. The stabilising factor lies with the C cluster, which plays a key role in stabilising proto-precipitates. For several clusters T_0 , the ' T_0 -temperature'

where two phases of identical chemical composition have the same Gibbs energy, i.e., the temperature at which $T_0\Delta S = E_{bind}$ is presented in Figure 4.5a. In Figure 4.5a we simulate clusters that use the same ‘triangular’ pattern as presented in Figures 4.4b-d, but now the edges are decorated with C atoms as shown in Figures 4.5b-d (cf. [47]). ‘Decorated’ means that the edges of the clusters, i.e., in the habit plane, are also covered with C atoms.

In Figure 4.5a the M fraction is kept constant at $X_M = 0.0005$ for all supercells, the carbon fraction is fixed at $X_C = 0.0015$. It is noted that the T_0 -temperature for small clusters is lower than for larger clusters, indicating that clusters become more stable with increasing cluster size as the T_0 -temperature increases with cluster size.

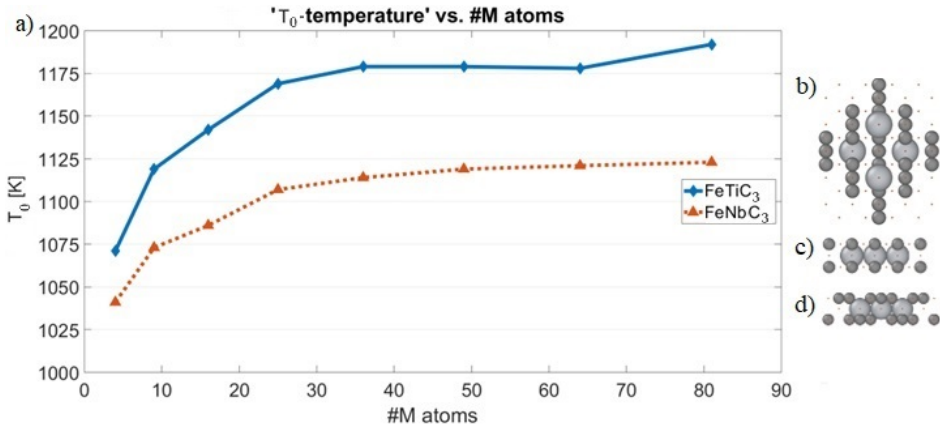


Figure 4.5: a) T_0 -temperature for TiC and NbC clusters calculated using the entropy of mixing from Eq. (4.6). The solid blue line belongs to the (Fe,Ti)C cluster, and the red dotted line belongs to the (Fe,Nb)C cluster. The fraction $X_M = 0.0005$ is fixed, and the C fraction is fixed at $X_C = 0.0015$. The Ti cluster remains energetically favourable up to higher temperatures than the Nb cluster, this is in agreement with the solubility products of the NbC and TiC carbides [50]. In b) the top-view of an (Fe,M)C cluster is given with added excess C atoms, in c) and d) two sides of the (Fe,M)C cluster are presented. The patterns given in b)-d) are extended for the larger clusters.

In Figure 4.5a it can be seen that the FeMC₃ clusters are stable up to approximately 1100 K for FeNbC₃, and 1175K for FeTiC₃. These temperatures are well in the experimental temperature range for which the platelets were observed [5–11]. Note that the ferrite matrix undergoes a phase transformation to austenite (fcc) at 1185 K, so larger Ti-C clusters are nearly always stable in ferrite at typical C and Ti concentrations, i.e., $X_{Ti} \approx 0.0005$ and $X_C \approx 0.0015$.

4.4. FORMATION MECHANISM

FROM simulations both static and dynamic, and the thermodynamic assessment the following hypothesis for a nucleation path is derived:

- Initially C atoms form clusters in the {100} planes of the ferrite matrix through spinodal decomposition, or as a temporal fluctuation. The bcc Fe lattice is strained

around these C clusters. Migration of C atoms in the (100) plane of a cluster is increased as migration barriers are lowered.

- In the strained zone around the C cluster M atoms attach to the surface of C clusters, as there is an attraction between the C cluster and M atoms. M atoms hardly move out of the cluster once attached to a (Fe,M)C cluster due to high migration barriers around the cluster. C atoms can attach to the cluster with favourable effect on the binding energy, thus the Nb-rich layer can be embedded in a C cluster. Both processes occur simultaneously where growth of the cluster is favoured in a single (100) plane.

In this process of M atoms attaching to the cluster a FeMC_3 cluster is formed. Clusters can form containing as little as two or three M atoms. Such proto-precipitates have a diameter less than 1 nm.

The formation of FeMC_3 clusters presents a precursor stage to the formation of NaCl-structured platelets. The mechanism found in this work presents an atomistic picture describing the processes that lead to the formation of the nano-precipitates (platelets) found in experiments [5–11]. However the carbon content of the clusters, found in the simulations, is outnumbering M atoms 3:1. Some factors may contribute to this high carbon content.

We note that C atoms may form clusters through temporal fluctuations in ferrite, but the formation of C-rich zones may also occur in austenite [51–53]. The formation of a M-C cluster pins part of the C atoms in a carbide precipitate. Contrary to [10] we find that the formation of C fluctuations occurs first and possibly preferentially near M atoms. We observe that the M atoms are attracted to C clusters to form proto-precipitates. Some C-rich layers found in spinodal decomposition [38] could attract M atoms and be stabilised to form FeMC_3 clusters. We find that carbides form at sites where C atoms accumulate and form clusters, despite the fact that M atoms are generally less mobile than C atoms. This effect, where the C atoms determine the position of the precipitate rather than the M atoms, was previously observed in Monte-Carlo simulations [45, 46]. Following the cluster formation path found in this work, this counter-intuitive result is explained by the fact that M atoms are inclined to attach to C clusters, rather than form independent M clusters.

We have shown that the formation of M-C clusters encompasses several steps. Firstly the fluctuation of C atoms in ferrite forms rapidly evolving C clusters in the {100} planes of the ferrite matrix [34–38]. Secondly M atoms attach to the C clusters, as is shown by the favourable binding energies. The M atoms thereby play a stabilising role on the C fluctuations by forming a M-C cluster. Alternately, the C clusters and fluctuations are more likely to occur near M atoms. Moreover, clusters attract vacancies [20], and the Nb (or Ti) migration energy is lowered in a (100) plane in which a cluster is situated.

The M-C clusters lie in the {100} planes of the ferrite matrix like the C clusters, and they form in a single (100) plane. The initial M-C clusters contain a large fraction of Fe and C atoms with a FeMC_3 stoichiometry. The FeMC_3 cluster has a structure where the C atoms do not lie in the NaCl-structure sites, but they rather form a structure where 2/3 of the C atoms align in 'rows' alternating between either surface of the cluster and the

adjacent Fe lattice planes. The remaining C atoms lie directly between these ‘rows’.

4.5. CONCLUSION

FORMATION of M-carbides encompasses different stages. Before the actual formation of a M-C cluster C atoms form clusters in the {100} planes of the ferrite matrix as a result of fluctuations. Unto these C clusters M atoms attach to form ordered Fe-M-C clusters with a composition FeMC_{3+x} , also directed in the [100] directions of the ferrite matrix. The M atoms in a FeMC_{3+x} cluster lie within a single (100) plane, where they form a chequerboard pattern together with Fe atoms. The origins of this chequerboard pattern seem to lie in the pair interactions between the M atoms which is particularly pronounced in DFT calculations.

Growth simulations reveal a stable FeMC_3 proto-precipitate and MD simulations show that at elevated temperatures it remains coherent with the ferrite matrix. At common matrix fractions, $X_{\text{Nb(or Ti)}} \approx 0.0005$ and $X_C \approx 0.0015$, the FeNbC_3 clusters are stable in the 1100 K range, and the FeTiC_3 clusters remain stable near 1185 K which is the ferrite-austenite transition temperature.

Hence the FeMC_3 proto-precipitates found in this study represent a very plausible precursor to MC nano-precipitate carbides.

REFERENCES

- [1] R. J. Slooter, M. H. F. Sluiter, W. G. T. Kranendonk, and C. Bos. Atomistic simulation of carbide formation in ferrite. *Computational Materials Science*, 230:112455, 2023.
- [2] R. J. Slooter, M. H. F. Sluiter, W. G. T. Kranendonk, and C. Bos. Investigation of NbC proto-nuclei in steel. In *CALPHAD 2022*, 2022.
- [3] P. A. Manohar, M. Ferry, and T. Chandra. Five decades of the Zener equation. *ISIJ international*, 38(9):913–924, 1998.
- [4] E. Nes, N. Ryum, and O. Hunderi. On the Zener drag. *Acta metallurgica*, 33(1):11–22, 1985.
- [5] E. Courtois, T. Epicier, and C. Scott. Characterisation of niobium carbide and carbonitride evolution within ferrite: contribution of transmission electron microscopy and advanced associated techniques. *Materials Science Forum*, 500-501:669–676, 2005.
- [6] A. J. Breen, K. Y. Xie, M. P. Moody, B. Gault, H.-W. Yen, C. C. Wong, J. M. Cairney, and S. P. Ringer. Resolving the morphology of niobium carbonitride nano-precipitates in steel using atom probe tomography. *Microscopy and microanalysis*, 20:1100–1110, 2014.
- [7] J. Takahashi, K. Kawakami, and Y. Kobayashi. Origin of hydrogen trapping site in vanadium carbide precipitation strengthening steel. *Acta materialia*, 153:193–204, 2018.

- [8] J. Wang, M. Weyland, I. Bikmukhametov, M. K. Miller, P. D. Hodgson, and I. Timokhina. Transformation from cluster to nano-precipitate in microalloyed ferritic steel. *Scripta materialia*, 160:53–57, 2019.
- [9] F. Danoix, T. Epicier, F. Vurpillot, and D. Blavette. Atomic-scale imaging and analysis of single layer GP zones in a model steel. *Journal of material science*, 47:1567–1571, 2012.
- [10] T. Furuhashi, Y. Zhang, M. Sato, G. Miyamoto, M. Enoki, H. Ohtani, T. Uesugi, and H. Numakura. Sublattice alloy design of high-strength steels: Application of clustering and nanoscale precipitation of interstitial and substitutional solutes. *Scripta Materialia*, 223:115063, 2023.
- [11] S. Taniguchi, G. Shigesato, and M. Sugiyama. Atomic resolution scanning transmission electron microscopy of TiC precipitates in low carbon ferritic steels. *ISIJ International*, 62(5):984–991, 2022.
- [12] R. G. Baker and J. Nutting. The tempering of Cr-Mo-V-W and Mo-V steel precipitation processes in steels. *ISI Special Report*, 64:1–12, 1969.
- [13] C. Ioannidou, A. Navarro-López, A. Rijkenberg, R. M. Dalgliesh, S. Koelling, C. Pappas, J. Sietsma, A. A. van Well, and S. E. Offerman. Evolution of the precipitate composition during annealing of vanadium micro-alloyed steels by in-situ SANS. *Acta Materialia*, 201:217–230, 2020.
- [14] R. Shi, Y. Ma, Z. Wang, L. Gao, X.-S. Yang, L. Qiao, and X. Pang. Atomic-scale investigation of deep hydrogen trapping in NbC/ α -Fe semi-coherent interfaces. *Acta Materialia*, 200:686–698, 2020.
- [15] A. P. Thompson, H. M. Aktulga, R. Berger, D. S. Bolintineanu, W. M. Brown, P. S. Crozier, P. J. in 't Veld, A. Kohlmeyer, S. G. Moore, T. D. Nguyen, R. Shan, M. J. Stevens, J. Tranchida, C. Trott, and S. J. Plimpton. LAMMPS - a flexible simulation tool for particle-based materials modeling at the atomic, meso, and continuum scales. *Computer Physics Communications*, 271:108171, 2022.
- [16] M. Volmer and A. Weber. Keimbildung in übersättigten Gebilden. *Zeitschrift für Physikalische Chemie*, 119:277–301, 1926.
- [17] R. Becker and W. Döring. Kinetische Behandlung der Keimbildung in übersättigten Dämpfen. *Annalen der Physik*, 416(8):719, 1935.
- [18] R. Kampmann and R. Wagner. Kinetics of precipitation in metastable binary alloys - Theory and application to Cu-1.9 at% Ti and Ni 14 at% Al. In P. Haasen, V. Gerold, R. Wagner, and M. F. Ashby, editors, *Decomposition of alloys: the early stages: proceedings of the 2nd acta-scripta metallurgica conference*, number 2 in 2. Acta metallurgica, Pergamon press, 1984.
- [19] M. Perez, M. Dumont, and D. Acevedo-Reyes. Implementation of classical nucleation and growth theories for precipitation. *Acta materialia*, 56:2119–2132, March 2008.

- [20] R. J. Slooter, M. H. F. Sluiter, W. G. T. Kranendonk, and C. Bos. Formation and growth of transition metal carbides in ferrite. *Computational Materials Science*, 242:113097, 2024.
- [21] H.-K. Kim, W.-S. Jung, and B.-J. Lee. Modified embedded-atom method interatomic potentials for the Nb-C, Nb-N, Fe-Nb-C, and Fe-Nb-N systems. *Journal for material research*, 25(7):1288–1297, 2010.
- [22] H.-K. Kim, W.-S. Jung, and B.-J. Lee. Modified embedded-atom method interatomic potential for the Fe-Ti-C and Fe-Ti-N ternary systems. *Acta materialia*, 57:3140–3147, 2009.
- [23] H. Jónsson, G. Mills, and K. W. Jacobsen. Nudged elastic band method for finding minimum energy paths of transitions. In B. J. Berne, G. Ciccotti, and D. F. Coker, editors, *Classical and quantum dynamics in condensed phase simulations*, pages 385–404. World Scientific, 1998.
- [24] G. Kresse and J. Hafner. *Ab initio* molecular dynamics for liquid metals. *Physical Review B*, 47:558(R), 1993.
- [25] G. Kresse and J. Hafner. *Ab initio* molecular-dynamics simulation of the liquid-metal-amorphous-semiconductor transition in germanium. *Physical Review B*, 49:14251–14269, 1994.
- [26] G. Kresse and J. Furthmüller. Efficiency of *ab-initio* total energy calculations for metals and semiconductors using a plane-wave basis set. *Computational Materials Science*, 6:15–50, 1996.
- [27] G. Kresse and J. Furthmüller. Efficient iterative schemes for *ab initio* total-energy calculations using a plane-wave basis set. *Physical Review B*, 54:11169–11186, 1996.
- [28] G. Kresse and D. Joubert. From ultrasoft pseudopotentials to the projector augmented-wave method. *Physical Review B*, 59:1758–1775, 1999.
- [29] H. Sawada, S. Taniguchi, K. Kawakami, and T. Ozaki. First-principles study of interface structure and energy of Fe/NbC. *Modelling and simulation in materials science and engineering*, 21(4):045012, 2013.
- [30] H. Sawada, S. Taniguchi, K. Kawakami, and T. Ozaki. Transition of the interface between iron and carbide precipitate from coherent to semi-coherent. *Metals*, 7:277–289, 2017.
- [31] C. Simonovic, C. K. Ande, A. I. Duff, F. Syahputra, and M. H. F. Sluiter. Diffusion of carbon in bcc Fe in the presence of Si. *Physical Review B*, 81:054116, 2010.
- [32] N. W. Ashcroft and N. D. Mermin. *Solid state physics*. Brooks/Cole, 1976.
- [33] C. K. Ande and M. H. F. Sluiter. First-principles calculations on stabilization of iron carbides (Fe_3C , Fe_5C_2 , and $\eta\text{-Fe}_2\text{C}$) in steels by common alloying elements. *Metalurgical and materials transactions A*, 43:4436–4444, 2012.

- [34] A. M. Sherman, G. T. Eldis, and M. Cohen. The aging and tempering of iron-nickel-carbon martensites. *Metallurgical Transactions A*, 14:995–1005, 1983.
- [35] K. A. Taylor, G. B. Olson, M. Cohen, and J. B. van der Sande. Carbide precipitation during stage I tempering of Fe-Ni-C martensites. *Metallurgical Transactions A*, 20:2749–2765, 1989.
- [36] R. Rementeria, C. Capdevila, R. Domínguez-Reyes, J. D. Poplawsky, W. Guo, E. Urones-Garrote, C. Garcia-Mateo, and F. G. Caballero. Carbon clustering in low-temperature bainite. *Metallurgical and Materials Transactions A*, 49:5277–5287, 2018.
- [37] S. Allain, F. Danoix, M. Goune, K. Hoummada, and D. Mangelinck. Static and dynamical ageing processes at room temperature in a Fe₂₅Ni_{0.4}C virgin martensite: effect of C redistribution at the nanoscale. *Philosophical Magazine Letters*, 93(2):68–76, 2013.
- [38] P. Maugis, F. Danoix, M. Dumont, S. Curelea, S. Cazottes, H. Zapolsky, and M. Gouné. Carbon diffusivity and kinetics of spinodal decomposition of martensite in a model Fe-Ni-C alloy. *Materials letters*, 214:213–216, 2018.
- [39] S. Chentouf, S. Cazottes, F. Danoix, M. Gouné, H. Zapolsky, and P. Maugis. Effect of interstitial carbon distribution and nickel substitution on the tetragonality of martensite: A first-principles study. *Intermetallics*, 89:92–99, 2017.
- [40] D. Kandaskalov and P. Maugis. A first-principles study of the structural, elastic, lattice dynamical and thermodynamic properties of α'' -Fe₁₆C₂ and α'' -Fe₁₆N₂ phases. *Computational materials science*, 128:278–286, 2017.
- [41] D. Kandaskalov and P. Maugis. Thermodynamics stabilities in the Fe-Fe₁₆C₂ system: Influence of carbon-carbon interactions studied by DFT. *Computational materials science*, 150:524–534, 2018.
- [42] J. Xu, C. T. Liu, M. K. Miller, and H. Chen. Nanocluster-associated vacancies in nanocluster-strengthened ferritic steel as seen via positron-lifetime spectroscopy. *Physical Review B*, 79:020204(R), 2009.
- [43] B.-J. Lee. A modified embedded-atom method interatomic potential for the Fe-C system. *Acta Materialia*, 54:701–711, 2006.
- [44] C. D. Versteyleen, N. H. van Dijk, and M. H. F. Sluiter. First-principles analysis of solute diffusion in dilute bcc Fe-X alloys. *Physical Review B*, 96:094105, 2017.
- [45] C. Hin, Y. Bréchet, P. Maugis, and F. Soisson. Kinetics of heterogeneous dislocation precipitation of NbC in alpha-iron. *Acta Materialia*, 56:5535–5543, 2008.
- [46] C. Hin, Y. Bréchet, P. Maugis, and F. Soisson. Kinetics of heterogeneous grain boundary precipitation of NbC in α -iron: A Monte Carlo study. *Acta Materialia*, 56:5653–5667, 2008.

- [47] R. J. Slooter, M. H. F. Sluiter, W. G. T. Kranendonk, and C. Bos. Supplemental data.
- [48] M. H. F. Sluiter. Phase stability of carbides and nitrides in steel. In *Materials research society symposia proceedings*, volume 979, 2006.
- [49] T. Klymko and M. H. F. Sluiter. Computing solubility products using ab initio methods. *Journal of Materials Science*, 47:7601–7614, 2012.
- [50] X.-W. Lei, D.-Y. Li, X.-H. Zhang, and T.-X. Liang. Effect of solid solution elements on solubility products of carbides and nitrides in ferrite thermodynamic calculations. *Metallurgical and Materials Transactions A*, 50(6):2978–2990, 2019.
- [51] M. K. Kang, Y. Q. Yang, Q. M. Wei, Q. M. Yang, and X. K. Meng. On the prebainitic phenomenon in some alloys. *Metallurgical and Materials Transactions A*, 25:1941–1946, 1994.
- [52] X. L. Wu, X. Y. Zhang, X. K. Meng, M. K. Kang, and Y. Q. Yang. Formation of carbon-poor regions during pre-bainitic transformation. *Materials Letters*, 22:141–144, 1995.
- [53] Q. Luo, M. Kitchen, and S. Abubakri. Effect of austempering time on the microstructure and carbon partitioning of ultrahigh strength steel 56NiCrMoV7. *Metals*, 7:258–272, 2017.

5

FORMATION AND GROWTH OF TRANSITION METAL CARBIDES IN FERRITE

The naturalest way is the best way.

Charles Dickens

If the iron be blunt, and he do not whet the edge, then must he put to more strength: but wisdom is profitable to direct.

Ecclesiastes 10:10

Carbide nano-precipitates are commonly used to improve mechanical properties of steel. It has been experimentally observed for TiC, NbC, and VC that carbide precipitates form as 'plate-like' particles oriented in the {100} planes of the ferrite lattice. These platelets share similarities with Guinier-Preston zones in Al-Cu alloys.

The clustering of group IV and V transition metal atoms ($M = \text{Ti, Zr, Hf, V, Nb, Ta}$) in ferrite is studied using density functional theory. It is deduced that the transition metal carbides all form in a similar way. Furthermore, the transition from an initial M-C cluster to a NaCl-structured precipitate is examined through atomistic simulations using Modified Embedded Atom Method potentials. A route is established along which transition metal carbides form and transform into precipitates that possess the Baker-Nutting orientation relation with the ferrite matrix.

The contents of this chapter have been published in *Computational Materials Science* [1], and parts were presented at CALPHAD XLIX [2].

5.1. INTRODUCTION

NANO-precipitates perform a key role to increase the mechanical hardness of microalloyed steels. The number and size-distribution of precipitates are commonly modelled using classical nucleation and growth theory (CNGT) [3–6]. These CNGT models provide a good insight in average precipitation behaviour. Conventional CNGT treats the formation of precipitates as compact particles with regular shapes, such as spheres, ellipsoids, cubes, etc. Furthermore, CNGT does not account for the variation of properties, such as composition, among precipitates of different sizes. However, transmission electron microscopy (TEM) reveals that various carbides in the bcc-Fe (α) matrix are not compact particles, rather they grow initially as platelets in {100}-planes of the bcc-Fe matrix [7–10], that evolve to spheroids as they grow larger. Moreover, the stoichiometry of metal carbides ‘MC’ (where M = Ti, V, or Nb) is found to be size dependent [8, 10–12]. Previous simulations for NbC and TiC [13] have demonstrated that the formation of MC precipitates involves a precursor state. Both simulations and experiments suggest that this precursor state is akin to a ‘Guinier-Preston’ (GP)-like zone [10, 13], which eventually transforms into the final NaCl-structured MC precipitate.

In the same study [13] the precursor stage for Nb and Ti carbides is found to have an ordered FeMC_3 structure, stable up to the 1100 K range. Relations between the binding energies of M-M and M-C pairs embedded in ferrite and the nature of the cluster, where Fe and M atoms initially form a checkerboard pattern, were identified from simulations using Modified Embedded Atom Method (MEAM) [14, 15] potentials and from Density Functional Theory (DFT) calculations. In this work the study of these pairs is expanded for multiple group IV and group V transition metals. Similarities are identified between Ti, Zr, Hf, V, Nb, and Ta behaviour in ferrite. As for most transition metals there is no available MEAM potential (where M = Ti, Zr, Hf, V, Nb, Ta) we perform DFT calculations on multiple M-M and M-C pairs. Additionally some M-M-M triplets are calculated. From these DFT calculations we find that all the corresponding MC carbides seem to form via the same mechanism, where the MC carbides form a precursor stage with its M atoms in a single $(100)_\alpha$ plane of the ferrite matrix.

Our previous study [13]¹ also shows that the precursor stage FeMC_3 clusters do not have the NaCl-structure that is observed for larger precipitates, and which is known to be the most stable bulk structure [16]. The FeMC_3 clusters rather display a checkerboard pattern for the Fe and M atoms in a single $(100)_\alpha$ plane. The transformation of a FeMC_3 cluster to a NaCl-structured platelet is studied here using MEAM [14, 15] potentials in LAMMPS [17]. Various steps in the transformation are identified, where the FeMC_3 cluster displays similarities in behaviour to the GP zone in aluminium alloys. The attraction of vacancies to the cluster occurs in the same manner as the GP zone in aluminium alloys [18], where vacancies aid transport of precipitate forming atoms toward the GP zone as vacancies are bound to the M atoms. In the simulations the role of vacancies and their interaction with the FeMC_3 clusters are also studied. Using atomistic simulations the main driving force behind the transformation from the initial cluster to the NaCl-structured platelet has been investigated. It is established that the main driving force is the strain in the planes perpendicular to the habit plane of the initial cluster.

¹Which is included in Chapter 4.

First the methodology is presented in Section 5.2, then in Section 5.3 the results of the DFT calculations are presented and discussed. In Section 5.4 the transformation mechanism is studied and discussed.

5.2. METHODOLOGY

5.2.1. INTRODUCTION

IN this work both DFT calculations and MEAM LAMMPS simulations are performed. The DFT calculations are used for small systems in which a pair of M atoms, or a pair consisting of a M atom and a C atom is embedded in ferrite. This shows whether the formation of a specific pair is energetically favourable compared to fully dissolved atoms, i.e., in the infinitely diluted limit. These calculations show how initial clusters can form from the solid solution. As DFT calculations are computationally demanding only small supercells are constructed.

For larger systems LAMMPS is used to perform atomistic simulations on FeMC₃ clusters. The atomistic simulations are specifically used to establish how a FeMC₃ cluster can transform to a NaCl-structured platelet and eventually a multilayered NaCl-structured precipitate.

5.2.2. DFT-CALCULATIONS

THE DFT calculations were performed using projector-augmented wave (PAW) pseudo potentials as implemented in the Vienna Ab initio Simulation Package (VASP version 5.3.5) [19–23].

For both M-M and M-C pairs the binding energy E_{bind} at 0 K is investigated where a positive value indicates attraction and a negative energy indicates repulsion. The binding energy is defined as:

$$E_{bind} = iE(Fe) + j\Delta E(M) + k\Delta E(C) - E(Fe_iM_jC_k), \quad (5.1)$$

where $\Delta E(X)$, with $X = M, C$, is the solute excess energy given by:

$$\Delta E(X) = E(Fe_iX) - iE(Fe). \quad (5.2)$$

Here $E(Y)$ is the total energy of a supercell containing Y (where $Y = Fe_pM_qC_r$). Each supercell contains a bcc lattice, the average lattice parameter is fixed at 2.833 Å which is the equilibrium lattice parameter for pure bcc Fe, hereby also fixing the supercell volume.

For different M-M, and M-C pairs embedded in bcc Fe a simulation is performed in a $3 \times 3 \times 3$ unit bcc and a $4 \times 4 \times 4$ bcc unit supercell, containing 54 and 128 substitutional atom sites respectively. For the $3 \times 3 \times 3$ supercell we use 6 k-points along all axes, the k-points are arranged following a regular Γ -centered mesh. The electronic wave functions are expanded in terms of plane waves, for all supercells a cut-off kinetic energy set at 400 eV was used. For the $4 \times 4 \times 4$ supercell we use 4 k-points along all axes, again using the regular Γ -centered mesh. For both the $3 \times 3 \times 3$ bcc unit and $4 \times 4 \times 4$ bcc unit supercell the precision is set to medium. The structural relaxation convergence criterium for energy is that the total energy change between subsequent ionic iterations is smaller than 0.1

meV, and for forces that the norms of each force is smaller than 100 meV/nm.

Additionally some pairs are also simulated in a $5 \times 5 \times 5$ bcc unit supercell, containing 250 substitutional atom sites. Apart from the supercell size the same settings as for the $4 \times 4 \times 4$ bcc unit supercell are used. Again 4 k-points were used following a regular Γ -centred mesh.

5.2.3. LAMMPS SIMULATIONS FOR THE TRANSFORMATION MECHANISM

THE transformation from initial M-C clusters to a NaCl-structure is studied using Modified embedded atom method (MEAM) potentials in LAMMPS (v 3mar20) [17]. In these simulations the MEAM potentials for the Fe-Nb-C [15] and Fe-Ti-C [14] ternary systems are used.

First the solute excess energy for a C atom at an octahedral interstitial site is established using Eq. (5.2), as well as the solute excess energy for replacing an Fe atom with a M (= Nb,Ti) atom. Using these solute excess energies the binding energies can be calculated for the various clusters using Eq. (5.1). Here it is explicitly assumed that C atoms only occupy octahedral interstitial sites, and M atoms only occupy substitutional sites on the bcc lattice. The initial clusters are of a FeMC_3 type, as presented in [13]. Note that the (total) binding energy contains both a chemical energy and an elastic energy component.

Clusters are simulated in a $20 \times 20 \times 20$ or a $40 \times 40 \times 20$ bcc unit cell supercell, where the supercell-size effects are negligible as the results for a cluster between the two supercells differ less than 0.01 eV/atom for the M and C atoms within the cluster. A constant volume is used where we use the equilibrium lattice parameter, $a=2.8636 \text{ \AA}$, for bcc Fe from the MEAM potentials [14, 15]. The relaxations are performed at 0 K, where the stopping criteria are set such that the energy change between iterations is $1 \cdot 10^{-8}$ eV, for forces the 2-norm of the global force vector must be less than 100 meV/nm, i.e., no force component on any atom is larger than 100 meV/nm. To illustrate the transformation from an FeMC_3 cluster to a NaCl-structured precipitate clearly, clusters with a square shape are used. However, the effects presented in Section 5.4 also hold true for simulations performed with both rectangular and more circular clusters.

5.3. FORMATION OF TRANSITION METAL CLUSTERS

5.3.1. DFT CALCULATIONS FOR THE FORMATION OF TRANSITION METAL CLUSTERS IN FERRITE

TO investigate the general trends in metal-carbide formation DFT calculations are performed for group IV and V transition metals embedded in a bcc iron lattice. Various M-M, M-C pair configurations are simulated: Figure 5.1 gives a schematic overview of the pair configurations. The simulated pairs are chosen to include several close pairs that would exist in the NaCl-structure or the FeMC_3 clusters found in [13].

The M-M pair configurations are labelled by their occupied sites indicated by Roman numerals in Figure 5.1, where all other bcc lattice sites are occupied by Fe atoms. For the M-C pair configurations a M atom is located at the site indicated by a Roman numeral, and a C atom at the integer numbered site. Note that the I-VII M-M pair in the $3 \times 3 \times 3$ bcc unit supercell also contains the I-II pair for periodic boundaries, so it is not included

in the results. The calculated binding energies for group IV metals are presented in Table 5.1, and for the group V metals in Table 5.2.

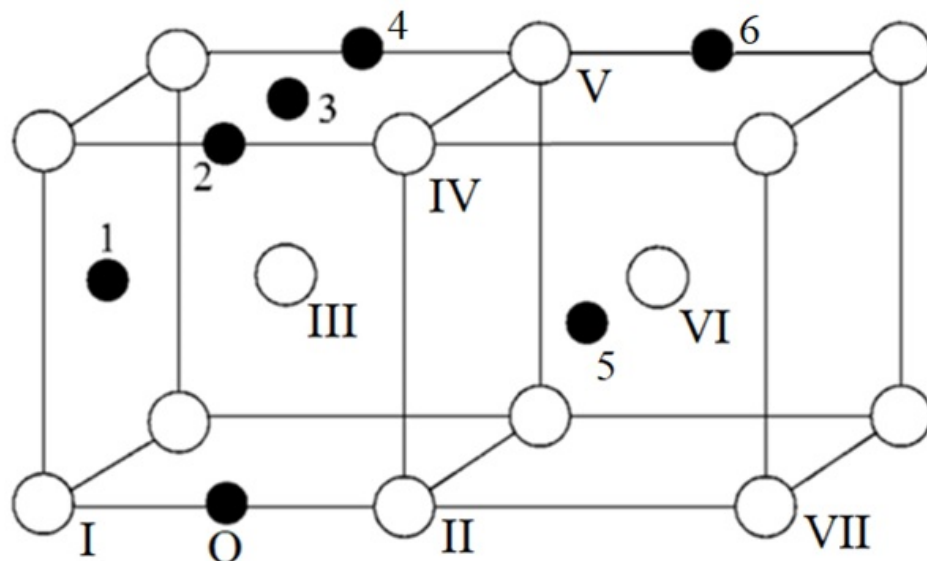


Figure 5.1: Positions of atom pairs, each pair is labelled by the sites the M or C atoms occupy. Corresponding binding energies are given in Tables 5.1 and 5.2. M atoms are placed at the sites with Roman numerals, and C atoms are placed at the integer numbered sites.

For the pairs given in Tables 5.1 and 5.2 the same trend is seen for the binding energy, again a positive value indicates attraction and a negative energy indicates repulsion. We remark that the change from a $3 \times 3 \times 3$ unit cell to a $4 \times 4 \times 4$ unit cell supercell largely preserves the order of favourability of the pairs. Additionally the change in M-M pair binding energies is less than 0.05 eV in most cases, for M-C pairs the change is less than 0.25 eV with one exception, namely the I-5 pair for vanadium. Given that the magnitude of the changes is largely similar within each species we do not expect significant changes in the order of favourability when using a larger supercell.

It must be noted that the binding energies of the least unfavourable pairs in the group V transition metals are only slightly negative. Therefore the I-IV and I-V M-M pairs are simulated again in a $5 \times 5 \times 5$ bcc unit cell sized supercell to see if the pairs are really repulsive or in fact attractive. As in a larger supercell the supercell-size effect caused by the boundaries is reduced for the relaxation, the relaxations are performed at constant volume from an initially 'perfect' bcc lattice.

In Tables 5.1-5.3 it is shown that generally the I-IV pair is the most favourable for M-M pairs, however for Ti and V the I-V pair is slightly more favourable than the I-IV pair. The most favourable M-C pair is the I-2 pair for all metals except vanadium for the $4 \times 4 \times 4$ supercell. There are some differences between the two groups of transition metals. Within the group IV metals attractive interactions are stronger, both for M-M pairs and M-C pairs, than in the group V metals.

Supercell size	Ti		Zr		Hf	
	3 × 3 × 3	4 × 4 × 4	3 × 3 × 3	4 × 4 × 4	3 × 3 × 3	4 × 4 × 4
M-M pairs						
I-II	-0.143	-0.136	-0.216	-0.126	-0.128	-0.128
I-III	-0.237	-0.249	-0.449	-0.365	-0.453	-0.448
I-IV	0.007	-0.009	-0.043	0.025	0.025	0.018
I-V	0.019	0.011	-0.126	-0.049	-0.054	-0.051
I-VI	-0.047	-0.024	-0.114	-0.033	-0.108	-0.032
I-VII	-	-0.017	-	-0.015	-	-0.009
M-C pairs						
I-0	-0.817	-0.728	-1.578	-1.365	-1.484	-1.309
I-1	0.012	0.038	0.011	0.094	0.057	0.101
I-2	-0.022	0.103	-0.041	0.179	-0.004	0.174
I-3	-0.150	-0.027	-0.325	-0.092	-0.278	-0.094
I-4	-0.090	0.033	-0.186	0.023	-0.133	0.031
I-5	-0.080	0.041	-0.135	0.052	-0.091	0.057

Table 5.1: Binding energies for various M-M and M-C pairs for group IV transition metals. The pairs indicated are illustrated in Figure 5.1, all binding energies are given in eV. The binding energy for the most favourable (or least unfavourable) M-M pair, and M-C pair is printed bold.

Supercell size	V		Nb		Ta	
	3 × 3 × 3	4 × 4 × 4	3 × 3 × 3	4 × 4 × 4	3 × 3 × 3	4 × 4 × 4
M-M pairs						
I-II	-0.145	-0.125	-0.216	-0.170	-0.210	-0.164
I-III	-0.259	-0.239	-0.402	-0.393	-0.470	-0.449
I-IV	-0.012	-0.023	-0.016	-0.006	-0.019	-0.008
I-V	-0.019	-0.012	-0.053	-0.053	-0.059	-0.049
I-VI	-0.062	-0.033	-0.080	-0.040	-0.098	-0.044
I-VII	-	-0.036	-	-0.034	-	-0.028
M-C pairs						
I-0	-0.528	-0.479	-1.366	-1.209	-1.353	-1.195
I-1	-0.162	-0.139	-0.108	-0.059	-0.125	-0.074
I-2	-0.114	-0.001	-0.103	0.070	-0.115	0.054
I-3	-0.122	-0.014	-0.271	-0.097	-0.272	-0.094
I-4	-0.096	0.010	-0.142	0.018	-0.138	0.025
I-5	-0.393	0.015	-0.123	0.023	-0.127	0.031

Table 5.2: Binding energies for various M-M and M-C pairs for group V transition metals. The pairs indicated are illustrated in Figure 5.1, all binding energies are given in eV. The binding energy for the most favourable (or least unfavourable) M-M pair, and M-C pair is printed bold.

Ti and V atoms behave different from the other metals, this is most likely a result of the size difference. The Ti and V atoms are both considerably smaller than the other M atoms in the same group when embedded in the ferrite matrix, so they have a better fit with the ferrite matrix [24]. This is also reflected by their comparatively low repulsion in

	Ti	Zr	Hf	V	Nb	Ta
M-M pairs						
I-II	-0.160	-0.089	-0.095	-0.169	-0.148	-0.138
I-IV	-0.016	0.069	0.065	-0.039	0.026	0.024
I-V	0.010	0.029	0.004	-0.038	-0.004	-0.001
M-C pairs						
I-1	0.093	0.168	0.178	-0.092	0.018	0.005
I-2	0.128	0.208	0.207	0.007	0.102	0.091

Table 5.3: Binding energies for the most favourable (or least unfavourable) M-M and M-C pairs in Tables 5.1 and 5.2. Here a $5 \times 5 \times 5$ bcc unit cell sized supercell is used to allow for better relaxation and less influence from the supercell boundaries. The binding energy for the most favourable (or least unfavourable) pairs are printed bold.

the I-III M-M pair and the I-0 M-C pair. The size effect is also visible when comparing the lattice parameters of the various MC carbides, where the TiC and VC lattice parameter is smaller than for the other carbides which are relatively comparable [25].

In short, from the pair interactions we see two main contributions, elastic interaction contribution which derives from the atomic size differences with other substitutional atoms [24], and a chemical interaction contribution. The chemical contribution is observed from the differences between group IV and V transition metals, as there are noticeable differences between the calculated trends for both groups.

For the M-M and M-C pairs all metals display a roughly similar behaviour for their pair interactions embedded in ferrite. This is true for M-C pairs in particular. In [13] the pair interactions for Ti and Nb atoms have been linked to the formation of a checkerboard pattern consisting of Fe and M atoms within a {100} plane, where the M and Fe atoms form an ordered cluster together with C atoms. As all the studied metals display the same (un)favourable interactions for studied pairs and triplets it is plausible that all their carbides form via a similar path, like the path found in [13]. However, it cannot be ruled out that different, more favourable, paths for Zr, Hf, V, and Ta carbides exist.

For further examination two M-C-C triplets are also of particular interest, as they had highly favourable binding energies in the simulations performed in [13]. Besides the M-C-C triplet several M-M-M triplets are studied to see which orientation is preferred, or least unfavourable. Results are given in Table 5.4. The results show that the M-M-M triplets in a single {100} plane are least unfavourable for all metals except for Ti and V. Furthermore the binding energies of the pairs that make up I-IV-VII and I-V-VII are roughly equal to the binding energy of the triplet, from this we deduce that the pair interactions provide a good first approximation for the binding energy of the M clusters. Hence the clusters formed by the substitutional atoms, without C atoms, can be predicted by looking at the pair interactions.

For the M-C-C triplets the binding energy of the triplet differs from the sum of binding energy for the pairs that make up the triplet as is displayed in Table 5.4, here the binding energies for the C-C pairs are taken from [13]. Note that the triplets where the C atoms are closer to the M atom are favoured. It is observed that the triplets display the

same preferential ordering. For the studied metals distinct trends are observed, hinting that the formation of M-C clusters may follow similar steps for all metals. The III-0-2 triplet contains a 0-2 C-C pair, and two I-1 M-C pairs. The III'-0-3 triplet contains a 0-3 C-C pair, a I-1 M-C pair, and I-2 M-C pair. Note that the site III' is the III site mirrored in the {100} plane containing the I, II, IV, and VII sites. In simulations using the MEAM potentials it has been shown that the formation of a Fe-M-C cluster is preceded by the clustering of C atoms [13], as the binding of M atoms to a pre-existing Fe-C cluster is more favourable than the clustering of M atoms in ferrite. At this scale the same preference for all investigated M atoms to attach to a C atom 'cluster' is observed. Nevertheless the interaction between M and C atoms is less predictable, so the exact energies cannot be inferred by summing pair interactions.

The DFT calculations show that the various transition metals display similar trends for their pair interactions within the bcc iron lattice, hinting that their carbides form in a similar manner, which is experimentally observed for TiC, VC, and NbC precipitates [7–10]. Additionally, simulations have previously shown that TiC and NbC carbides form following a similar path [13], where both the M-M and M-C pair interactions for both metals displayed similar trends.

	Ti	Zr	Hf	V	Nb	Ta
M-M-M triplet						
I-IV-VII	-0.030	0.025	0.015	-0.076	-0.059	-0.054
I-IV-VIII	0.000	-0.065	-0.063	-0.042	-0.080	-0.074
I-V-VII	0.008	-0.123	-	-0.053	-0.140	-0.124
M-C-C triplet						
III-0-2	0.177	0.304	0.313	-0.163	-0.008	-0.034
III'-0-3	0.035	0.128	0.130	-0.165	-0.050	-0.071
$E_{bind.} - \Sigma(E_{bind. pairs in triplet})$						
III-0-2	0.071	0.086	0.081	0.085	0.080	0.084
III'-0-3	-0.111	-0.150	-0.150	-0.030	-0.066	-0.066

Table 5.4: Binding energies for metal triplets embedded in the ferrite matrix, the triplets are based on the most favourable M-M pairs from Tables 5.1 and 5.2. In all cases a $4 \times 4 \times 4$ bcc unit cell supercell is used. The various configurations can be found in Figure 5.1, except for III' which is the site where III is mirrored with respect to the (100) plane in which sites I, II, IV lie. The binding energy for the most favourable (or least unfavourable) triplet is printed bold. In the last two rows the difference in energy between the triplets and the pairs that can be found in the triplet are given, this shows that some triplets are favoured over the pairs. Particularly for the group V metals there is a strong preference for the III-0-2 triplets over the various pair energies.

5.4. TRANSFORMATION MECHANISM

5.4.1. TRANSFORMATION TO NaCl-STRUCTURE

SEVERAL M-C clusters are simulated using LAMMPS (v3mar20) [17], with two separate MEAM potentials for the Fe-Nb-C [15] and Fe-Ti-C [14] ternary systems to simulate the transition path. The initial (Fe,M)-C cluster has a structure where the C atoms lie in the {200} plane adjacent to the {100} plane containing the M and Fe atoms. We will refer to the {100} plane containing the M atoms as the habit plane. The M and Fe atoms form

a chequerboard-pattern in the habit plane. The structure of these clusters is presented in Figure 5.2, the generalized chemical formula is FeMC_3 where additional C atoms can be located at the outer edge of the cluster, for brevity we will write FeMC_3 . As there is a high Fe fraction present in the FeMC_3 clusters the interface between the cluster and the surrounding ferrite matrix is nearly perfectly coherent, it is observed that all simulated clusters (with a diameter up to 4.5 nm) retain a coherent interface. There are some specific features for the FeMC_3 cluster, also described in [13]:

- There are two types of C atoms; i) C atoms which lie in ‘rows’ where there are two C atoms (near a Fe site) on one side of the cluster, and ii) C atoms that lie ‘between-rows’. These rows, ideally, lie alternating on both sides of the {100}-plane in which the M atoms are situated. Which is displayed in Figures 5.2c and 5.2d.
- Fe atoms within the cluster have three close C neighbours. Two of these lie within a ‘row’, the other C atom lies ‘between-rows’. The Fe-C distance is roughly 1.85 Å for all three C atoms, hence the C atoms form a triangle as mentioned above. Also note that the Fe atom is pushed from the middle toward one of the M neighbours. The Fe-C network is shown in Figure 5.2e.
- The M atoms have 8 nearest Fe neighbours. These fall into two groups, the Fe atoms on the side of the in-row C atoms are pushed away from the M atom, whereas the other Fe atoms are pushed closer to the M atom. The Nb-Fe connections are shown in Figure 5.2f.

The transition from the FeMC_3 cluster, as given in Figure 5.2, to a MC precipitate with a NaCl-structure depends on the cluster size and does not occur for small clusters, as observed experimentally [8, 10]. Notice that a single {100} plane in the bcc lattice is a {100} plane rotated by 45° in a fcc lattice. The NaCl-structure consists of two superposed fcc lattices, one being a M lattice and the other a C lattice. As mentioned, the FeMC_3 cluster has its M atoms in a single {100} plane, i.e., the habit plane, but the C atoms lie in the first adjacent {200} planes. The transition to a NaCl structure thus requires the movement of the C atoms, and the movement of M atoms. The M atoms can come from the solid solution, or move within the cluster itself. In Figure 5.3 a schematic overview of the transformation is presented.

The C atoms move into the ‘NaCl-sites’, i.e., into the octahedral interstitials in the habit plane. The rearrangement of C atoms occurs around some of the Fe atoms in the habit plane, and may be preceded by the substitution of the Fe atom by a vacancy as the substitution of Fe atoms by vacancies is also energetically favourable, e.g., in Figure 5.3 (step 2) for FeNbC_3 (in the 8×8 cluster) the movement of the C atoms increases the binding energy by 4 eV, only removing the Fe atom gains 1.5 eV, and both removing the Fe atom and moving the C atoms gains 5.7 eV, so the combination is most favourable (Table 5.5). We note that the increase in binding energy is very large for the 8×8 cluster, in practice these relatively large clusters would not retain their FeNbC_3 structure. The transformation is likely to occur in smaller clusters, as the increase in binding energy associated with the transformations is significant as shown in Table 5.5. The preference for both relocating C atoms, and replacing Fe atoms with vacancies indicates that vacancies can enhance the transformation speed as they incentivise the relocation of C atoms in

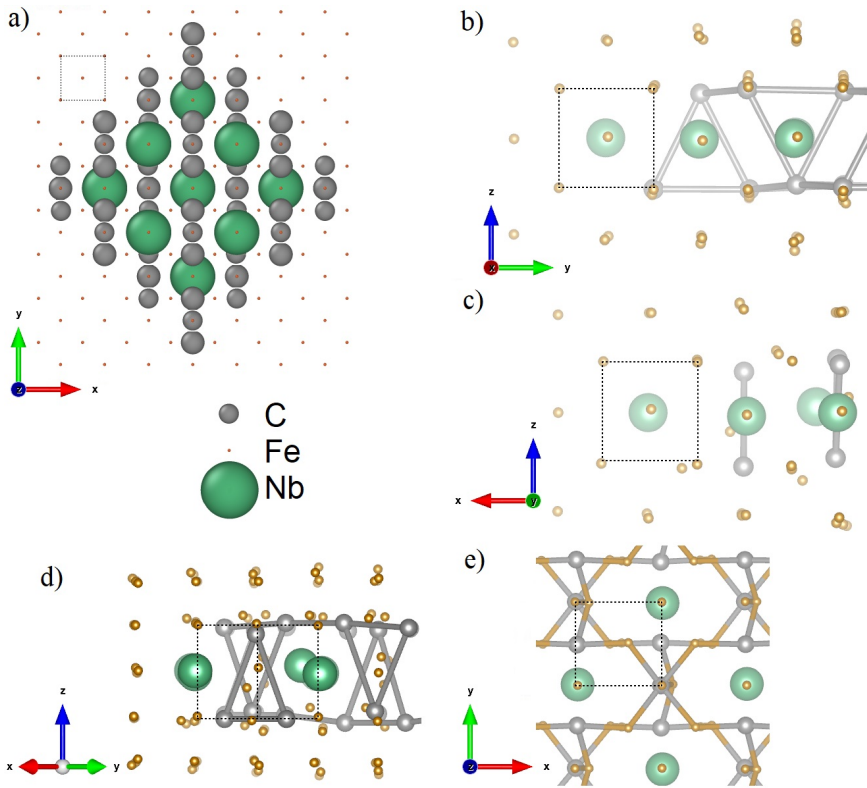


Figure 5.2: The Initial FeMC₃ cluster illustrated for M = Nb, however for M = Ti the same cluster is found [13]. The small (brown) atoms are the Fe atoms, chosen small to not obscure the cluster, the large (green) atoms are the Nb atoms, and the mid-sized (grey) atoms are the C atoms. In a) a topview of a 3 × 3 cluster lying in a (001) plane is presented, with the black dotted line the outline of a bcc unit cell is shown. For further clarity the C atoms that lie on top of the (001) habit plane are slightly larger than those below. Figures b) to d) show a side-view of a part of the cluster; all figures show bonds between C atoms in the relaxed system shorter than 3 Å, atoms further from the observer are faded. In b) a part of the cluster is shown from the [100] direction, where the triangles formed by C atoms are visualised. In c) a part of the cluster is shown from the [010] direction, where the triangles are not visible. In d) a view from the [110] direction of a part of the cluster is given, where the triangles are visible. In e) a top-view of a part of the cluster is shown, where the Fe-C bonds with a length between 1.8 Å and 2 Å are shown in grey and yellow. A set of coordinates for 3D examination of an example cluster is provided in the supplemental data [26].

the habit plane. Additionally, it is remarked that the clusters, for all sizes, act as strong vacancy attractors, cf. [13].

Additionally several of the C atoms in neighbouring sites are pushed outward from the habit plane. These C atoms are still close to the FeMC₃ cluster and are still attracted to the cluster, however their binding energy is lowered making it easier for the C atoms to dissolve back into the matrix. These excess C atoms can then attach to other clusters, or re-attach to the cluster at more favourable sites. We note a strong bond between C atoms and vacancies in the matrix, where for a vacancy and a C atom at a 1NN octahedral site

the binding energy is found to be 0.89 eV using [14, 15]. We also notice that some of the C atoms are bound less strong to the cluster, as some sites show a binding energy of just 0.57 eV. So C atoms can form a complex with a vacancy, the C-vacancy complex can then move away from a cluster.

The Fe atom (or vacancy) around which the C atoms are moved can be replaced by a M atom as in step 3a Fig. 5.3, this is not always energetically favourable, particularly for large M atoms like Nb. Alternatively the Fe atom in the cluster can be replaced by a vacancy. Hence the cluster acts as a ‘vacancy sink’. Vacancies can then move through the cluster displacing M atoms to form a NaCl-structure locally, as depicted in Figure 5.3 step 3b. Note that this immediately results in a Baker-Nutting orientation relation (BN-OR) [27–30]. The movement of C atoms, and the substitution of vacancies or M atoms can occur at the same time for different sites. In steps 4 and 5 of Figure 5.3 snapshots are shown of the transforming cluster in which multiple sites are changed.

Cluster size	2 × 2	4 × 4	6 × 6	8 × 8
Change ΔE_{bind} .	[eV]			
Relocate C atoms	-0.64	-0.52	3.13	3.97
Replace Fe atom with vacancy	1.12	0.69	2.00	1.52
Relocate C atoms + replace Fe atom with vacancy	1.32	2.81	3.28	5.69
Replace Fe atom with Nb atom	-2.30	-0.33	1.20	-0.27
Relocate C atoms + replace Fe atom with Nb atom	-1.23	-1.65	0.99	2.71
Relocate C atom + subs. vac. + move neighbour Nb atom	-0.65	-1.14	2.23	5.09

Table 5.5: Change in binding energy following transformation/relocation at the centre atom of a $N \times N$ FeNbC₃ cluster (the site in Step 2. of Fig. 5.3). Various changes are checked and combined, such as the relocation of C atoms, the substitution of the Fe atom by a vacancy or a M atom, and finally the substitution with a vacancy and movement of a neighbouring M atom with relocated C atoms. As the size of the cluster increases the favourability of the transformation is greater. Given the large change in binding energy for the relocation of C atoms, over 3 eV for a 6 × 6 cluster, the original FeNbC₃ structure is not expected to be maintained when the cluster reaches a size larger than 6 × 6.

Cluster size	2 × 2	4 × 4	6 × 6	8 × 8
Change ΔE_{bind} .	[eV]			
Relocate C atoms	-0.64	0.07	-2.08	2.74
Replace Fe atom with vacancy	-0.39	-0.54	-0.57	-0.30
Relocate C atoms + replace Fe atom with vacancy	-1.26	-0.43	0.57	3.42
Replace Fe atom with Ti atom	1.04	1.51	1.73	1.91
Relocate C atoms + replace Fe atom with Ti atom	1.28	0.65	1.34	5.56
Relocate C atom + subs. vac. + move neighbour Ti atom	-1.66	-1.72	-2.82	2.80

Table 5.6: Change in binding energy following transformation/relocation at the centre atom of a $N \times N$ FeTiC₃ cluster (the site in Step 2. of Fig. 5.3). Various changes are checked and combined, such as the relocation of C atoms, the substitution of the Fe atom by a vacancy or a M atom, and finally the substitution with a vacancy and movement of a neighbouring M atom with relocated C atoms. As the size of the cluster increases the favourability of the transformation is greater.

For smaller FeMC₃ clusters the substitution of Fe atoms with M atoms has an ener-

getically unfavourable effect, the Fe atoms are rather replaced by vacancies. For larger clusters (larger than 7×7 Nb atoms, 5×5 Ti atoms) part of the Fe atoms can be substituted with M atoms. In the case of the 7×7 Nb cluster the gain in binding energy is 1.8 eV when substituting the centre Fe atom, however the substitution of a second M atom is unfavourable as is the substitution of Nb atoms at other sites. Hence there is a dependence on the cluster size for the transformation, but also a dependence on the M atom size as for Ti this effect is weaker (see Table 5.6). This seems to be a size effect as Ti atoms are much smaller than Nb atoms, so the strain caused by Ti atoms is smaller than for Nb atoms. Hence Ti atoms have a better fit in the cluster.

The energetic favourability for the presence of vacancies in the FeMC_3 clusters and the role that they seemingly play in the movement of M atoms shows a parallel to the behaviour of the Guinier-Preston zone in aluminium alloys [31, 32], e.g., Al-Cu, and Al-Ag. In aluminium alloys the GP zone acts as a ‘vacancy pump’ [33, 34], as the GP zone attracts vacancies (and vacancy-Cu complexes) there is a local accumulation of vacancies driving back vacancies into the matrix which in turn allows for the attraction of new M atoms as vacancies bind to the M atoms.

An attractive binding between first nearest-neighbour (1NN) vacancies and M atoms in the ferrite matrix was observed in this study. For the used MEAM potentials we find 0.05 eV for Nb atoms and 1NN vacancies, and 0.13 eV for Ti atoms and 1NN vacancies [14, 15]. A strong bond of 0.89 eV forms between a vacancy and a C atom at a 1NN octahedral site. DFT results show a stronger binding of 0.36 eV and 0.24 eV for with 1NN vacancies for Nb and Ti atoms respectively [35]. This confirms that the FeMC_3 cluster attracts vacancies and acts as a vacancy-sink.

To fully resemble the vacancy-pump described by Girifalco and Herman [33] the bond between M atoms and vacancies needs to be small, to be precise the binding of a complex needs to be weak near a FeMC_3 cluster, additionally the interaction between the FeMC_3 cluster and the vacancy and between the FeMC_3 cluster and the complex needs to be small. The cluster has quite strong bonds with vacancies, so several vacancies will remain ‘attached’ to the cluster. However for vacancy complexes with C atoms there is a possibility that vacancies allow for transportation of excess C atoms away from a transformed cluster back into the matrix. So the cluster displays a partial resemblance of the GP zone, where we find a vacancy pump behaviour, but instead the ‘pumping’ relies on the trade of M atoms for C atoms in vacancy complexes.

The relocation of the C atoms is favoured near the centre of the cluster, however the M atoms (particularly for Nb) are more easily added in ‘NaCl-sites’ near the edge. In the example of Figure 5.3 substituting a Nb at the centre site is unfavourable, as the total binding energy is lowered by 1 eV. Whereas substituting a Nb atom at the edge site (step 3a Fig. 5.3) is favourable, as the total binding energy increases by 0.6 eV. Secondly, the relocation of the C atoms around Fe sites (as in step 2 Fig. 5.3) favours the direction parallel to the ‘rows’ of C atoms, as displayed in step 3 of Figure 5.3. As the cluster grows larger (in the habit plane) the number of M atoms that can be added in the planar cluster increases, both by substitution of Fe by M atoms in the cluster and by growth of the cluster at its edges. For example in a 5×5 FeNbC_3 cluster only the C atoms for a single Fe atom can be moved in an energetically favourable manner, but a Nb atom cannot be entered in a favourable way. For a 7×7 FeNbC_3 cluster the number of atoms that

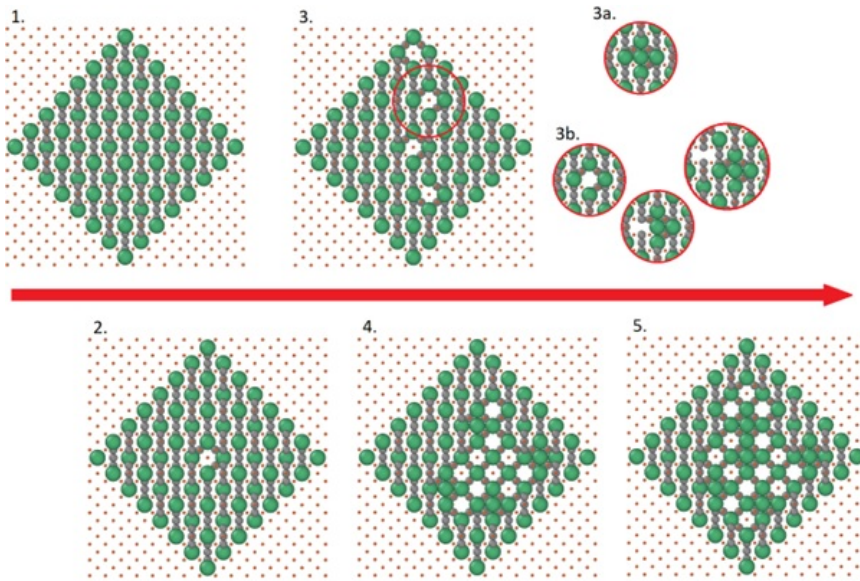


Figure 5.3: A schematic overview of the transformation of a FeMC_3 cluster, for all steps a snapshot of an idealised representation of the cluster where the change is visible is provided. In step 1 an ideal FeMC_3 cluster is shown. In step 2 the C atoms around a single Fe site have moved into the 'NaCl-sites'. In step 3 multiple C atoms have moved into the 'NaCl-sites'. In steps 3a and 3b the two follow-up options are presented. In 3a a M atom has replaced the Fe atom at one of the sites, an alternative path is illustrated in 3b where the Fe atom is replaced by a vacancy. In 3b we also show that a neighbouring M atom then moves into a (local) NaCl-structure where the vacancy migrates through the FeMC_3 cluster, note that the M atoms generally need to overcome a significant activation energy to migrate through the FeMC_3 cluster [13]. This process can be repeated where C atoms are moved into the habit plane, and vacancies or M atoms attach to the cluster to form a structure that locally has a NaCl-structure as shown in steps 4 and 5. Steps 4 and 5 show snapshots of the transformation of the cluster.

can be moved in a favourable manner is increased as can be seen in Figure 5.3 step 4, where multiple Nb atoms (and vacancies) have been added whilst increasing the binding energy of the cluster by over 2 eV.

5.4.2. MATRIX MISFIT AND STRAIN

SEVERAL factors may contribute to the change in cluster structure, but most notably the strain in the matrix, as the misfit between bcc Fe and NbC in the BN-OR is large and therefore causing an increase in total energy. For the MEAM potential there is an approximate 12% misfit between the surface of the precipitate and the ferrite matrix, i.e., in the $\langle 100 \rangle$ directions parallel to the $\{100\}_\alpha$ plane in which the precipitate is situated, for the NbC [15] and approximately 9% for TiC [14]. This impacts the coherency of the precipitate-matrix interface as observed by Sawada et al. [36]. For the NaCl-structure it has been found that NbC precipitates (multi layered cuboids) become semi-coherent at sizes above roughly 1.8 nm, for TiC this occurs at 3.6 nm [36]. Precipitates retain coherency longer, the more plate-like [37], as also observed in the current work where none of the studied clusters, of which the largest is a 11×11 M atom cluster (~ 4.5 nm) consist-

ing of a single layer, lost its coherency when fully relaxed.

The FeMC_3 cluster and the partially transformed clusters have a better fit with the bcc lattice than the NaCl-structured MC. FeMC_3 clusters display anisotropy in their lattice parameter. We relax the {100} plane, and the {200} containing the M and C atoms to find approximate lattice parameters, for FeNbC_3 the lattice parameter parallel to the C atom rows is 2.98 Å and 3.08 Å perpendicular to the rows, and for FeTiC_3 the lattice parameter parallel to the C rows is 2.93 Å and 3.03 Å perpendicular. There are much smaller misfits than for the NbC and TiC carbides at just 4% parallel and 7% perpendicular (to the C rows) for FeNbC_3 , and 2% parallel and 6% perpendicular for FeTiC_3 . It has been suggested that the strain in the direction perpendicular to the habit plane of the precipitate is the root cause for the transformation to NaCl-structured carbides [10]. In this work it is observed that in the {100} planes parallel to the cluster the Fe atoms are displaced outward perpendicular to the habit plane of the cluster (tensile strain), this strain is lowered with the transition to MC for larger clusters, which is displayed in Figure 5.4.

In Figure 5.4c and 5.4d C atoms are moved into the ‘NaCl-sites’ to demonstrate the effect on the displacement in the matrix without interference with other effects, e.g., vacancies, substitution of Fe atoms by M atoms etc. Note that besides moving C atoms several C atoms are also removed in Figure 5.4c and 5.4d. The real transformation occurs in steps and only for parts of the cluster as presented in Figure 5.3, which is discussed above.

The displacement in the surrounding ferrite matrix caused by the original FeMC_3 cluster is in large parts directed in $\langle 110 \rangle$ directions, whereas the displacement by a NaCl-structured {100} platelet is primarily directed in the $\langle 001 \rangle$ directions. The driving force behind the transformation from FeMC_3 to MC can be understood from the strain energy density in the matrix associated with these two directions, f_{strain}^{hkl} , as adapted from [38].

$$f_{strain}^{hkl} = 2\epsilon^2 Y(hkl). \quad (5.3)$$

Where hkl indicates the direction of the strain, ϵ is the magnitude of the strain given by $\epsilon = (a - a_0) / a_0$ where a_0 is the equilibrium lattice parameter, and a the strained lattice parameter. Finally $Y(hkl)$ is the associated elastic constant. To get an energy (per atom) rather than an energy density Eq. (5.3) is integrated over the atomic volume of the equilibrium state:

$$E_{strain}^{hkl} = 2\epsilon^2 Y(hkl) V_{at}. \quad (5.4)$$

Where v_{at} is the atomic volume in the equilibrium state. From [38] the elastic constants can be found for different directions:

$$Y(100) = \frac{(C_{11} + 2C_{12})(C_{11} - C_{12})}{C_{11}}, \text{ and } Y(110) = \frac{3(C_{11} + 2C_{12})(C_{11} - C_{12} + 4C_{44})}{5C_{11} - 4C_{12} + 8C_{44}}. \quad (5.5)$$

Here C_{ij} are the elastic parameters in Voigt notation. For iron, as used in the MEAM potential [14, 15], $Y(100) = 224$ GPa and $Y(110) = 337$ GPa. The main strain contribution comes from the ferrite matrix, as it is observed in simulations performed in this study that clusters consisting of a single layer conform to the matrix lattice to form a highly coherent interface. The M atoms are displaced out of the habit plane to form a wave-like

pattern (Fig. 5.5) whilst still forming a single atom layer. This is quite similar to the rippling observed in Fe/MC interfaces seen by Jung et al. [39] except that there are no bulk MC layers in the simulations performed in this work.

In simulations, of the two clusters depicted in Figure 5.4, for Fe-Nb-C it is established that the strain varies greatly along the surface of the formed FeMC_3 and MC cluster. The largest strain occurs toward the edges of the cluster, further indicating that the transformation depends on the cluster size. Using the displacement in the direct neighbouring $\{100\}$ planes parallel to the habit plane the strain energy is calculated using Eq. (5.4), the clusters depicted in Figure 5.4 are used. For the FeMC_3 cluster the strain energy density is roughly 1.6 eV per Fe (in the first adjacent $\{100\}$ plane) atom based on an average displacement of 0.4 Å in the $\langle 100 \rangle$ direction and 0.4 Å in the $\langle 110 \rangle$ direction, for the MC cluster the strain energy density is 1.0 eV per Fe atom based on the average displacement of 0.5 Å in the $\langle 100 \rangle$ direction. A similar trend is seen for the Fe-Ti-C system. Here it is noted that these strain energies are very high, so in real cluster we expect the transformation, as described above, to start in much smaller precipitates.

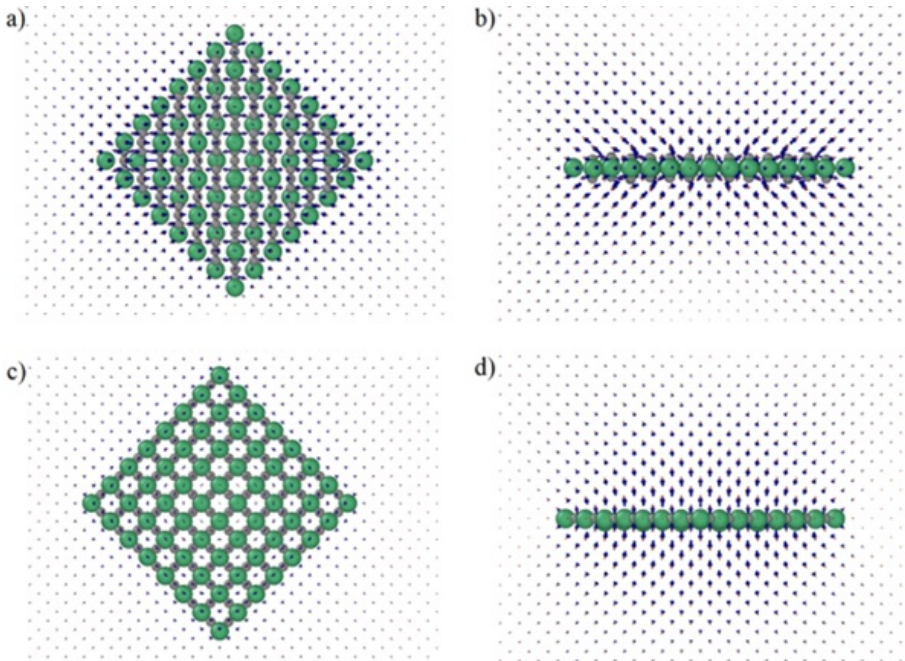


Figure 5.4: Displacement of Fe atoms in the matrix from their bcc equilibrium positions. The green (largest) atoms are the M atoms, and the grey (mid-sized) atoms are C atoms, and the smallest atoms are the Fe atoms. Idealised $(\text{Fe},\text{M})\text{C}_3$ cluster a) top-view, b) side view. The platelet with relocated (and some removed) C atoms still containing high a fraction of Fe c) top-view, d) side view. Fe atoms for the FeMC_3 cluster, a) and b), are displaced in the $\langle 110 \rangle$ directions out of the habit plane. For the platelet with relocated C atoms, c) and d), Fe atoms are displaced in the $\langle 100 \rangle$ direction perpendicular to the habit plane.

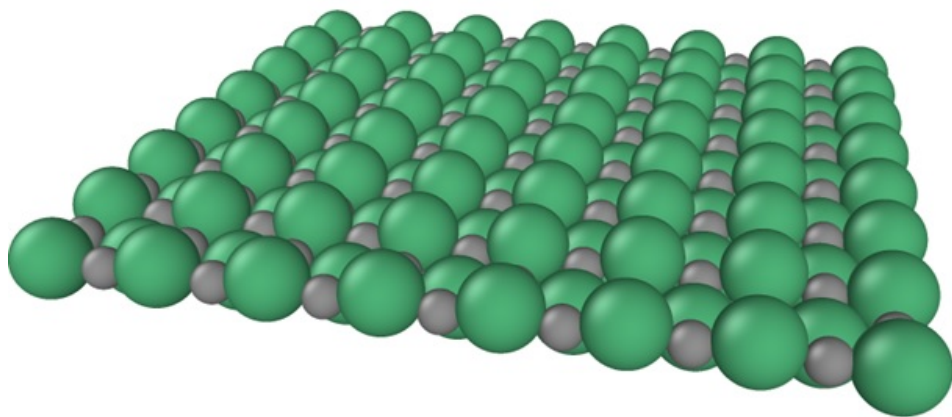


Figure 5.5: A single atomic layer of NbC where the Nb atoms are pushed out of the (100) habit plane of the platelet. The Nb atoms form a wave-like pattern where one half is pushed up, and the other half is pushed down.

5.4.3. RESULTS FROM LAMMPS SIMULATIONS

IN Figure 5.3 the transformation of a FeMC_3 cluster is shown, where various steps in the transformation are highlighted. Static relaxations of these steps in FeMC_3 clusters using LAMMPS for FeNbC_3 and FeTiC_3 show that the transformation occurs in steps, in these steps the binding energy of the cluster is increased. Initially the C atoms migrate to the octahedral interstitial sites in the habit plane, in the same step the Fe atoms can be replaced by vacancies. This movement of C atoms and the introduction of vacancies may occur for various sites in the $\{100\}$ habit plane of the FeMC_3 cluster. At the sites where the C atoms have rearranged into the habit plane, i.e., the 'NaCl-sites', a M atom can substitute an Fe atom or a vacancy. All these steps occur in an energetically favourable manner. The FeMC_3 cluster contains a high C atom fraction, it must be noted that these C atoms may (re-)attach to a M-C cluster or dissolve back into the matrix after the transformation. Generally C atoms are still (weakly) bound to the NaCl-structured platelet, however we note that some of the weakly bound C atoms form strong bonds with vacancies and can move away from a cluster via a C-vacancy complex.

We note that the FeNbC_3 cluster allows many vacancies within the cluster, for FeTiC_3 the number of vacancies is much lower. The main reason behind this seems to be the size difference between Nb and Ti atoms in ferrite [24], Nb atoms are much larger and cause more strain in their neighbourhood. Note that this coincides with the DFT results in Section 5.3, where large M atoms also display much less favourable (or even unfavourable) pair interactions with other M atoms or C atoms.

Thus the transformation occurs in steps, moreover the extent of the transformation depends on the cluster size. Small clusters cannot transform in an energetically favourable manner, but for larger clusters the transformation does increase the binding energy of the cluster. The FeMC_3 cluster diameter for which a favourable (partial) transformation may occur is 3 nm for NbC and 2 nm for TiC.

The main driving force for the transformation is determined to be the matrix strain

caused by the FeMC_3 cluster, in directions perpendicular to the habit plane of the cluster. A FeMC_3 cluster on the (001) habit plane causes a strain in the [110] and [1-10] directions in the ferrite matrix, whereas the MC platelet primarily causes a strain in the [100] direction. The strain in $\langle 100 \rangle$ directions causes a lower strain energy than the strain in the $\langle 110 \rangle$ directions.

The transformation, as described in Section 5.4.1 and illustrated in Figure 5.3, is energetically favourable, hence the replacement and relocations of atoms in the transformation may occur simultaneously. The LAMMPS simulations further suggest that the FeMC_3 clusters act in a similar manner as GP zones in aluminium alloys [33, 34], where the GP zone attracts vacancies and the precipitate forming elements are bound to vacancies, which is also the case for the Nb and Ti atoms as verified in this study. As the precipitate forming atoms are attracted to vacancies, and the vacancies are attracted by the GP zone more precipitate forming atoms are attracted to the GP zone, where the GP zone acts as a weak ‘vacancy pump’ [33]. But in the case of these carbides the excess C atoms are necessary in the return of vacancies to the matrix.

The cluster size at which the transformation occurs is found to be ~ 3 nm for FeNbC_3 and ~ 2 nm for FeTiC_3 . Courtois et al. [7] find platelets of Nb(C,N) precipitates with an average size ~ 3 nm using TEM, and ~ 8 nm using High-Resolution TEM. Breen et al. [8] find Nb(C,N) platelets as small as ~ 3 nm. Wang et al. [10] find (Ti,Mo)C platelets of sizes ~ 1.5 nm, which they call embryo clusters, as these small cluster have not fully taken to NaCl-structure, which occurs at sizes of 6 nm and larger. So the simulation results are in agreement with the experimental results.

Experimental clusters however show a lower carbon concentration for the Carbide clusters, in part this is due to the presence of N atoms. Additionally we note that C atoms have a higher mobility than the M atoms and can therefore move away from the FeMC_3 cluster during the transformation.

The current study does not provide a time-scale at which the transformation takes place. Experimental studies [7–10] indicate that platelets can form in $\sim 10^1$ to $\sim 10^2$ seconds, the timescale depends strongly on temperature, e.g., [8]. Therefore it may be difficult to observe a FeMC_3 cluster, as they transform already at small sizes (~ 3 nm for FeNbC_3 , ~ 2 nm for FeTiC_3) to MC platelets. Furthermore we have found that FeMC_3 clusters are highly coherent with the ferrite matrix making detection harder.

5.5. CONCLUSION

THE pair interactions of M atoms, where $M = \text{Ti, Zr, Hf, V, Nb, Ta}$, in M-M pairs and M-C pairs embedded in ferrite display a same pattern for all studied metals. Indicating that the transition metal carbides all form in a similar manner. M atoms attach to a C atom cluster in ferrite in which an ordered FeMC_3 cluster forms in a $\{100\}$ oriented lattice plane of the ferrite matrix. Here the M atoms form a checkerboard pattern with Fe atoms in a single $\{100\}$ plane, this Fe-M structure is surrounded by C atoms.

The clusters that form initially do not have the NaCl-structure, but rather a FeMC_3 stoichiometry containing a large Fe fraction. The results from our simulations show that the transformation occurs through several energetically favourable steps in which vacancies seem to play a significant role. The role of vacancies and the FeMC_3 clusters

appears similar to that of GP zones in aluminium alloys.

Furthermore the in-plane transformation to NaCl-structured platelets is found to be driven by the strain directed in the directions perpendicular to the habit plane of the cluster/precipitate, i.e., in the (100) planes neighbouring the habit plane.

The formation and transformation of FeMC_3 clusters presented here provide the theoretical basis that clarifies experimentally observed carbide platelet nucleation and (early) growth.

REFERENCES

- [1] R. J. Slooter, M. H. F. Sluiter, W. G. T. Kranendonk, and C. Bos. Formation and growth of transition metal carbides in ferrite. *Computational Materials Science*, 242:113097, 2024.
- [2] R. J. Slooter, M. H. F. Sluiter, W. G. T. Kranendonk, and C. Bos. Investigation of NbC proto-nuclei in steel. In *CALPHAD 2022*, 2022.
- [3] M. Volmer and A. Weber. Keimbildung in übersättigten Gebilden. *Zeitschrift für Physikalische Chemie*, 119:277–301, 1926.
- [4] R. Becker and W. Döring. Kinetische Behandlung der Keimbildung in übersättigten Dämpfen. *Annalen der Physik*, 416(8):719, 1935.
- [5] R. Kampmann and R. Wagner. Kinetics of precipitation in metastable binary alloys - Theory and application to Cu-1.9 at% Ti and Ni 14 at% Al. In P. Haasen, V. Gerold, R. Wagner, and M. F. Ashby, editors, *Decomposition of alloys: the early stages: proceedings of the 2nd acta-scripta metallurgica conference*, number 2 in 2. Acta metallurgica, Pergamon press, 1984.
- [6] M. Perez, M. Dumont, and D. Acevedo-Reyes. Implementation of classical nucleation and growth theories for precipitation. *Acta materialia*, 56:2119–2132, March 2008.
- [7] E. Courtois, T. Epicier, and C. Scott. Characterisation of niobium carbide and carbonitride evolution within ferrite: contribution of transmission electron microscopy and advanced associated techniques. *Materials Science Forum*, 500-501:669–676, 2005.
- [8] A. J. Breen, K. Y. Xie, M. P. Moody, B. Gault, H.-W. Yen, C. C. Wong, J. M. Cairney, and S. P. Ringer. Resolving the morphology of niobium carbonitride nano-precipitates in steel using atom probe tomography. *Microscopy and microanalysis*, 20:1100–1110, 2014.
- [9] J. Takahashi, K. Kawakami, and Y. Kobayashi. Origin of hydrogen trapping site in vanadium carbide precipitation strengthening steel. *Acta materialia*, 153:193–204, 2018.
- [10] J. Wang, M. Weyland, I. Bikmukhametov, M. K. Miller, P. D. Hodgson, and I. Timokhina. Transformation from cluster to nano-precipitate in microalloyed ferritic steel. *Scripta materialia*, 160:53–57, 2019.

- [11] X. Zhang, C. Ioannidou, G. H. ten Brink, A. Navarro-López, J. Wormann, J. Campaniello, R. M. Dalgliesh, A. A. van Well, S. E. Offerman, W. G. T. Kranendonk, and B. J. Kooi. Microstructure, precipitate and property evolution in cold-rolled Ti-V high strength low alloy steel. *Materials and Design*, 192:108720, 2020.
- [12] C. Ioannidou, A. Navarro-López, A. Rijkenberg, R. M. Dalgliesh, S. Koelling, C. Pappas, J. Sietsma, A. A. van Well, and S. E. Offerman. Evolution of the precipitate composition during annealing of vanadium micro-alloyed steels by in-situ SANS. *Acta Materialia*, 201:217–230, 2020.
- [13] R. J. Slooter, M. H. F. Sluiter, W. G. T. Kranendonk, and C. Bos. Atomistic simulations of carbide nucleation in ferrite. *Computational Materials Science*, 230:112455, 2023.
- [14] H.-K. Kim, W.-S. Jung, and B.-J. Lee. Modified embedded-atom method interatomic potential for the Fe-Ti-C and Fe-Ti-N ternary systems. *Acta materialia*, 57:3140–3147, 2009.
- [15] H.-K. Kim, W.-S. Jung, and B.-J. Lee. Modified embedded-atom method interatomic potentials for the Nb-C, Nb-N, Fe-Nb-C, and Fe-Nb-N systems. *Journal for material research*, 25(7):1288–1297, 2010.
- [16] M. H. F. Sluiter. Phase stability of carbides and nitrides in steel. In *Materials research society symposia proceedings*, volume 979, 2006.
- [17] A. P. Thompson, H. M. Aktulga, R. Berger, D. S. Bolintineanu, W. M. Brown, P. S. Crozier, P. J. in 't Veld, A. Kohlmeyer, S. G. Moore, T. D. Nguyen, R. Shan, M. J. Stevens, J. Tranchida, C. Trott, and S. J. Plimpton. LAMMPS - a flexible simulation tool for particle-based materials modeling at the atomic, meso, and continuum scales. *Computer Physics Communications*, 271:108171, 2022.
- [18] D. A. Porter, K. E. Easterling, and M. Y. Sherif. *Phase transformations in metals and alloys*. CRC Press, Taylor and Francis group, third edition, 2009.
- [19] G. Kresse and J. Hafner. *Ab initio* molecular dynamics for liquid metals. *Physical Review B*, 47(1):558–561, 1993.
- [20] G. Kresse and J. hafner. *Ab initio* molecular-dynamics simulation of the liquid-metal-amorphous-semiconductor transition on germanium. *Physical Review B*, 49(20):14251–14269, 1994.
- [21] G. Kresse and J. Furthmüller. Efficient iterative schemes for *ab initio* total-energy calculations using a plane-wave basis set. *Physical Review B*, 54(16):11169–11186, 1996.
- [22] G. Kresse and J. Furthmüller. Efficiency of *ab-initio* total energy calculations for metals and semiconductors using a plane-wave basis set. *Computational Materials Science*, 6(1):15–50, 1996.
- [23] G. Kresse and D. Joubert. From ultrasoft pseudopotentials to the projector augmented-wave method. *Physical Review B*, 59(3):1758–1775, 1999.

- [24] C. K. Ande and M. H. F. Sluiter. First-Principles calculations on stabilization of iron carbides (Fe_3C , Fe_5C_2 , and $\eta\text{-Fe}_2\text{C}$) in steels by common alloying elements. *Metallurgical and Materials Transactions A*, 43A:4436–4444, November 2012.
- [25] W.-S. Jung and S.-H. Chung. Ab initio calculation of interfacial energies between transition metal carbides and fcc iron. *Modelling and simulation in materials science and engineering*, 18(7):075008, 2010.
- [26] R. J. Slooter, M. H. F. Sluiter, W. G. T. Kranendonk, and C. Bos. Supplemental data.
- [27] R. G. Baker and J. Nutting. *Iron and Steel Institute Special Report*, 64:1–22, 1959.
- [28] R. M. Smith and D. P. Dunne. Structural aspects of alloy carbonitride precipitation in microalloyed steels. *Materials Forum*, 11:166–181, 1988.
- [29] F. Ishikawa, T. Takahashi, and T. Ochi. Intragranular ferrite nucleation in medium-carbon vanadium steels. *Metallurgical and Materials Transactions A*, 25:929–936, 1994.
- [30] Z.-G. Yang and M. Enomoto. Discrete lattice plane analysis of Baker-Nutting related B1 compound/ferrite interfacial energy. *Materials Science and Engineering*, 332:184–192, 2002.
- [31] A. Guinier. Un nouveau type de diagrammes de rayons X. *Comptes Rendus Hebdomadaires Des Séances De L'Académie Sciences*, 206:1641–1643, 1938.
- [32] G. D. Preston. The diffraction of X-rays by an age-hardening alloy of aluminium and copper. The structure of an intermediate phase. *The London, Edinburgh, and Dublin Philosophical Magazine and Journal of Science*, 26:855–871, 1938.
- [33] L. A. Girifalco and H. Herman. A model for the growth of Guinier-Preston zones-the vacancy pump. *Acta Metallurgica*, 13(6):583–590, June 1965.
- [34] M. V. Petrik, Y. N. Gornostyrev, and P. A. Korzhavyi. Point defect interactions with Guinier-Preston zones in Al-Cu based alloys: Vacancy mediated GPZ to θ' -phase transformation. *Scripta Materialia*, 165:123–127, 2019.
- [35] C. D. Versteyleen, N. H. van Dijk, and M. H. F. Sluiter. First-principles analysis of solute diffusion in dilute bcc Fe-X alloys. *Physical Review B*, 96:094105, 2017.
- [36] H. Sawada, S. Taniguchi, K. Kawakami, and T. Ozaki. Transition of the interface between iron and carbide precipitate from coherent to semi-coherent. *Metals*, 7:277–289, 2017.
- [37] H. Sawada, S. Taniguchi, K. Kawakami, and T. Ozaki. First-principles study of interface structure and energy of Fe/NbC. *Modelling and simulation in materials science and engineering*, 21(4):045012, 2013.
- [38] J. W. Cahn. The impurity-drag effect in grain boundary motion. *Acta metallurgica*, 10:789–798, September 1962.
- [39] W.-S. Jung, S.-C. Lee, and S.-H. Chung. Energetics for interfaces between group IV transition metal carbides and bcc iron. *ISIJ international*, 48(9):1280–1284, 2008.

6

CONCLUSIONS & RECOMMENDATIONS

Les inventions des hommes vont en avançant de siècle en siècle. La bonté et la malice du monde en général restent la même.

Pascal

The first half of life is devoted to forming a healthy ego, the second half is going inward and letting go of it.

Carl Gustav Jung

This is a concluding chapter explaining the scientific and technical implications for society of the research findings. In this chapter recommendations are made for follow-up research.

6.1. MODELS FOR PRECIPITATION

IN Chapter 2 an approximation to the quasi-isothermal “mean-radius” CNGT model was derived. This approximation provides a simple yet close approximation to a full simulation of the nucleation and growth of single precipitates. The approximation therefore provides a quick method to assess the nucleation and growth process of precipitates in metals.

The main achievement of Chapter 2 is to provide intuitive tools which can provide an easier understanding of the precipitate nucleation and growth process. Several parameters τ_η , Σ , and τ_λ have been defined, where τ_η , and τ_λ are the characteristic times for nucleation and loss of over-saturation respectively (see Eqs. (2.19) and (2.26)), and Σ is a characteristic parameter for growth (see eq. (2.20)). From these parameters ‘characteristic times’: (i) a start-of-nucleation time, $t_{5\%}$; (ii) an end-of-nucleation time, $t_{95\%}$; (iii) a start-of-growth time $t_{g,5\%}$; (iv) an end-of-growth time $t_{g,95\%}$; (v) a coarsening time t_{coarse} are also defined. Such simple expressions are capable of predicting the approximate nucleation, growth and coarsening curve of a single precipitate, and provide a clear outline of the timeline concerning the formation of the precipitates.

With these characteristic times, there is no direct need to simulate precipitation behaviour. And decisions can be made to leave certain less relevant, second precipitates out of the simulation. This may for example be done for slow forming precipitates, which would hardly form within the simulated time as one of the key ingredients is already consumed by a fast forming precipitate.

The approximation however, only works for quasi-isothermal conditions, with quick temperature variations the approximation will lose accuracy and will take longer to calculate. Another point is that in most cases multiple precipitates form simultaneously, and at various sites. This is not captured in the approximation, the full simulation can therefore not be replaced by the presented approximation. These shortcomings would need to be addressed to make an approximation that can replace the model simulation.

6.2. RF-MEAM POTENTIAL

CHAPTER 3 presents a new RF-MEAM potential for iron, the RF-MEAM potential is not bound to a reference structure unlike traditional MEAM potentials which are bound to a reference structure and its corresponding Rose equation of state¹. The new potential for iron is aimed to reproduce and predict lattice properties and defect energies, most notably for vacancies, and self-diffusion. Additionally, surface energies and stacking fault energies are predicted well. Orientation relations between the bcc and fcc lattice are predicted well for both Nishiyama-Wassermann and Kurdjumov-Sachs interface orientations. The thermal expansion in the 800 K to 1300 K temperature range follows the experimental data well. Therefore the potential presented here can be used for simulations in α -Fe, and in γ -Fe, as well as in interphase simulations.

The use of RF-MEAM potentials provides an important tool to establish parameter values, which are needed in the CNGT models and approximation presented in Chapter 2. Additionally RF-MEAM potentials may be used to model the kinetics of precipitate nucleation, for which steps were taken in Chapters 4 and 5.

¹see Chapter 1.

The presented potential can only represent pure Fe, but through the use of *MEAMfit v2* it should be possible to add elements to form a binary or ternary system containing iron. There are several interesting systems which draw our attention:

- Of direct interest regarding this work one could seek a potential for the Fe-V-C ternary system as none existed at the time of writing.
- Also the ternary systems studied in Chapters 4 and 5, Fe-Nb-C and Fe-Ti-C, could be fitted without the need of a reference structure. Again this is important as the ternary system can now be fitted in multiple phases of the iron matrix.
- Further ternary systems regarding the carbide of the group IVB and group VB transition metals studied in Chapter 5. This would be the Fe-Ta-C, Fe-Zr-C, and Fe-Hf-C systems.
- Quaternary systems for studying complex precipitates, e.g., Fe-Nb-C-N, or Fe-Nb-Ti-C.

Importantly, we note that these potentials would need to be fitted with precipitates in mind, as some quinary potentials for high-entropy alloys (HEA's) exist. However these potentials are optimised for the HEA compositions, which does not fit within the topic of precipitate formation in steel.

6.3. CARBIDE FORMATION

CARBIDE formation was studied in Chapters 4 and 5. Through simulations using MEAM potentials for the Fe-Nb-C and Fe-Ti-C ternary systems it is found that before the actual formation of a M-C cluster, C atoms form clusters in the {100} planes of the ferrite matrix as a result of concentration fluctuations. M atoms (M = Nb, or Ti) attach to these clusters to form ordered structures with a FeMC_3 composition. Most notably, paths exist for which a monotone decrease in the total Gibbs energy of the system is witnessed.

These FeMC_3 lie within the {100} planes of the ferrite matrix, where they maintain a nearly perfectly coherent interface with the ferrite matrix. Furthermore, it is found that the FeMC_3 clusters are stable up to common process temperatures, i.e., the 1100 K range for FeNbC_3 , and 1185 K for FeTiC_3 , for common steel compositions.

Given the monotone decrease in the total Gibbs energy of the system, the stability at relevant temperatures, and the nearly perfectly coherent interface with the ferrite matrix, the FeMC_3 clusters present a very plausible precursor to MC nano-precipitate carbides. Particularly when considering the parallels with GP zones found in other precipitate forming alloys².

Additionally, the outline of the transformation from a FeMC_3 cluster to a NaCl-structured precipitate can be explained by an increasing strain around the FeMC_3 cluster in the ferrite matrix. This process, seems to be aided by vacancies, as is the transformation of GP zones in aluminium alloys.

²Al-Cu, see Chapter 1.

Moreover, DFT results imply that it is plausible that all group IVB and group VB transition metals form carbides in the same way. Despite several minor differences, the interaction of transition metal atoms amongst themselves as well as the interaction of metal atoms with carbon atoms in ferrite is remarkably similar. From various experiments for TiC, VC, and NbC such similarities were already observed. These similarities also suggest that the various transition metals, from a theoretical point of view, can be interchanged³. In the practical sense this might require far-reaching adaptations in the production of steel (e.g., heat treatment), and new raw resource management as Zr, Hf, and Ta are also scarce elements. Nevertheless, the end-product can retain its qualities even when using other carbide forming metals.

The behaviour for carbides has been studied in great detail. As the nitrides of these transition metals are also commonly used it is likely that there are similarities between the different nitrides. Furthermore, MEAM potentials exist to study TiN and NbN so combining our work on carbides and the existing potentials a study in nitrides should be performed. In addition, complex precipitates have not been addressed in Chapter 5. Complex precipitates like carbonitrides, or precipitates containing multiple metals are commonly found in steel. Due to the lack of usable MEAM potentials, and the computational demand of DFT calculations this is a very challenging investigation. However, this is where AI potentials could present an opportunity to overcome these difficulties.

To gain a more complete understanding of the formation of carbides (and nitrides) several other issues need to be addressed, which were not addressed in this work:

- We lack insight in the kinetics which surround the formation process.
- What is the influence of the nucleation site?
- An analytical model, using the kinetics for the formation of precipitates. Replacing the Classical Nucleation Theory, describing the formation of the found FeMC_3 clusters and their transformation to NaCl-structured carbides. Obviously, this would be required for nitrides as well.
- The FeMC_3 clusters form as single layers, how and when the growth of additional layers occurs is not clear. For instance, does this occur after the first layer is fully transformed to a NaCl-structure or simultaneously with the transformation.
- Do the NaCl-structured precipitates always form spheroidal precipitates as commonly found in experiments⁴. Or can other shapes form with different conditions?

³Notwithstanding that they may form at different temperatures and have (slightly) different mechanical properties

⁴See for example: X. Zhang “*Precipitate evolution in grain oriented electrical steel and high strength low alloy steel*”, or C. Ioannidou “*Microstructure of vanadium micro-alloyed steels for automotive applications*”.

A

SENSITIVITY ANALYSIS OF THE KAMPMANN-WAGNER NUMERICAL MODEL

*Sommige mensen vernietig je door ze te bewijzen dat hun vooroordeel onjuist is.
't is alles wat ze bezitten.*

Simon Carmiggelt

Onredelijk is alleen onze rede, die alles wil weten en formuleren, op alle momenten.

Simon Vestdijk

In this Appendix a brief, and far from exhaustive, sensitivity analysis is performed for the Kampmann-Wagner Numerical (KWN) model.

A.1. MATHEMATICAL ANALYSIS

WHICH parameters are of the greatest importance for the KWN model [1]? There are three parameters that mainly influence the development of precipitates.

- The diffusion coefficient D , of the elements present in the matrix.
- The interface energy γ , of the matrix-precipitate interface.
- The solubility product K^{Eq} of the precipitate.

First we restate the nucleation rate

$$\frac{dN}{dt} = \beta^* N_0 Z \exp\left(-\frac{\Delta G^*}{k_B T}\right), \quad (1.5)$$

and growth rate

$$\left.\frac{dR_{\text{prec}}}{dt}\right|_{\text{growth}} = \frac{D_{\text{eff}}}{R_{\text{prec}}} \frac{C - C^e \exp(R_0/R_{\text{prec}})}{C^P - C^e \exp(R_0/R_{\text{prec}})}. \quad (1.18)$$

For the meaning of all the symbols see Chapter 1. However for rewriting we note $R_0 = 2\gamma v_{\text{at}} (k_B T)^{-1}$ as defined in [2]. Deschamps *et al.* [2] further state that $R_0 = R^* \ln(C/C^{Eq})$, where R^* is the critical radius.

The mathematical analysis here will be limited to homogeneous precipitation for notational simplicity. For precipitation at dislocations, grain boundaries, etc. is quite similar, to this end one can enter the additional terms as described in Section 1.2. When the homogeneous case is taken Eqs. (1.5) and (1.18) can be written as (cf. [3]):

$$\frac{dN}{dt} \equiv \dot{N} = N_0 \frac{v_{\text{at}}}{\sqrt{k_B T}} \sqrt{-R^* \Delta G_v - \gamma} \frac{2D_{\text{eff}} C}{a^4} \exp\left(-\frac{\Delta G^*}{k_B T}\right), \quad (A.1a)$$

and

$$\left.\frac{dR}{dt}\right|_{\text{growth}} \equiv \dot{R} = \frac{D_{\text{eff}}}{R} \frac{C - C^e \left(\frac{C}{C^e}\right)^{R^*/R}}{C^P - C^e \left(\frac{C}{C^e}\right)^{R^*/R}}. \quad (A.1b)$$

Where the critical radius for homogeneous precipitates is $R^* = -2\gamma/\Delta G_v$, a is the matrix lattice constant, and the free energy barrier is $\Delta G^* = \frac{16\pi\gamma^3}{3(\Delta G_v)^2}$. So for homogeneous precipitation we find:

$$\dot{N} = N_0 \frac{v_{\text{at}}}{\sqrt{k_B T}} \sqrt{\gamma} \frac{2D_{\text{eff}} C}{a^4} \exp\left(-\frac{16\pi\gamma^3}{3(\Delta G_v)^2 k_B T}\right), \quad (A.2a)$$

and

$$\dot{R} = \frac{D_{\text{eff}}}{R} \frac{C - C^e \left(\frac{C}{C^e}\right)^{-2\gamma/(\Delta G_v R)}}{C^P - C^e \left(\frac{C}{C^e}\right)^{-2\gamma/(\Delta G_v R)}}. \quad (A.2b)$$

A.1.1. DIFFUSION COEFFICIENT

NUCLEATION and growth rate both depend linearly on the diffusion coefficient. In addition there is no dependence on the diffusion coefficient in the critical radius or free energy barrier.

$$\frac{d\dot{N}}{dD_{\text{eff}}} = N_0 \frac{v_{\text{at}}}{\sqrt{k_B T}} \sqrt{-R^* \Delta g_v - \gamma} \frac{2C}{a^4} \exp\left(-\frac{\Delta G^*}{k_B T}\right), \quad (\text{A.3a})$$

and

$$\frac{d\dot{R}}{dD_{\text{eff}}} = \frac{1}{R} \frac{C - C^e \left(\frac{C}{C^e}\right)^{R^*/R}}{C^P - C^e \left(\frac{C}{C^e}\right)^{R^*/R}}. \quad (\text{A.3b})$$

Where both derivatives with respect to the diffusion coefficient are independent of the diffusion coefficient.

A.1.2. INTERFACE ENERGY

FOR the interface energy the critical radius and free energy barrier provide additional dependency on the interface energy.

$$\frac{d\dot{N}}{d\gamma} = N_0 \frac{2D_{\text{eff}}C}{a^4} \frac{v_{\text{at}}}{\sqrt{k_B T}} \exp\left(-\frac{16\pi\gamma^3}{(\Delta G_v)^2 k_B T}\right) \left[\frac{1}{2\sqrt{\gamma}} - \frac{16\pi\gamma^2 \sqrt{\gamma}}{3(\Delta G_v)^2 k_B T} \right], \quad (\text{A.4a})$$

and

$$\frac{d\dot{R}}{d\gamma} = \frac{D_{\text{eff}}}{R} \frac{2C^e(C - C^P) \ln\left(\frac{C}{C^e}\right) \left(\frac{C}{C^e}\right)^{-2\gamma/(\Delta G_v R)}}{\Delta G_v R \left(C^P - C^e \left(\frac{C}{C^e}\right)^{-2\gamma/(\Delta G_v R)}\right)^2}. \quad (\text{A.4b})$$

For the nucleation rate it is observed that the sign of Eq. (A.4a) depends on the value of γ . If $\gamma > ((\Delta G_v)^2 k_B T / 32)^{1/3}$ the sign is positive. Generally speaking this is the case for supersaturated steel grades at common temperatures of the order of 10^3 K. When the sign is positive a higher interface energy increases the nucleation rate. In the case that the interface energy is small enough, the sign will be negative and the nucleation rate decreases with a higher interface energy. The minimal nucleation rate is reached at $\gamma = ((\Delta G_v)^2 k_B T / 32)^{1/3}$.

For the growth rate we note that Eq. (A.4b) has the opposite sign to the chemical energy ΔG_v as $C^P \gg C$. If the chemical energy is negative the matrix is supersaturated, i.e., precipitates form. If the chemical energy is positive no precipitates form. So when precipitation occurs, a higher interface energy increases the growth rate.

A.1.3. SOLUBILITY PRODUCT

THE final parameter that is assessed is the solubility product K^{Eq} . From [3] we take $\Delta G_v = -\frac{k_B T}{v_{\text{at}}} \ln\left(\frac{K}{K^{Eq}}\right)$, which is substituted in Eqs. (A.2a) and (A.2b).

$$\frac{d\dot{N}}{dK^{Eq}} = N_0 \frac{1}{\sqrt{k_B T}} \sqrt{\gamma} \frac{2D_{\text{eff}}C}{a^4} \exp\left(-\frac{16\pi\gamma^3}{3(\Delta G_v)^2 k_B T}\right) \frac{1}{(\Delta G_v)^3} \frac{32\pi\gamma^3}{3K^{Eq}}, \quad (\text{A.5a})$$

and

$$\frac{d\dot{R}}{dK^{Eq}} = -\frac{D_{\text{eff}}}{R} \frac{(C^P - C)C^e R^* \ln\left(\frac{C}{C^e}\right)\left(\frac{C}{C^e}\right)^{R^*/R}}{RK^{Eq} \ln\left(\frac{K}{K^{Eq}}\right)\left(C^P - C^e\left(\frac{C}{C^e}\right)^{R^*/R}\right)^2}. \quad (\text{A.5b})$$

The derivative of the nucleation rate with respect to the solubility product is negative for a supersaturated matrix, so higher solubility lowers the nucleation rate. For the dependence of the precipitate growth it is also found that the growth is slowed down with a higher solubility product. Both results are in line with expectations.

A.2. WORKED EXAMPLE: NIOBIUM CARBIDE

To illustrate the sensitivity to the parameters presented at the top of this Appendix it is useful to look at an example. The KWN model (as implemented in [3]) is used to simulate the formation of niobium carbide (NbC). The formation of precipitates at dislocations is considered at a constant temperature of 850°C. The composition of the alloy is:

Element	Fe	C	N	P	S	Si	Mn	Nb	Al
wt%	98.4695	0.076	0.0061	0.0058	0.0026	0.06	1.34	0.03	0.01

Table A.1: The composition of the alloy used in the worked example.

The ‘normal’ parameter values for the diffusivity (D_{Eff}), the interface energy (γ), and the solubility product (K^{Eq}) are calculated at 850°C as implemented by Vonk [3], all the used parameter values are specified in Table 2.1. We use $D_{\text{Eff}} = 6.8 \cdot 10^{-16} \text{ m}^2/\text{s}$, $\gamma = 0.5012 \text{ J/m}^2$, and $K^{Eq} = 2.43 \cdot 10^{-4}$.

The parameter values are varied around the given values by multiplication with a factor of 0.9, 0.95, 1, 1.05, and 1.1. Here all other parameters are kept constant. The results for the average radius are given Figures A.1-A.3. For the solubility product the chemical energy is varied, as this is logarithmically dependent on the solubility product.

The effect of the diffusivity is, as described above, a mere shift in the time domain. The change in interface energy or chemical energy results in a much more significant change in the average precipitate radius. To further verify the effect of changes in interface and chemical energies the number density is included in Figures A.4 and A.5. The theoretically predicted effects from above, i.e., a higher interface energy slows down nucleation, and a larger (more negative) chemical energy increases the nucleation rate, can be observed.

REFERENCES

- [1] R. Kampmann and R. Wagner. Kinetics of precipitation in metastable binary alloys - Theory and application to Cu-1.9 at% Ti and Ni 14 at% Al. In P. Haasen, V. Gerold, R. Wagner, and M. F. Ashby, editors, *Decomposition of alloys: the early stages: proceedings of the 2nd Acta-Scripta Metallurgica conference*, number 2 in 2. Acta metallurgica, Pergamon press, 1984.

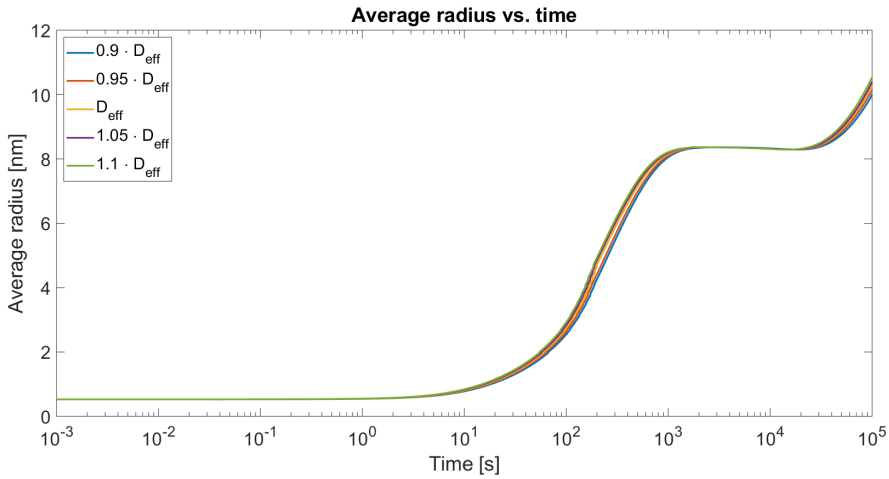


Figure A.1: Average precipitate radius vs. time with varied diffusivity.

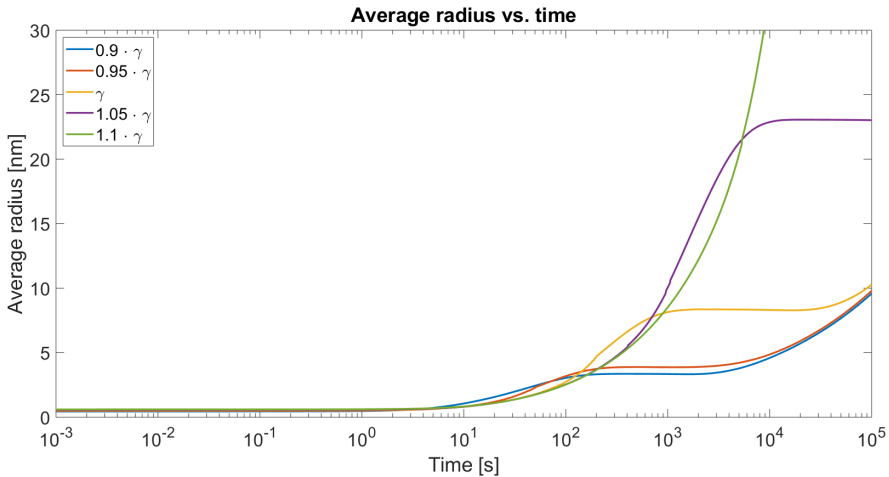


Figure A.2: Average precipitate radius vs. time with varied interface energy.

- [2] A. Deschamps and Y. Bréchet. Influence of predeformation and ageing of an Al-Zn-Mg alloy - II. modeling of precipitation kinetics and yield stress. *Acta materialia*, 47(1):293–305, 1999.
- [3] S. M. Vonk. Precipitates on dislocations: Mathematical modelling of nucleating and growing precipitates on dislocations. MSc. thesis, TU Delft, September 2016.

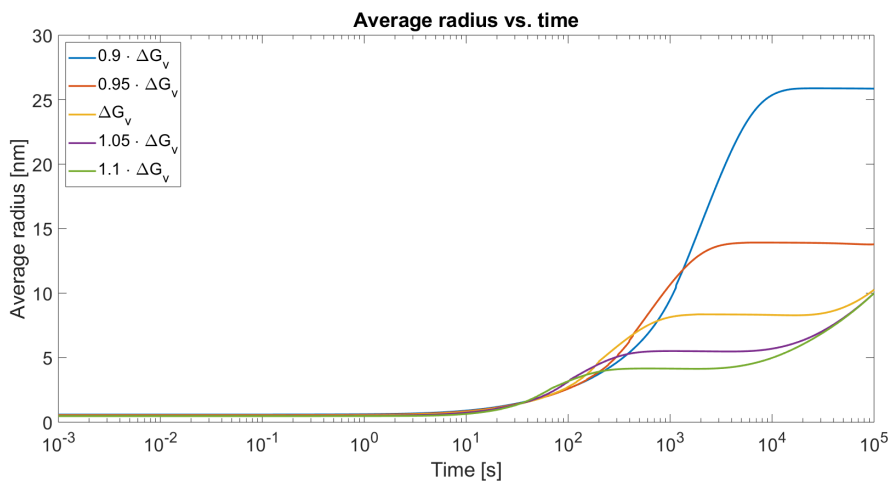


Figure A.3: Average precipitate radius vs. time with varied chemical energy.

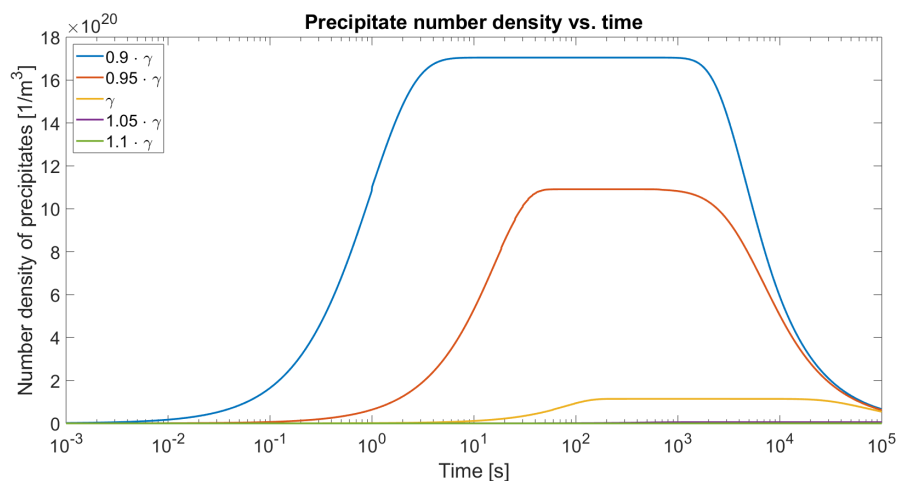


Figure A.4: Precipitate number density vs. time with varied interface energy.

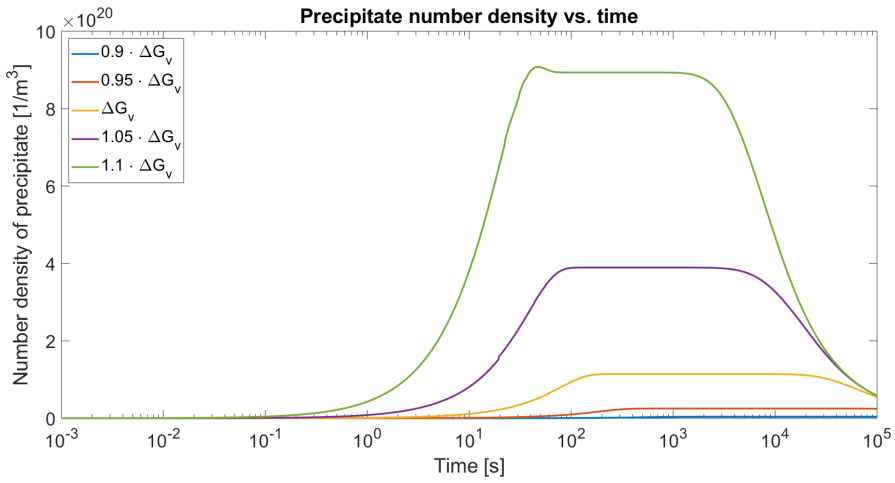


Figure A.5: Precipitate number density vs. time with varied chemical energy.

ACKNOWLEDGEMENTS

AT the end of a Ph.D. there comes a time to thank those who have contributed to the formation of this dissertation. In the most direct connection to this work I want to thank those who were involved with the content; Marcel for his insights and constant drive to deliver the best quality science, Kees for his enthusiasm and the organisation of the DENS project in the larger sense, and Winfried for his experience, literature knowledge, and perfectionism. Then there are the many people in and around the DENS project, in the Materials Science and Engineering department at TU Delft, at Tata Steel, and also in M2i.¹ With special thanks to Jan who has been a great office/room mate, and Peter who has been of great help with all things hpc and DelftBlue related.

Besides the professional help I also need to acknowledge the support given by my wife, and the motivation derived from my children. I want to apologise for the numerous evenings spent behind a screen or buried in books and articles. To my children, I hope that you will be able to appreciate this dissertation and the work your father did once you are able to read and understand the contents of this work. Then there is the added support from my family, my parents in particular for their support both during my study prior to working on the Ph.D., and during the work on the Ph.D. And the help provided with taking care of the children and in moving house, to be brief: in all the small and larger things that have helped me so much.

The greatest thanks are to God. As He provided the opportunity to pursue a Ph.D., and He has given me the strength and ability to keep going during the good and the bad times. All in the knowledge that He did not give up on me when I was impatient or did not want to follow the path He provided.

*Rutger Jarrick Slooter
Goudswaard, 2024*

¹The research in this dissertation was carried out under project number T17019m in the framework of the *Research Program of the Materials Innovation Institute (M2i)* supported by the Dutch government.

CURRICULUM VITÆ

Rutger Jarrick SLOOTER

14-03-1995 Born in Korendijk, Nederland.

EDUCATION

- 2006–2012 VWO-TTO
CSG Willem van Oranje, Oud-Beijerland
- 2012–2015 B.Sc. Applied Mathematics
Technische Universiteit Delft
- 2012–2015 B.Sc. Applied Physics
Technische Universiteit Delft
- 2015–2017 M.Sc. Applied Physics
Technische Universiteit Delft
Thesis: Quantum Optomechanics: Quadratic coupling and phonon counting
Supervisor: Prof. dr. Ya.M. Blanter
- 2015–2018 M.Sc. Applied Mathematics
Technische Universiteit Delft
Thesis: Automated analysis of microscopic images of cellular tissues
Supervisor: Dr. N.V. Budko
- 2018–2025 Ph.D. Material Science
Technische Universiteit Delft
Thesis: Precipitate development in steel
Promotor: Dr. ir. M.H.F. Sluiter
Copromotor: Dr. ir. C. Bos

EMPLOYMENT

- 2023– Adviseur, Sr. Medewerker Behandelen en Ontwikkeling
Octrooicentrum Nederland, Rijksdienst voor Ondernemend Nederland (RVO)

LIST OF PUBLICATIONS

PUBLICATIONS CONCERNING THIS DISSERTATION

2. **R.J. Slooter, M.H.F. Sluiter, W.G.T. Kranendonk, and C. Bos**, *Approximation and characteristic times in precipitation modelling*, *ISIJ international*, **Vol. 61, No. 5**, pp. 1698-1707, (2021).
3. **R.J. Slooter, M.H.F. Sluiter, W.G.T. Kranendonk, and C. Bos**, *A Reference-Free MEAM potential for α -Fe and γ -Fe*, *Journal of Physics: Condensed Matter*, **Vol. 34**, pp. 505901, (2022).
4. **R.J. Slooter, M.H.F. Sluiter, W.G.T. Kranendonk, and C. Bos**, *Atomistic simulation of carbide formation in ferrite*, *Computational Materials Science*, **Vol. 230**, pp. 112455, (2023).
5. **R.J. Slooter, M.H.F. Sluiter, W.G.T. Kranendonk, and C. Bos**, *Formation and growth of transition metal carbides in ferrite*, *Computational Materials Science*, **Vol. 242**, pp. 113097, (2024).

CONTRIBUTIONS TO CONFERENCES

6. **R.J. Slooter, M.H.F. Sluiter, W.G.T. Kranendonk, and C. Bos**, *Investigating of NbC proto-nuclei in steel*, *CALPHAD XLIX*, Stockholm, Sweden, (2022).
7. **R.J. Slooter, M.H.F. Sluiter, W.G.T. Kranendonk, and C. Bos**, *The precipitate interface*, *M2i conference*, April, (2022).

OTHER PUBLICATIONS REFERENCED TO THE AUTHOR

1. **J.D.P. Machado, R.J. Slooter and Ya.M. Blanter**, *Quantum signatures in quadratic optomechanics*, *Physical Review A*, **99**, 053801 (2019).